

INFORMATION TO USERS

This manuscript has been reproduced from the microfilm master. UMI films the text directly from the original or copy submitted. Thus, some thesis and dissertation copies are in typewriter face, while others may be from any type of computer printer.

The quality of this reproduction is dependent upon the quality of the copy submitted. Broken or indistinct print, colored or poor quality illustrations and photographs, print bleedthrough, substandard margins, and improper alignment can adversely affect reproduction.

In the unlikely event that the author did not send UMI a complete manuscript and there are missing pages, these will be noted. Also, if unauthorized copyright material had to be removed, a note will indicate the deletion.

Oversize materials (e.g., maps, drawings, charts) are reproduced by sectioning the original, beginning at the upper left-hand corner and continuing from left to right in equal sections with small overlaps. Each original is also photographed in one exposure and is included in reduced form at the back of the book.

Photographs included in the original manuscript have been reproduced xerographically in this copy. Higher quality 6" x 9" black and white photographic prints are available for any photographs or illustrations appearing in this copy for an additional charge. Contact UMI directly to order.

UMI

A Bell & Howell Information Company
300 North Zeeb Road, Ann Arbor MI 48106-1346 USA
313/761-4700 800/521-0600

Heat transport in the high-temperature superconductor Yttrium Barium Copper Oxide

Song Pu

Centre for the Physics of Materials
Department of Physics, McGill University
Montréal, Québec, Canada

A Thesis submitted to the
Faculty of Graduate Studies and Research
in partial fulfillment of the requirements for the degree of
Master of Science



National Library
of Canada

Acquisitions and
Bibliographic Services

395 Wellington Street
Ottawa ON K1A 0N4
Canada

Bibliothèque nationale
du Canada

Acquisitions et
services bibliographiques

395, rue Wellington
Ottawa ON K1A 0N4
Canada

Your file Votre référence

Our file Notre référence

The author has granted a non-exclusive licence allowing the National Library of Canada to reproduce, loan, distribute or sell copies of this thesis in microform, paper or electronic formats.

The author retains ownership of the copyright in this thesis. Neither the thesis nor substantial extracts from it may be printed or otherwise reproduced without the author's permission.

L'auteur a accordé une licence non exclusive permettant à la Bibliothèque nationale du Canada de reproduire, prêter, distribuer ou vendre des copies de cette thèse sous la forme de microfiche/film, de reproduction sur papier ou sur format électronique.

L'auteur conserve la propriété du droit d'auteur qui protège cette thèse. Ni la thèse ni des extraits substantiels de celle-ci ne doivent être imprimés ou autrement reproduits sans son autorisation.

0-612-29767-5

Canada

*To my lovely wife
and my parent*

CONTENTS

RÉSUMÉ	x
ABSTRACT	xi
ACKNOWLEDGMENTS	xii
1 OUTLINE AND MOTIVATION	1
2 THERMAL CONDUCTIVITY: A REVIEW	4
2.1 Thermal conductivity of solids	4
2.1.1 Scattering mechanisms	5
2.1.2 Mean free path and Mattiessen's rule	5
2.1.3 Electrons and the Wiedemann-Franz law	6
2.1.4 Phonons	9
2.1.5 Electrons and phonons: a comparison	10
2.2 Thermal conductivity of conventional superconductors	11
2.2.1 Electronic thermal conductivity	13
2.2.2 Lattice thermal conductivity	17
3 TRANSPORT PROPERTIES IN $\text{YBa}_2\text{Cu}_3\text{O}_{7-\delta}$: A BRIEF REVIEW	19
3.1 Crystal structure	19
3.2 Electrical resistivity	20
3.3 Heat conduction	20
3.4 Origin of the peak in $\kappa(T)$	23
3.4.1 Phonons	23
3.4.2 Electrons	28
4 EXPERIMENTAL ASPECTS	32
4.1 Sample preparation	32
4.1.1 Crystal growth	32
4.1.2 Oxygenation	34
4.1.3 Detwinning	34
4.1.4 Zn-doped crystals	34
4.2 Sample characterization	35
4.2.1 Polarized optical microscopy	35
4.2.2 Electrical resistivity	36
4.2.3 Scanning electron microscopy	37
4.2.4 Magnetic susceptibility	38
4.3 ^4He cryostat	38
4.4 Thermal conductivity set-up	41
4.5 Experimental procedure	45
4.6 Test on a gold sample	47

5	RESULTS AND DISCUSSION	51
5.1	Introduction	51
5.2	Peak in $\kappa(T)$: effect of Zn impurities	52
5.2.1	Results	52
5.2.2	Discussion	55
5.2.3	Summary	65
5.3	Anisotropy in $\kappa(T)$	68
5.3.1	Results	68
5.3.2	Discussion	71
5.3.3	Summary	77
	APPENDIX	79
A.1	Microwave conductivity	79
A.2	Thermal Hall effect	79
	REFERENCES	81

FIGURES AND TABLES

FIGURES

2.1 Schematic view of the relation between temperature gradient and the thermal current	6
2.2 Electrical conductivity σ and electronic thermal conductivity κ_e of a metal as a function of temperature.	8
2.3 The Lorenz ratio $\kappa_e/\sigma T$ for an ideally perfect metal and for specimens with imperfections	9
2.4 Thermal conductivity of a non-metallic crystal	10
2.5 Thermal conductivity of Pb-10% Bi alloy.	12
2.6 Ratio of superconducting to normal thermal conductivity for aluminum as a function of T/T_c	15
2.7 Comparison of theory and experiment for extremely pure metals.	16
3.1 Structure of YBCO crystal	20
3.2 Resistivity as a function of temperature, for a current along the a axis (ρ_a) and the b axis (ρ_b).	21
3.3 Temperature dependence of thermal conductivity by Yu <i>et al.</i>	22
3.4 Temperature dependence of the out-of-plane thermal conductivity κ_c single crystalline of YBCO	23
3.5 Low temperature thermal conductivity vs temperature for the untwinned YBCO crystal measured by Cohn	24
3.6 Thermal conductivity of sintered powder $\text{YBa}_2\text{Cu}_3\text{O}_{7-\delta}$ with different oxygen content.	25
3.7 Experimental data and theoretical curves by Peacor <i>et al.</i>	27
3.8 Quasiparticle scattering rate in $\text{YBa}_2\text{Cu}_3\text{O}_{7-\delta}$	28
3.9 Microwave conductivity of the detwinned crystal of $\text{YBa}_2\text{Cu}_3\text{O}_{7-\delta}$	29
3.10 Temperature dependence of the κ_e derived from $\kappa - \kappa_{ph}$ by Yu <i>et al.</i>	31
4.1 Schematic representation of a twinned crystal	35
4.2 Picture of a small area of a twinned sample	36
4.3 The transition temperature by resistivity and susceptibility.	37
4.4 The SEM image of one of our crystals	38
4.5 Susceptibility apparatus	39
4.6 Low-temperature portion of the cryostat	40
4.7 A drawing of the thermal conductivity apparatus	42
4.8 Resistivity vs temperature of three cernox thermometers.	43
4.9 The electrical circuit of the experiment	45
4.10 Demonstration of analysis performed in order to extract the thermal conductivity.	46
4.11 Thermal conductivity of Au sample at low temperature	48

4.12	κ vs temperature of a pure Au sample up to $T = 150$ K	49
5.1	$\kappa(T)/\kappa(180)$ vs T for $\text{YBa}_2(\text{Cu}_{1-x}\text{Zn}_x)_3\text{O}_{7-\delta}$ by Ting <i>et al.</i>	52
5.2	$\kappa(T)$ of $\text{YBa}_2(\text{Cu}_{1-x}\text{Zn}_x)_3\text{O}_{7-\delta}$ measured by Henning <i>et al.</i>	54
5.3	Electrical resistivity vs temperature for $\text{YBa}_2(\text{Cu}_{1-x}\text{Zn}_x)_3\text{O}_{7-\delta}$ (a-axis) crystals	55
5.4	Electrical resistivity vs temperature for YBCO crystals (twinned) of different Zn-content	56
5.5	T_c and ρ_0 as a function of Zn content	57
5.6	Thermal conductivity of twinned $\text{YBa}_2\text{Cu}_3\text{O}_{7-\delta}$ with Zn-impurities	58
5.7	Thermal conductivity vs T for detwinned $\text{YBa}_2\text{Cu}_3\text{O}_{7-\delta}$ crystals (a-axis) with different Zn content	59
5.8	Effect of Zn (upper) on microwave conductivity measured by Zhang	60
5.9	Comparison of $\kappa_{e,pl}$ measured by us with that from thermal Hall effect by Krishana.	61
5.10	Total thermal conductivity κ vs temperature for a pure crystal, experimental and fitted curve	62
5.11	κ vs $T(\text{K})$, with different Zn concentrations fitted by TW theory with different γ	63
5.12	κ vs $T(\text{K})$ with different Zn concentrations fitted by TW theory with different gap scaling ratio χ	64
5.13	Normalized electronic thermal conductivity $\kappa_{e,s}/\kappa_{e,n}$ calculated by Hirschfeld <i>et al.</i>	65
5.14	Demonstration of thermal conductivity consisting of phononic part and electronic part	66
5.15	Total thermal conductivity κ vs T fitted by using $\kappa_{e,s}$ calculated by Hirshfeld	67
5.16	The ratio of κ_{max} to κ_{norm} for twinned and detwinned Zn-doped YBCO crystals	68
5.17	The ratio of T_{max} to T_c as a function of Zn content	68
5.18	κ_{twin} (measured value) vs temperature, compared with κ_{ab} calculated using $\kappa_{ab} = \frac{1}{\frac{1}{2}(1/\kappa_a + 1/\kappa_b)}$	69
5.19	Resistivity of b-axis for pure and 0.6% Zn-doped crystals	69
5.20	The resistivity of a twinned crystals, comparison of measured and calculated using $\rho_{twin} = \frac{\rho_a + \rho_b}{2}$	70
5.21	Thermal conductivity of pure $\text{YBa}_2\text{Cu}_3\text{O}_{7-\delta}$ along two directions.	71
5.22	Thermal conductivity of detwinned crystals for Zn-doped sample	72
5.23	κ_{chain} for a pure $\text{YBa}_2\text{Cu}_3\text{O}_{7-\delta}$ crystal	73
5.24	Comparison of κ_{chain} and κ_{plane} vs reduced temperature (T/T_c).	74
5.25	The superfluid density when no coupling is available	75
5.26	New microwave data measured by Srikanth <i>et al.</i>	76
5.27	Penetration depth of YBCO measured by Zhang <i>et al.</i>	77
5.28	σ_1 vs temperature, along \vec{b} and \vec{a} axis, measured by Zhang <i>et al.</i>	78

5.1	The geometric factor, T_c and resistivity of our twinned Zn-doped crystal	53
5.2	The geometric factor, T_c and resistivity of our detwinned Zn-doped crystal	53

RÉSUMÉ

La conductivité thermique κ du supraconducteur à haute température $\text{YBa}_2\text{Cu}_3\text{O}_{7-\delta}$ (YBCO) a été l'objet de nombreuses recherches ces dernières années. Ces récentes études ont montré que κ :

- révèle un pic important dans l'état supraconducteur.
- est anisotrope dans le plan de base de la structure cristalline orthorhombique.

Les deux principaux thèmes de cette thèse sont: 1) l'origine du pic et 2) une étude détaillée de l'anisotropie.

Dans le but de faire la lumière sur la contribution relative des électrons et des phonons à la conduction de chaleur dans YBCO, nous avons mesuré les conductivités thermique et électrique de cristaux mâclés et démâclés de grande qualité, et ce pour différents niveaux de dopage par le Zn (0.0%, 0.6%, 1%, 2% et 3%). Nous avons trouvé que le pic est rapidement supprimé par les impuretés. Deux mécanismes possibles sont invoqués pour expliquer ces résultats, soient le scénario des phonons et le scénario des électrons.

En ce qui a trait à l'anisotropie entre l'axe- a et b des cristaux démâclés, seulement deux études précédentes se sont penchées sur le sujet. Nous avons obtenu quelques résultats frappants:

- un pic apparaît sur $\kappa_{chaînes} = \kappa_b - \kappa_a$, probablement parce que nos cristaux sont de meilleure qualité.
- ce pic est très similaire à celui de $\kappa_{plans} = \kappa_a$. Ceci est une évidence pour l'apparition de supraconductivité dans les chaînes en-dessous de 55 K.

Nous discuterons de ces comportements en relation avec le modèle de proximité (effect tunnel d'électrons entre les plans et les chaînes) qui, qualitativement, explique nos données de manière satisfaisante.

ABSTRACT

The thermal conductivity κ of the high-temperature superconductor $\text{YBa}_2\text{Cu}_3\text{O}_{7-\delta}$ has been the subject of numerous investigations in recent years. Previous measurements show that κ :

- exhibits a large peak in the superconducting state;
- is anisotropic in the basal plane of the orthorhombic crystal structure.

The main two subjects of this thesis are: 1) the origin of the peak and 2) a detailed investigation of the anisotropy.

In order to investigate the relative contribution of electrons and phonons to the heat conduction in YBCO, we have measured the thermal and electrical conductivities of high-quality twinned and detwinned crystals, with different levels of Zn-doping (from 0% to 3%). We found that the peak was rapidly suppressed by the impurities. Two scenarios are used to explain our results, attributing the effect to decrease in the carrier mean free path of either the electrons or the phonons.

As for the anisotropy between the a-axis and the b-axis, only two previous studies had previously been done. We find some new striking features:

- a peak appears in κ_{chain} below 50 K, revealed as a result of our using of higher purity samples.
- this peak is similar to that of κ_a below T_c (*i.e.* κ_{plane}), which we take as the evidence for the growth of superfluid density in the chains below 60 K.

We discuss these results in terms of a model of single-electron tunneling between chains and planes.

ACKNOWLEDGMENTS

To my wife Tao, for her love and support despite of the many lonely hours.

To my supervisor Professor Louis Taillefer, for his guidance and support throughout the course of my studies, as well as for his kindness, patience and understanding to both my study and life.

To Robert Gagnon, whom I have been worked with all the time in these 2 years, for his aid in every aspect of this work, from crystal growth to data analysis.

To Dr. Brett Ellman, Benoit Lussier, Christian Lupien, May Chiao and Stephane Legault, for their constant support in this project, their aid with the computer system and their help on my English, including correction of this thesis.

To Rut Besseling, for his collaboration in this project and for his friendship.

To D. Bonn for providing us with crystals for a comparative study.

To the technicians of the machine shop, Steve, John and Michel for their assistance in building up the cryostat.

To Cynthia, Paula, and Janice for many helps on my study.

Heat transport in the high-temperature
superconductor Yttrium Barium Copper Oxide

OUTLINE AND MOTIVATION

In this thesis, we present a study of the thermal conductivity κ of a high- T_c superconductor. The compound $\text{YBa}_2\text{Cu}_3\text{O}_{7-\delta}$ is chosen, because it is the best characterized and perhaps the most unconventional of the high- T_c superconductors. In particular, its electronic properties have received a great deal of experimental and theoretical attention in recent years.

Thermal conductivity has already been extensively studied in this kind of superconductors because of its ability to probe the electrons in both normal and superconducting states. It can provide invaluable information on the superconducting energy gap, the quasiparticle lifetime, the electron-phonon coupling, etc.

Two salient features of the thermal conductivity of $\text{YBa}_2\text{Cu}_3\text{O}_{7-\delta}$ have been reported:

- A sharp rise with decreasing temperature below T_c , giving rise to a peak in κ with a maximum at approximately $T_c/2$;
- An anisotropy in the basal plane transport throughout the the normal and superconducting states, with $\kappa_b > \kappa_a$.

The peak is due to the fact that for $T < T_c$, Cooper pairs form and the number of electrons available to scatter heat carriers falls rapidly, resulting in an increase in the mean free path of those carriers and an enhancement in $\kappa(T)$. For many years, the debate has been on the nature of these heat carriers: phonons or electrons?

Our approach to this controversial issue has been to investigate the effect of added impurities on the peak in $\kappa(T)$.

If the peak is caused by an increase in the quasiparticle lifetime $\tau(T)$ in clean crystals, as a result of the reduced electron-electron scattering, then the deliberate

addition of impurities should place a limit on this increase, resulting in a decrease in the amplitude of the peak in $\kappa(T)$ for doped samples.

Zn is expected to be an effective probe for this purpose. It substitutes preferentially for the Cu(2) atoms in the YBCO crystal structure, thereby specifically disturbing the CuO_2 planes which are the key element in the superconductivity. Existing microwave data show that the electronic mean free path is limited by impurity scattering from as little as 0.15% Zn, and the observed peak in the charge conduction $\sigma_1(T)$ almost disappears when the concentration of Zn reaches 0.3%, such low levels of Zn are not expected to affect phonons appreciably. Therefore, by measuring the thermal conductivity of Zn-doped samples, we hope to uncover the origin of the peak in κ (*i.e.* determine whether it is mainly electronic or mainly phononic).

The second issue is one on which there is much less information. We know that the CuO_2 planes are inter-spaced with Cu-O chains which lie along the b-axis of the orthorhombic crystal structure, parallel to the planes, therefore, the transport properties in the \vec{b} (chain + plane) direction can be different from that in the \vec{a} (plane) direction. Therefore, a study of the anisotropy of κ in the ab-plane of $\text{YBa}_2\text{Cu}_3\text{O}_{7-\delta}$ may prove very fruitful, as it will shed light on the role of CuO chains in the superconductivity of this compound.

Two groups have measured the ab-plane anisotropy of κ , but their results are in contradiction. Our detailed study resolves this contradiction and reveals new features not seen in those earlier studies, the significance of which will become clear later on.

This thesis is organized as follows:

We start off in chapter 2 by introducing some fundamental aspects of thermal conductivity in solids, the separate contribution of electrons and phonons are discussed. In the second section, heat transport in conventional superconductors is discussed along with the standard BRT theory, which gives a good description of κ in conventional superconductors.

Chapter 3 is devoted to the properties of YBCO: the structure is introduced first and then the transport properties are reviewed briefly, with an emphasis on heat conduction.

Chapter 4 covers the sample preparation and experimental setup, and some con-

siderations pertaining to the accuracy of our measurement of.

The results and discussions are presented in Chapter 5, which is divided into two sections:

- The first section deals with the origin of the peak in $\kappa(T)$, by studying the effect of Zn impurities. The related properties of microwave conductivity and thermal Hall effect are discussed. Two different scenarios are introduced to try to explain the data, namely, the phononic scenario (a theory by Tewordt and Wölkhausen), and the electronic scenario (a theory presented by Hirschfeld and Putikka). We conclude that the latter gives a better description of our data.
- The basal-plane anisotropy is discussed in the second section of this chapter. We present our data on κ_b and κ_a , which reveals a new feature on κ_{chain} (obtained by $\kappa_b - \kappa_a$), there exist a peak below 60 K. We believe that this is a evidence of the growth of superfluid density in chain electron, and then, we discuss a model of single-electron tunneling to explain our data qualitatively.

THERMAL CONDUCTIVITY: A REVIEW

2.1 Thermal conductivity of solids

There are several mechanisms by which heat can be transmitted through a solid and several processes which can limit the effectiveness of each mechanism [1]. In a non-magnetic insulator, heat is conducted by means of the thermal vibrations of the lattice. In good metals, the thermal conductivity is almost entirely due to the electrons. For some solids, such as alloys and superconductors, however, both transport mechanisms can make comparable contributions to the observed conductivity, and the relative proportions vary with temperature and composition. In particular, for superconductors, the proportions are different in the normal and superconducting states.

Let us discuss the definition of thermal conductivity κ first. For an isotropic solid, heat flow obeys the following simple relation [2]:

$$\vec{H} = -\kappa \vec{\nabla}T \quad (2.1)$$

where \vec{H} is a vector measuring the rate of flow of heat through a unit cross-section perpendicular to \vec{H} , $\vec{\nabla}T$ is the temperature gradient and κ the thermal conductivity. The negative sign indicates that heat flows down a temperature gradient from the hotter to the colder region.

In crystals without cubic symmetry, this should be modified to:

$$H_i = -\kappa_{ij} \frac{\Delta T}{\Delta x_j} \quad (2.2)$$

where the coefficients κ_{ij} form a second-rank tensor.

2.1.1 Scattering mechanisms

At temperature $T=0$, Bloch's theorem states that electrons in a perfect periodic potential, move forever without any degradation of their mean velocity in spite of the interaction with the fixed lattice of ions. [2] In real crystals, however, the heat carried by electrons would be limited by imperfections of the lattice (such as impurities, inhomogeneities and structural defects, etc.) which act as scattering centers to degrade the conduction of electrons. These scattering centers are called static impurities which in most cases conserve energy in the collision. Similarly, heat carried by phonons would also be limited by these imperfections, as well as by grain or sample boundaries. The anharmonic terms in the Hamiltonian would also eventually degrade the perfect conductivity of phonons. Finally, electrons and phonons scatter each other, and also themselves, these are inelastic processes. In general, this is very important in the intermediate temperature range.

2.1.2 Mean free path and Mattiessen's rule

On average, every particle (electron and phonon) travels a mean distance between collisions, called the mean free path l , and the time between collisions is called the relaxation time τ . In the general case, when there are more than one scattering mechanisms which are independent of the others, the total scattering rate, $1/\tau$, is the sum of the several scattering rates from different mechanisms:

$$\frac{1}{\tau} = \sum_i \frac{1}{\tau_i} \quad (2.3)$$

so that, for electrons:

$$\tau_{electron}^{-1} = \tau_{electron-imperfection}^{-1} + \tau_{electron-phonon}^{-1} + \tau_{electron-electron}^{-1} \quad (2.4)$$

Similarly, for phonons, we have:

$$\tau_{phonon}^{-1} = \tau_{phonon-imperfection}^{-1} + \tau_{phonon-electron}^{-1} + \tau_{phonon-phonon}^{-1} \quad (2.5)$$

This is called Mattiessen's Rule. Within the relaxation-time approximation, it is a valuable tool when we consider the thermal conductivity of solids.

2.1.3 Electrons and the Wiedemann-Franz law

For metals, κ can be obtained by a brief consideration of the situation of heat conduction in a gas of free electrons, derived by Drude [2]. It is assumed that free electrons are accelerated by the electric field over an average distance or mean free path l , before they lose the extra velocity acquired and resume their typical purely thermal motion. The electrical conductivity can then be expressed as:

$$\sigma = \frac{n_e e^2 \tau}{m_e} \quad (2.6)$$

where n_e is the number of free electrons per unit volume, e and m_e are their electric charge and effective mass and τ is the relaxation time of electrons, related to mean free path via $l = v_F \tau$, where v_F is the fermi velocity. Then the heat conductivity can be derived as follows.

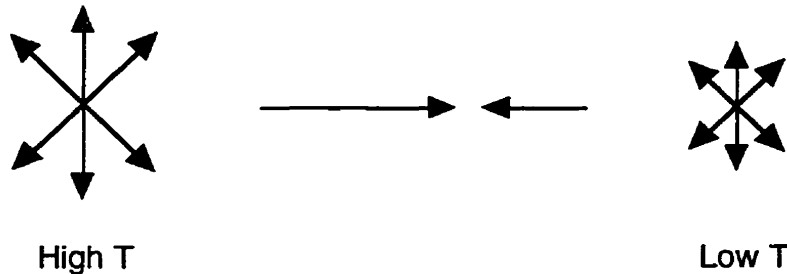


Figure 2.1: Schematic view of the relation between temperature gradient and the thermal current. after [2]. Electrons arriving at the center x from the left had their last collision in the high temperature region. Those arriving at the center from the right had their last collision in the low temperature region.

The thermal current in a metal is carried by the conduction electrons, we have:

$$j_q = -\kappa_e \frac{dT}{dx} \quad (2.7)$$

where j_q is the thermal current density, defined to be a vector parallel to the direction of the heat flow. To extract a quantitative estimate of κ , consider first a 1-dimensional model, in which the electrons can only move along the x -axis, so that at a point x , half the electrons come from a high temperature region and half from the low temperature region, as shown in figure 2.1. If $\epsilon(T)$ is the thermal energy per electron in the metal in equilibrium at temperature T , and v the velocity of the electron, then the electrons arriving at x from the high temperature side will, on average, have

$\epsilon(T[x - v\tau])$ (because their last collision happened at $x - v\tau$). Their contribution to thermal current density will be:

$$\frac{n}{2}v\epsilon(T([x - v\tau])),$$

with n the number of electrons per unit volume and v their velocity. Similarly, the electrons arriving at x from the low temperature side will contribute

$$\frac{n}{2}v\epsilon(T([x + v\tau])).$$

Adding these together gives:

$$j_q = \frac{1}{2}nv[\epsilon(T([x - v\tau]) - \epsilon(T([x + v\tau]))]$$

Provided that the variation in temperature over the mean free path ($l = v\tau$) is very small, we expand this as

$$j_q = nv^2\tau \frac{d\epsilon}{dT} \left(-\frac{dT}{dx}\right) \quad (2.8)$$

To go from this to the 3-dimensional case, we need only replace v by the x-component v_x of the electronic velocity \vec{v} , and average over all directions. Since $\langle v_x^2 \rangle = \langle v_y^2 \rangle = \langle v_z^2 \rangle = \frac{1}{3}v^2$ and since $n \frac{d\epsilon}{dT} = \left(\frac{N}{V} \frac{d\epsilon}{dT}\right) = \frac{(dE/dT)}{V} = c_v$, the electronic specific heat, we have:

$$\vec{j}_q = \frac{1}{3}v^2\tau c_v \frac{(-\partial T)}{\partial x} \quad (2.9)$$

or

$$\kappa_e = \frac{1}{3}v^2\tau c_v = \frac{1}{3}lv c_v \quad (2.10)$$

Since the relaxation time is a difficult quantity to compute and to measure, we assume the same scattering rate for both thermal and electrical processes, then, dividing κ_e by σ , we got:

$$\frac{\kappa_e}{\sigma} = \frac{2m_e v^2 c_e}{3e^2} \quad (2.11)$$

According to Sommerfeld theory of conduction in metals, the specific heat $c_v = \frac{\pi^2}{2} \left(\frac{k_B T}{\epsilon_F}\right) n k_B$ and $v^2 = v_F^2 = 2\epsilon_F/m$. Inserting these values in eqn. 2.11, we find,

$$L_0 = \kappa_e/\sigma T = \frac{\pi^2}{3} (k_B/e)^2 = 2.44 \times 10^{-8} W\Omega/K^2 \quad (2.12)$$

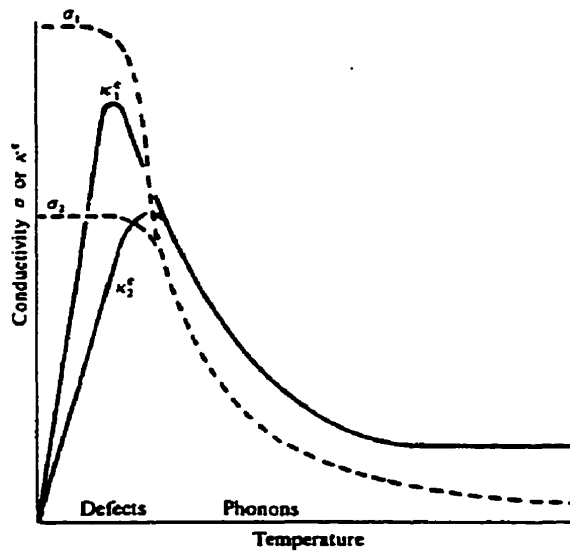


Figure 2.2: Electrical conductivity σ and electronic thermal conductivity κ^e of a metal as function of temperature. the upper curves in each case are for more perfect specimens than the lower curves. after [1]

This is called the Wiedemann-Franz Law (WFL) and L_0 is known as the Sommerfeld value. Figure 2.2 shows the electrical conductivity σ and electronic thermal conductivity κ_e of a typical metal over a wide temperature range.

In general, at high temperatures, the electronic thermal conductivity is constant and at low temperatures it is proportional to the temperature, as would be deduced by using WFL and the temperature dependence of the electrical conductivity. At intermediate temperatures, however, the thermal conductivity varies less rapidly with temperature than would be expected from WFL. This can be explained by the fact that charge transport can only be affected by the carrier's momentum, so, the only way to degrade electrical current is by changing the electron velocity. Heat transport, on the other hand, relies on both energy and momentum of the carrier, that is, there exist an extra possibility for degrading this kind of current, for example, in inelastic collision, the consuming of the energy $((\epsilon - \mu)/T$ in this case), would further degrade the thermal current. This causes Lorenz number ($L = \kappa_e/\sigma T$) to be smaller than the Sommerfeld value (L_0) in certain temperature range, as shown in figure 2.3

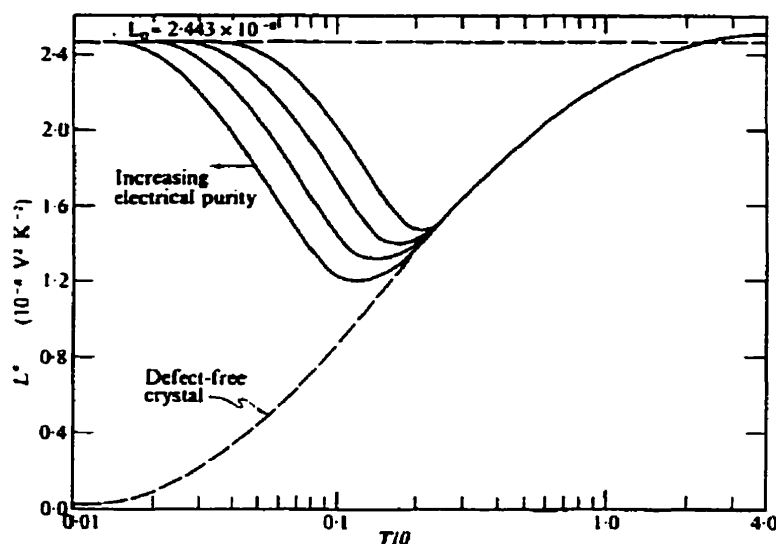


Figure 2.3: The Lorenz ratio $\kappa_e/\sigma T$ for an ideally perfect metal and for specimens with imperfections plotted as a function of the ratio of temperature to the Debye characteristic temperature. In the perfect metal, inelastic scattering dominates at low temperatures, causing a large suppression of the Lorenz ratio.

2.1.4 Phonons

In an insulator, heat is carried by lattice vibrations, with the appropriate mean free path l_{ph} defined as the distance such a mode travels before its intensity is attenuated by scattering to $\frac{1}{2}$ of its initial value. In quantum theory [1], this is considered as heat being transmitted by phonons, which are the quanta of energy in each mode of vibration, and the mean free path l_{ph} is a measure of the rate at which energy is exchanged between different phonon modes. We can again use the expression $\kappa_{ph} = \frac{1}{3}c_v v l_{ph}$ to represent the heat conductivity by phonons, where v is now the mean phonon velocity (equal to a suitable average velocity of sound in the crystal) and c_v is the heat capacity contributed by the lattice.

Figure 2.4 shows a typical phononic thermal conductivity as a function of temperature. At high temperatures, l_{ph} is limited by direct interactions between the phonons themselves, and is inversely proportional to T , as is κ_{ph} . As the temperature decreases, interactions among the phonons become rapidly less effective in restricting l_{ph} , thus increases more rapidly than $1/T$. For sufficiently perfect crystals, this increase could be best represented by an exponential form $l_{ph} \propto \exp \frac{T^*}{T}$, where T^* is a characteristic temperature for a particular crystal. At low temperatures (~ 1

K), l_{ph} may reach several millimeters and thus becomes comparable with the smallest dimensions of a typical specimen, it then tends to a constant value. Because the mean velocity v is essentially independent of temperature, consequently, κ is proportional to T^3 at low temperature (when $c_v \sim T^3$).

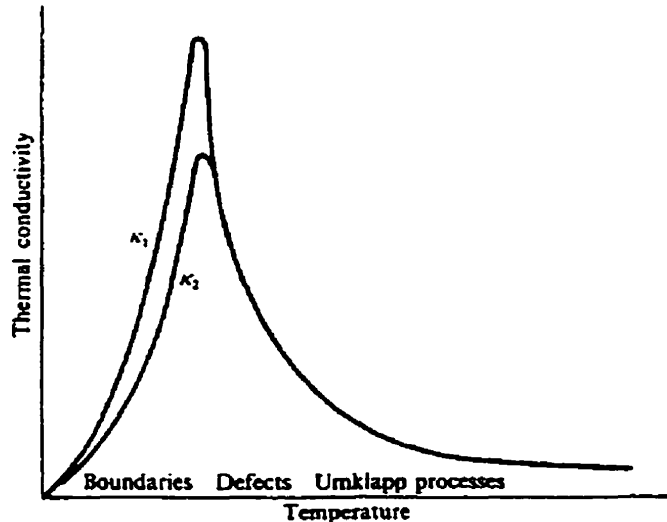


Figure 2.4: Thermal conductivity of a non-metallic crystal. The upper curve is for a crystal of larger diameter than the lower curve. The dominant phonon-scattering mechanism are indicated along the abscissa. after [1]

2.1.5 Electrons and phonons: a comparison

To conclude this sector, we compare the different behavior of electrons and phonons here.

- For electrons and phonons at high temperature, the mean free paths are both proportional to $1/T$, but the electronic heat capacity is proportional to temperature while for the phonons, it is constant. Thus the temperature dependences of the two thermal conductivities differ by one power of T , specifically, $\kappa_e \sim \text{constant}$, while $\kappa_{ph} \sim \frac{1}{T}$.
- As we approach the peak, the mean free path increases much more rapidly than $1/T$ in both cases, this rapid change more than makes up for the decreasing heat capacity. As results, for metals, the constant thermal conductivity changes to $1/T^2$, while for phonons the $1/T$ variation changes to an exponential increase.

- At the lowest temperature, both mean free paths reach constant values and thermal conductivity is proportional to the heat capacity contributed by the appropriate heat carriers (T for electron, T^3 for phonon). Hence, κ_e is proportional to T , while κ_{ph} proportional to T^3 . It should be emphasized, however, that for electrons, the mean free path is determined by the imperfections present, while for phonons, it is determined by the external boundaries of the crystal (or the grain boundaries in a polycrystal).

There are other possibilities of heat carriers, for example, photons or magnons. However, heat conduction by lattice vibrations and by electrons constitute the most important mechanisms in nearly all substances at nearly all temperatures. Therefore, we only consider these two contributions in this thesis.

2.2 Thermal conductivity of conventional superconductors

Let us talk about the thermal conductivity of traditional superconductors. There are two fundamental aspects of the superconducting condensate which have effects on the thermal conductivity of the superconductor:

- Cooper pairs carry no entropy.¹
- Cooper pairs do not scatter phonons.

The first condition means that the electronic thermal conductivity decreases with decreasing temperature more rapidly in the superconducting state than in the normal state. Since $\kappa_e \propto nvl_e$, the number of quasiparticles decrease with temperature and goes to zero at $T = 0$, this causes $\kappa_e \sim \exp(-\Delta/kT)$ at low temperature. The second condition has a more subtle effect: provided that the mean-free path of phonons l_{ph} at $T > T_c$ is limited by electron scattering, the phonon thermal conductivity will rise on passing into the superconducting state, because the number of quasi-particle excitations rapidly decreases—leading to an enhancement in the mean-free-path of phonons l_{ph} . A competition between the rapidly diminishing κ_e on the one hand and the increasing κ_{ph} on the other hand will determine the overall dependence of

¹For example, experiments by Daunt and Mendelssohn [3] showed that the specific heat of the superconducting electrons is zero.

the total thermal conductivity of a given superconductor. In the vast majority of cases κ falls rapidly as the material goes superconducting. However, in some alloys, sufficiently disordered so that κ_e is small and κ_{ph} accounts for a large fraction of the normal-state thermal conductivity, one may observe a rise in the total conductivity as the sample enters into its superconducting domain. A classic example of this is lead-10% bismuth alloy [4] (shown in figure 2.5). A peak below T_c is obvious, which is qualitatively similar to the behavior observed in high- T_c superconductors, to be discussed later. Eventually, of course, the thermal conductivity must turn over and start decreasing with temperature. This follows because the phonon population decreases, and phonon-defects and phonon-boundary scattering start to dominate the transport at low temperature.

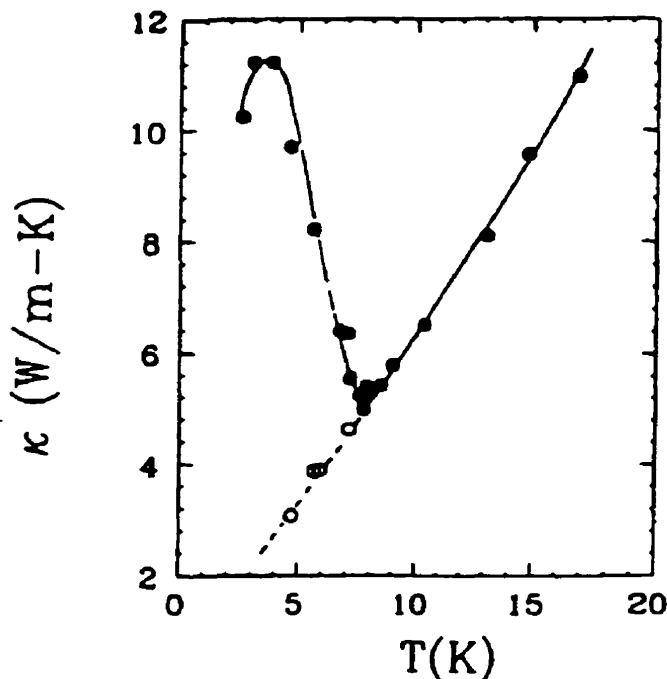


Figure 2.5: Thermal conductivity of Pb-10% Bi alloy, where a peak below T_c is obvious. Open symbols indicate normal-state data below the transition temperature, after Mendelssohn [4].

In the following, I will introduce the theory of Bardeen, Rickayzen and Tewordt (BRT) [5] which accounts well for the behavior of κ in conventional superconductors. This is based on the famous theory of Bardeen, Cooper and Schriffer (BCS) [6], which we will not review here. Let us only say that in the presence of an attractive potential

between electrons, BCS showed that a state with energy lower than that of the normal state can be formed by taking a linear combination of normal-state configurations in which pair states of electrons of equal but opposite momentum and spin ($k\uparrow, -k\downarrow$) are both either occupied or unoccupied. These pairs are known as Cooper pairs, identified with the superconducting ground state. In conventional superconductors, the attractive pairing interaction is mediated by the lattice. Excited states are formed when only one state of a pair is occupied in all configurations or when pair excitations are formed so as to be orthogonal to the ground state.

The important concept is that there exists an energy gap Δ of order $k_B T_c$ in the quasi-particle excitation spectrum of the system, $E(\vec{k}) = [\epsilon(\vec{k})^2 + \Delta(\vec{k})^2]^{\frac{1}{2}}$, which plays the role of a minimum excitation energy (where $\epsilon(\vec{k})$ is the energy of the electron with wave-vector \vec{k} in the normal metal).

Now let us derive the heat transport equation of a superconductor. At low temperature, at which the phenomenon of superconductivity is found, the system is not highly excited so the excitations can be treated as independent. Then one can set up a Boltzmann equation for the transport problem, which has the physical meaning that the driving force is equal to the dissipative effects of collisions:

$$\frac{\partial f}{\partial t} - \frac{e\vec{E}}{\hbar} \nabla_{\vec{k}} f + \vec{v} \nabla_{\vec{r}} f = \left(\frac{\partial f}{\partial t} \right)_{coll} \quad (2.13)$$

where \vec{v} is the velocity and \vec{E} the electrical field. f is the non-equilibrium distribution function.

2.2.1 Electronic thermal conductivity

First, we consider that electrons are scattered elastically only by impurities. we will only quote the basic results of this theory in here: applying the Boltzmann equation above to the heat transport (eqn. 2.8), we can get the heat current due to electrons to be

$$j_q = -\frac{2}{T} \sum \mu_i^2 E_k^2 \frac{\partial f_0}{\partial E_k} v_k^2 \tau_k \quad (2.14)$$

where E_k the quasiparticle energy, v_k the group velocity of the quasiparticles in the superconducting state, and τ_k the relaxation time.

The quasiparticle velocity is found to be

$$v_k = \left| \frac{\epsilon_k}{E_k} \right| v_F = \frac{N(0)}{N_s(E)} v_F \quad (2.15)$$

with $N(0)$ the density of states in the normal state and $N_s(E)$ the quasiparticle density of states.

Then, Bardeen *et al.* proceeded to compute the scattering time τ_s in the superconducting state by solving the Boltzmann equation. Assuming an isotropic gap, and applying the relaxation-time approximation, they get

$$\tau_s = \left| \frac{E}{\epsilon} \right| \tau_N \quad (2.16)$$

where τ_N is the relaxation time in normal state.

Combining this with eqn. 2.15 they get an important result for the mean free path:

$$l_s = l_N \quad (2.17)$$

that is, this kind of scattering (impurity) is best described by a relatively constant mean free path. Putting everything into eqn. 2.14 and changing the sum into an integral, they obtain:

$$\kappa_{e,s} = \frac{2}{T} v_F^2 \tau_N N(0) \int_{\Delta T}^{+\infty} dE E^2 \left(-\frac{\partial f}{\partial E} \right) \int \frac{d\Omega}{4\pi} \cos^2 \theta \quad (2.18)$$

By letting $\Delta \rightarrow 0$, we can find a similar expression for the normal state thermal conductivity $\kappa_{e,n}$. Dividing $\kappa_{e,s}$ by $\kappa_{e,n}$ we get

$$\kappa_{e,s}(T) / \kappa_{e,n} = \int_{\Delta(T)}^{+\infty} dE E^2 \frac{\partial f}{\partial E} / \int_0^{+\infty} d\epsilon \epsilon^2 \frac{\partial f}{\partial \epsilon} \quad (2.19)$$

A plot of the theoretical ($\kappa_{e,s}/\kappa_{e,n}$) versus (T/T_c), together with a plot of experimental data of aluminum, for three samples of varying impurity concentration, is provided in figure 2.6. As one can see, there is excellent agreement between this theory and experiment.

For completeness, let us consider the other case, the interaction between electrons and phonons, part of which has already been used in forming the superconducting ground state [8, 9]. In this case, the scattering is inelastic, and condition of eqn. 2.16 is no longer satisfied, making things a little bit complicated. Still, we can obtain a

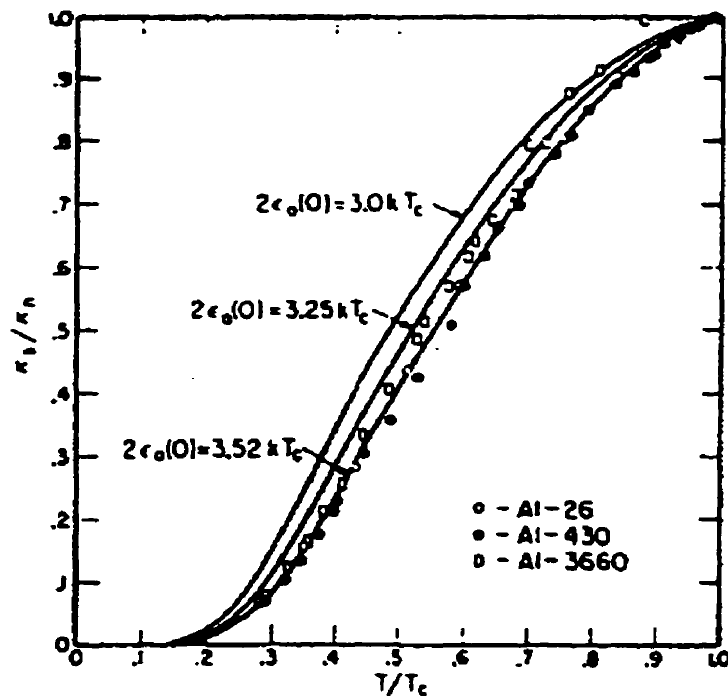


Figure 2.6: Ratio of superconducting to normal thermal conductivity for aluminum as a function of T/T_c (after Satterthwaite [7]). The solid lines represent the BRT calculation in the presence of impurity scattering for three values of the gap parameter, namely $2\Delta(0) = 3.00, 3.25,$ and 3.52 times $k_B T_c$.

Boltzmann equation in the usual way, by equating the total rate of change of the distribution function to zero. Then we can employ the variational principle, whose physical content may be expressed by saying that matter arranges itself so that the rate of entropy generation is a minimum, as pointed by Ziman [10]. In this manner, Bardeen *et al.* obtained a lower bound to $\kappa_{e,s}$, which indicated a value smaller than -0.5 for $d(\frac{\kappa_{e,s}}{\kappa_{e,n}})/d(\frac{T}{T_c})$, shown in figure 2.7 (cross).

This is in disagreement with the experimental data for the purest specimens of tin, lead and mercury. The experimentally determined $\kappa_{e,s}/\kappa_{e,n}$ drops very sharply as temperature is lowered below T_c , where $d(\frac{\kappa_{e,s}}{\kappa_{e,n}})/d(\frac{T}{T_c}) = 5$.

In a later work, Kadanoff and Martin [11], by using time-dependent correlation functions, calculated thermal conductivity of the superconductor. They yielded results in good agreement with observed thermal conductivity. They set up a model which treats the lifetime of single-particle excitations due to lattice interactions as constant. The difference between their theory and that of BRT is that they assume

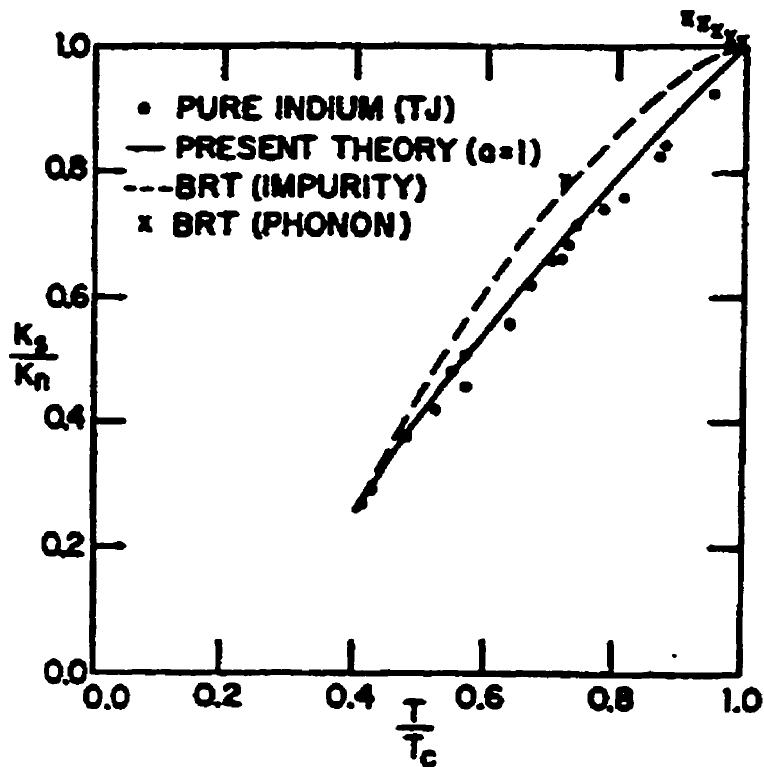


Figure 2.7: Comparison of theory presented by Kadanoff *et al.* along with data for extremely pure metals, where inelastic scattering of electrons is dominant. The data for very pure tin (circles) agrees very well with the theory; the BRT result in this case is also included (crosses)

that the collision time is not strongly altered by the occurrence of the gap, that is, the mean free time, instead of the mean free path, is relatively independent of the excitation.

Then, their object is to determine thermal conductivities from width of excitation (which is the inverse quasiparticle lifetime). They first set up a heat-current correlation function and then solve it by introducing the Green's function, when the conductivity is limited by phonon scattering, they get

$$\kappa_e = \frac{\pi^2}{3} \frac{n}{m} k_B^2 T [\Gamma + v_F/l]^{-1} \quad (2.20)$$

There exist two contributions to the thermal resistance: 1) Γ , which results from phonon absorption and emission and is proportional to T^3 , and 2) v_F/l , which results from impurity scattering and is independent of T , this contribute additively to the thermal resistance.

In this model, The interaction between electron and phonon was included by in-

serting a parameter Γ into the single-particle correlation function. If these correlation functions were expressed as functions of space and time and substituted into the current correlation function, their essential effect would be to reduce that correlation function by the factor $\exp(-\Gamma|t-t'|)$. This modification agrees with the expectation that phonon emission and absorption is normally described by a relatively constant life time. The ratio of the electronic thermal conductivities in the superconducting and normal states, when the conductivity is limited by phonon scattering, can be calculated as:

$$\kappa_{e,s}/\kappa_{e,n} = \frac{3}{2\pi^2} \int_0^\infty d\epsilon \epsilon^2 \sec^2 \frac{1}{2} [\epsilon^2 + (\beta\Delta)^2]^{\frac{1}{2}} \quad (2.21)$$

Figure 2.7 shows the comparison of this theory with experimental data, together with BRT's result, and indicates that the above theory could give a better description than BRT theory in this case.

2.2.2 Lattice thermal conductivity

In BRT theory, for the sake of simplicity, the authors only considered κ_{ph} limited by electron scattering. Then the thermal current density is

$$W_{ph} = \sum_q \hbar q_z v_0^2 \delta N_q \quad (2.22)$$

where N_q is the number of phonons with wave vector q and v_0 is the velocity of sound in a metal.

To calculate the thermal conductivity, we proceed by setting up a Boltzmann equation and reducing it to:

$$v_0 \frac{q_s}{q} \frac{\partial N_q}{\partial T} \frac{\partial T}{\partial Z} = \left(\frac{\partial N_q}{\partial t} \right)_{coll} \quad (2.23)$$

Following the procedure for normal metals, they get a solution of this equation. The thermal conductivity is then derived as:

$$\kappa_{gs} = D \left(\frac{T}{\Theta} \right)^2 \int_0^\infty \frac{u^3 du}{(e^u - 1)(1 - e^{-u})g(u)} \quad (2.24)$$

where D is a constant independent of temperature and u the reduced energy $\hbar v/k_B T$, where:

$$g(u) = \frac{1 - e^{-u}}{u} \int dE \left| \frac{EE'}{\epsilon\epsilon'} \right| \left(1 - \frac{\epsilon_0^2}{EE'} \right) f(E) f(-E') \quad (2.25)$$

the energies are measured in units of $k_B T$ and the physical meaning of $g(u)$ is the ratio of relaxation time of electrons in normal state $\tau_{e,n}$ to that of quasiparticles in superconducting state $\tau_{e,s}$, therefore, it goes to 1 above T_c . In the superconducting state, it gives us the information about: 1) the number of electrons that scatter phonons, which decrease as temperature goes down. 2) the scattering matrix element including the coherence factor.

However, it is not easy to obtain thermal conductivity data which can be unequivocally interpreted as lattice conductivity limited only by electron scattering. At lower temperatures, where the electronic contribution is negligible, it appears that the lattice waves are scattered mainly by the boundaries of the crystals. At higher temperatures where the lattice waves are scattered mainly by the electrons, the main contribution to the thermal conductivity comes from electrons.

This can be shown, however, qualitatively in figure 2.5, in which a peak appears as the temperature drops below T_c indicating that the phonon contribution is large. A similar peak also appears below T_c in YBCO, which is the major concern of this thesis. To explain that peak, we will revisit the above theory again through theory of Tewordt and Wölkhausen in section 3.4.1.

TRANSPORT PROPERTIES IN $\text{YBa}_2\text{Cu}_3\text{O}_{7-\delta}$: A BRIEF REVIEW

3.1 *Crystal structure*

The high- T_c compound $\text{YBa}_2\text{Cu}_3\text{O}_{7-\delta}$ (also labeled YBCO or 1-2-3) was discovered in 1987, and has been intensely studied ever since. Although it does not have the highest T_c (93 K), high sample quality can be achieved relatively easily, which enables us to make good single crystals with narrow superconducting transitions.

As with other high- T_c cuprates, $\text{YBa}_2\text{Cu}_3\text{O}_{7-\delta}$ is also based on CuO_2 planes in the a-b plane of a tetragonal structure. At high temperature, the tetragonal YBCO has six oxygen atoms. After annealing, an additional O is introduced in the chains along the b-axis, between two Cu atoms, which results in a transition to an orthorhombic structure. The length of the b-axis is larger than the a-axis by 2 ~ 3%. Figure 3.1 shows the structure of YBCO in the 2 phases. As a result, the introduced oxygen atoms in the chain site are relatively easily removed from (or added in), and the physical properties of a $\text{YBa}_2\text{Cu}_3\text{O}_{7-\delta}$ crystal can be strongly affected by the oxygen content δ . For example, it undergoes a transition from superconductor to insulator with decreasing oxygen content from $\delta = 0.0$ to $\delta = 1.0$ [12]. In this thesis, all crystals investigated here, $\delta = 0.1$ and the structure is therefore made of the CuO_2 planes and CuO chains along b-axis.

Because atomic substitution is an important approach, which will be used by us to obtain an insight into the transport properties of YBCO, we want also to mention the following: Neutron diffraction and Moss-Bauer spectroscopy have shown that different metal ions prefer different Cu site, for example, Au, Fe and Al occupy selectively the Cu(1) (chain) sites while Zn and Ni ions occupy only the Cu(2) (plane) site. This gives us some clues on choosing the doping ions.

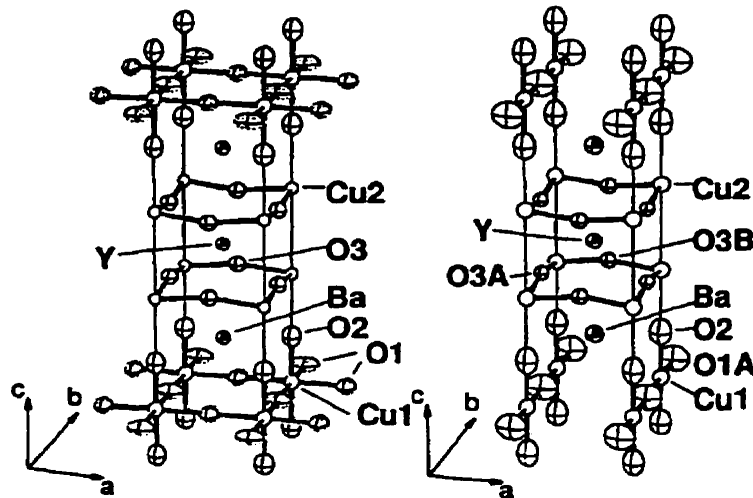


Figure 3.1: Structure of YBCO. It undergoes a transition from tetragonal to orthorhombic at 530 K. Comparison of the tetragonal (left) and orthorhombic (right) are shown above. The c axis is vertical and the a axis horizontal.

3.2 Electrical resistivity

From early on, a linear temperature dependence of the electrical resistivity in the normal state has been observed, which is now considered as a key characteristic property of the planes. Later on, R. Gagnon *et al.* [13] showed that the electrical conduction in the Cu-O chains is quite different to that of the CuO_2 planes: the chain resistivity, defined as $\rho_{chain} = \rho_b - \rho_a$, extrapolates to a high residual value at low temperatures and obeys a rough T^2 dependence up to room temperature. Figure 3.2 shows the electrical resistivity of a pure detwinned YBCO sample measured by us. Note that the chains conduct just as well as the planes above T_c .

3.3 Heat conduction

The thermal conductivity of $\text{YBa}_2\text{Cu}_3\text{O}_{7-\delta}$ as measured by Yu *et al.* [14], is shown in figure 3.3. The following features are observed:

1. The overall thermal conductivity is of order 10 W/mK in the normal state. We can estimate the maximum electronic conductivity using WFL: $\kappa_e \leq L_0 T / \rho \approx 3.0 \text{ W/mK}$. Therefore, one can conclude that phonons carry at least 70% of the heat.

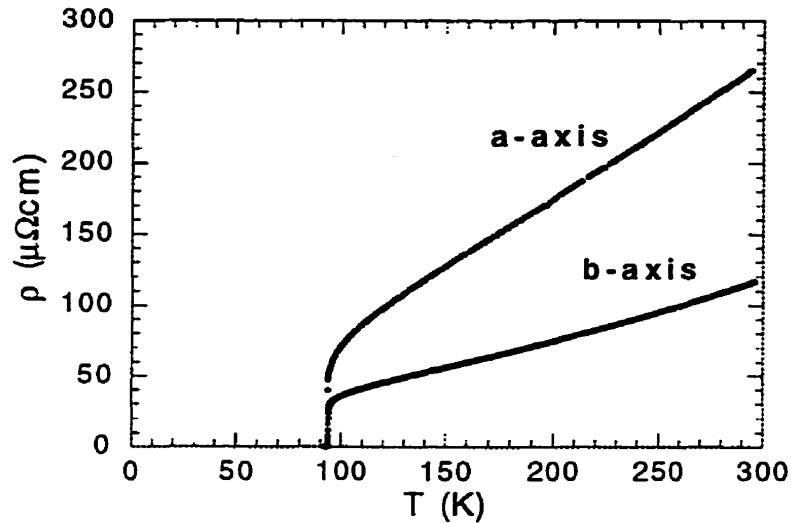


Figure 3.2: Resistivity as a function of temperature, for a current along the a axis (ρ_a) and the b axis (ρ_b).

2. A sudden rise and pronounced maximum of κ is observed below T_c . The thermal conductivity increases by a factor of 2 from T_c to the peak position at about 40 K. The origin of this peak is one of the main concerns of this thesis.
3. Just below T_c , we note that the thermal conductivity rises fairly abruptly. However, the rise is not as sharp as predicted by certain theories [17].
4. The results in figure 3.3 are measured in the ab-plane. The across-the-plane conductivity, κ_c , was measured by Hagen *et al.* [15] and is shown in figure 3.4. We note a distinctly different behavior from what is observed for heat flow along the planes. The overall thermal conductivity is some 4-5 times smaller than that in the plane, increasing slowly with decreasing temperature, with a broad peak in the range of 50-80 K beyond which it falls to zero. There is no hint of any anomalous behavior at the transition temperature T_c .
5. The ab-plane results of figure 3.3 are obtained from detwinned specimens of YBCO. The thermal conductivity is different along the two directions, \vec{a} and \vec{b} , with $\kappa_b > \kappa_a$. The additional conduction along \vec{b} is attributed (at least in part) to chain electrons. We note that the difference between κ_b and κ_a is not far beyond the experimental uncertainty on the absolute value of κ ($\pm 15\%$). In this respect, we point out that Cohn *et al.* [16] obtained similar results for

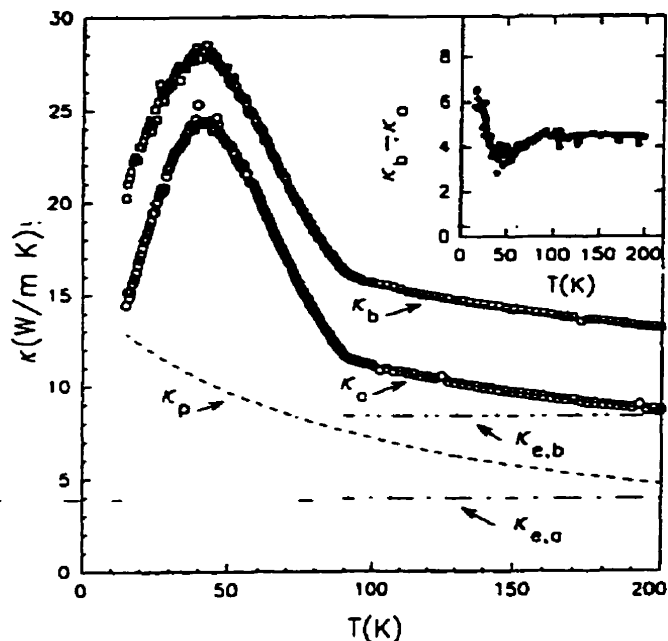


Figure 3.3: Temperature dependence of thermal conductivity in the a(o) and b(\square) direction. dashed line, the derived phonon thermal conductivity κ_p ; Dot-dashed line and dot-dot-dashed line, the derived electronic thermal conductivity. Inset: $\kappa_b - \kappa_a$ vs T. after [14]

κ_b and κ_a , but with different absolute values (see figure 3.5) such that $\kappa_a > \kappa_b$. One of the main aims of our work was to have a closer look at this anisotropy.

6. As mentioned earlier, oxygen is the crucial parameter determining whether a $\text{YBa}_2\text{Cu}_3\text{O}_{7-\delta}$ compound behaves as a superconductor or as an insulator. This greatly influences the thermal transport properties. Zavaritskii *et al.* [18] studied κ of YBCO as a function of oxygen deficiency δ by successively annealing their sintered powder samples in vacuum or in an oxygen atmosphere. They found as the oxygen concentration is reduced from $\delta = 0$ to $\delta = 0.3$, the maximum in the thermal conductivity shifts to lower temperatures and the magnitude of the thermal conductivity decreases. Further vacuum annealing to $\delta > 0.5$ results in non-superconducting material with still lower thermal conductivity (see figure 3.6). Z. Gold [19] measured a deoxygenated single crystal ($\delta = 0.7$) and got a nearly temperature independent κ , with a value around $6.35 \text{ Wm}^{-1}\text{K}^{-1}$ in the range $40 \text{ K} \sim 140 \text{ K}$, this is believed entirely due to phonons.

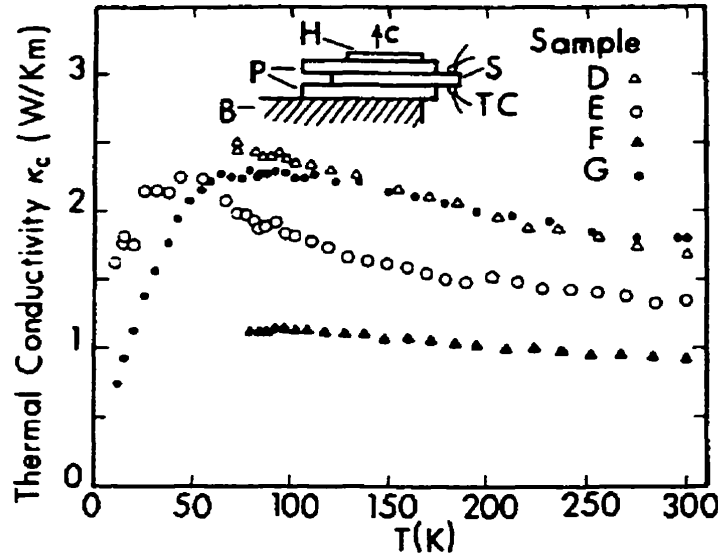


Figure 3.4: Temperature dependence of the out-of-plane thermal conductivity κ_c single crystalline $\text{YBa}_2\text{Cu}_3\text{O}_{7-\delta}$ with $T_c \approx 90$ K. No obvious anomaly is shown near T_c . (after [15]).

3.4 Origin of the peak in $\kappa(T)$

The total thermal conductivity of $\text{YBa}_2\text{Cu}_3\text{O}_{7-\delta}$, like other solids, can be viewed as the sum of lattice (κ_{ph}) and electronic (κ_e) components. Therefore, it has long been debated whether the peak in κ of YBCO below T_c is due to electrons or phonons [14, 16]. The arguments in favor and against each interpretation are presented below.

3.4.1 Phonons

Cohn *et al.* [16] attributed the enhancement below T_c of κ in YBCO to phonons, from a more conventional point of view. They pointed out if there is a modest electron-phonon interaction, and if the primary thermal carriers are phonons, then the peak can be explained within the BRT theory due to an increase in the phonon mean free path driven by a decrease in electron scattering, as the pairs condense into the superconducting ground state. As T continues to decrease, $\kappa(T)$ eventually decreases due to the decrease in phonon density along with the dominance of other scattering mechanisms. They made the following observations:

By estimating $\kappa_{e,n}$ using the measured electrical resistivities ρ and the Wiedemann-Franz law, which states that $\kappa_{e,n} \leq L_0 T / \rho$ ($L_0 = 2.45 \times 10^{-8} \text{W}\Omega/\text{K}^2$), they get an upper-limit estimate of the electronic component of $\kappa_{e,n} / \kappa_n \approx 0.3-0.4$ for their speci-

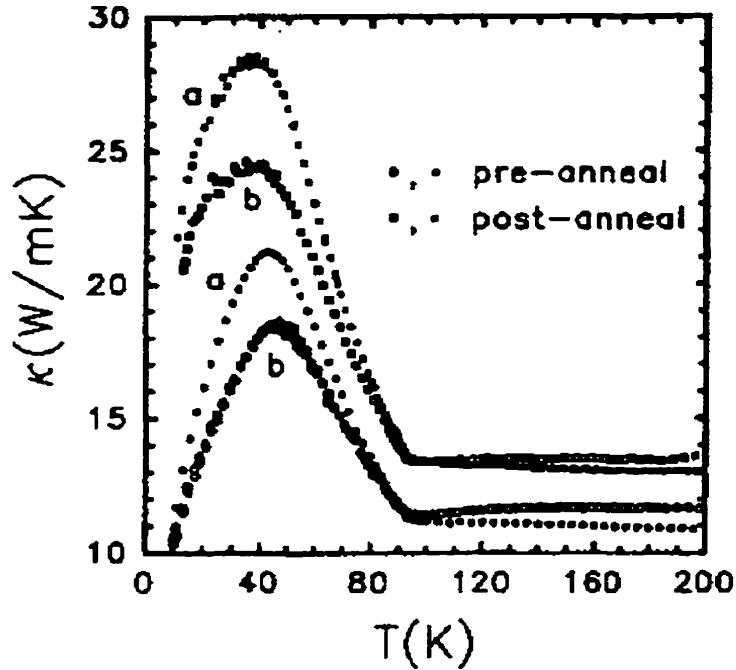


Figure 3.5: Low temperature thermal conductivity vs temperature for the untwinned YBCO crystal before and after oxygen annealing measured by Cohn [16].

men at $T=100$ K. Inelastic scattering of carriers (e.g. by phonons) tends to reduce the Lorenz number from its ideal value L_0 , and hence $\kappa_{e,n}$ could be substantially smaller than this estimate. Therefore, the phonon part in these crystals dominate at least for the temperature range above T_c .

Tewordt and Wölkhausen [17] presented a theory that attempts to describe this scenario in the context of BCS theory. They used BRT theory to calculate the lattice contribution, with the addition of other phonon scattering processes that might be appropriate when describing phonon transport (such as point defects, sheet-like faults etc). The phonon thermal conductivity is then expressed as:

$$\kappa_{ph}(t) = At^3 \int_0^\infty dx \frac{x^4 e^x}{(e^x - 1)^2} \times [1 + \alpha t^4 x^4 + \beta t^2 x^2 + \delta t x + \gamma t x g(x, y)]^{-1} \quad (3.1)$$

where $t = \frac{T}{T_c}$ is the reduced temperature, $x = \hbar\omega/k_B T$ is the reduced phonon energy, $y = \frac{\Delta(T)}{k_B T}$ is the parameter containing the energy gap. The coefficients correspond to the different scattering mechanisms:

1. The coefficient A refers to boundary scattering and is proportional to $L_b = \tau_b v_s$,

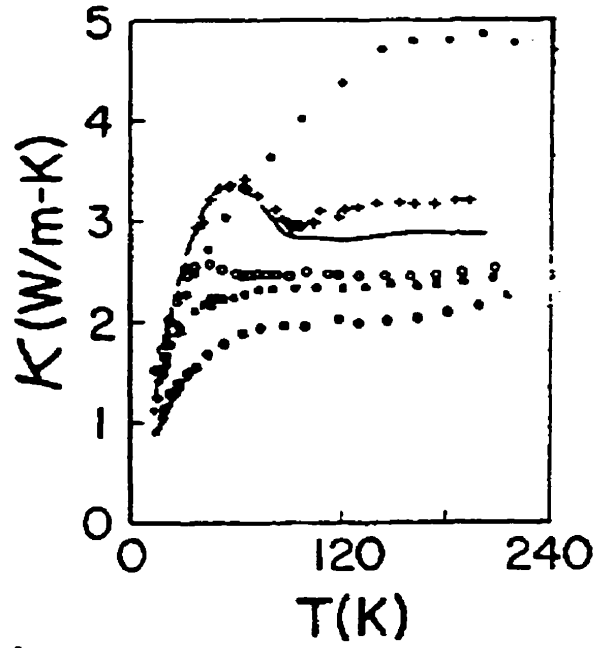


Figure 3.6: Thermal conductivity of $\text{YBa}_2\text{Cu}_3\text{O}_{7-\delta}$ with different oxygen content, (+) original material with $\delta = 0$; (circ) $\delta = 0.3$, $T_c = 70$ K; (*) $\delta = 0.47$, $T_c = 56$; (\odot) $\delta = 0.69$, non-superconducting; (\bullet) $\delta = 1$, non-superconducting.

where L_b corresponds to the outer dimensions of the sample, τ_b is the relaxation time for scattering off the boundaries and v_s is the sound velocity. The full expression for A is: [20]

$$A = \left(\frac{4\pi}{3}\right)^{1/3} (2\pi)^{-1} (k_B^2 \Theta / \hbar a^2) (T_c / \Theta)^3 L_b \quad (3.2)$$

with Θ the Debye temperature and a the average lattice constant.

2. $\alpha t^4 x^4 = \tau_b / \tau_p$ where τ_p is the relaxation time for scattering by point defects [21], and:

$$\alpha = \left(\frac{4\pi}{2}\right) (6\pi^2)^{1/3} (\Delta M / NM)^2 (L_b / a) (T_c / \Theta)^4 n \quad (3.3)$$

where n is the concentration of point defects, and ΔM is the mass difference between the solute and solvent atoms.

3. $\beta t^2 x^2 = \tau_b / \tau_{sh}$ where τ_{sh} is the relaxation time for scattering of phonons by the strain field of sheet-like faults [22], and:

$$\beta = 0.7 (6\pi^2)^{2/3} \gamma_G^2 (T_c / \Theta)^2 N_s L_b. \quad (3.4)$$

here γ_G is the strength of the anharmonic coupling term and N_s is the number of sheet-like faults.

4. $\delta t_x = \tau_b/\tau_d$ where τ_d is the relaxation time due to scattering by the strain field of dislocations.
5. $\gamma t_x g(x, y) = \tau_b/\tau_{e,s}$, arising from the phonon-electron scattering with relaxation time $\tau_{e,s}$. The function $g(x, y)$ is equal to the ratio τ_{en}/τ_{es} of the relaxation times in the the normal and superconducting states, which was derived in BRT theory (for a s-wave gap):

$$g(x, y) \equiv \frac{\tau_{e,n}}{\tau_{e,s}} = (1 - e^x)x^{-1}[2J_1(x, y) + J_2(x, y)] \quad (3.5)$$

J_1 and J_2 has been given in Appendix B of ref [5]. We can express the coefficient γ in terms of the electron-phonon coupling constant λ :

$$\gamma \approx \left(\frac{\pi}{2}\right)\left(\frac{k_B T_c}{\bar{t}}\right)\left(\frac{L_b}{a}\right)\lambda \quad (3.6)$$

where \bar{t} is the effective hopping matrix element for a 2-dimensional tight-binding band of electrons.

Tewordt and Wölkhausen approximate the temperature dependence of the electronic thermal conductivity to be a constant above the superconducting transition temperature. Below T_c , the charge carriers condense into Cooper pairs, which do not transfer heat. The temperature dependence of κ_e for $T < T_c$ is very different depending on whether the electrons are scattered predominantly by defects or by phonons (here electron-electron scattering is ignored). They employed the results of Geilikman *et al.* [23] who tabulated $\kappa_{e,s}/\kappa_{e,n}$, the ratio of the electronic thermal conductivity in the superconducting state and in the normal state, as a function of the reduced temperature. Then:

$$\kappa_e = \begin{cases} K & \text{if } T > T_c \\ K \frac{\kappa_{e,s}}{\kappa_{e,n}}, & \text{if } T < T_c \end{cases} \quad (3.7)$$

where K is an adjustable constant. The sum of eqn. 3.1 and eqn. 3.2 is the model used to fit the measured $\kappa(T)$ of YBCO. For a set of parameters, it certainly confirms the existence of a characteristic peak in κ_{ab} below T_c , as shown in figure 3.7.

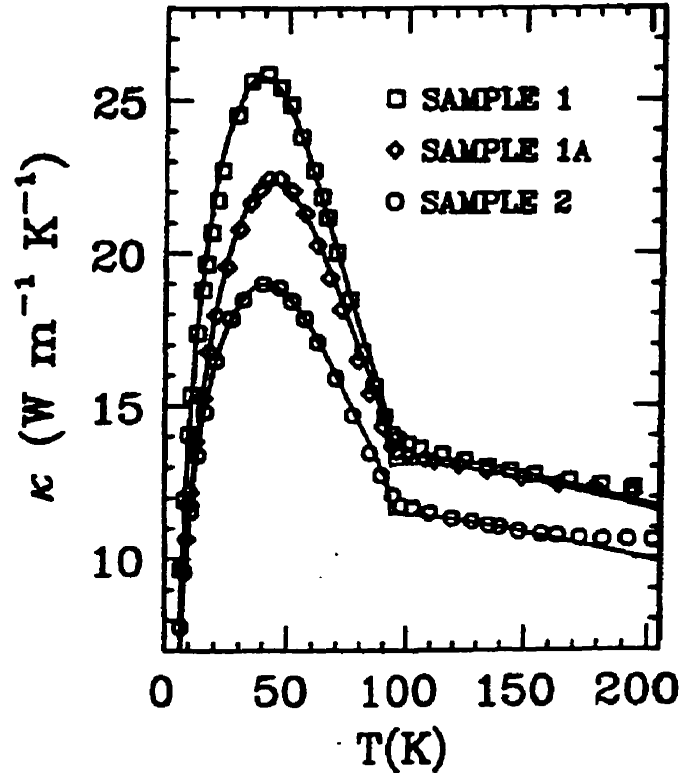


Figure 3.7: Experimental data of ref [24] and theoretical curves calculated by the TW theory [17], showing the thermal conductivity of three different YBCO single crystals.

In a later publication, Tewordt and Wölkhausen extended their model to include the possibilities of strong coupling and d-wave pairing, which could give an even better fit to the data.

While this scenario is able to reproduce the thermal conductivity enhancement below T_c , there are several weak points:

1. A similar phonon peak is also predicted for the out-of-plane thermal conductivity κ_c in this model. Experimentally, as we showed in the last section, none of the existing investigations of κ_c show any such behavior at or below T_c [15]. This point, however, is somewhat weak since the elastic phonon mean free path may be much smaller along \bar{c} .
2. The behavior of the electronic thermal conductivity in the superconducting state has been either neglected or assumed to decrease with temperature as in the BRT treatment discussed before, in which the quasiparticle scattering rate was

assumed to be unaffected by superconductivity. However, these assumptions are not well justified in light of observations of a strongly suppressed quasiparticle scattering rate in microwave conductivity [25] and thermal Hall effect measurements [26], where both showed an enhancement of the mean free path for quasiparticles, as shown in figure 3.8.

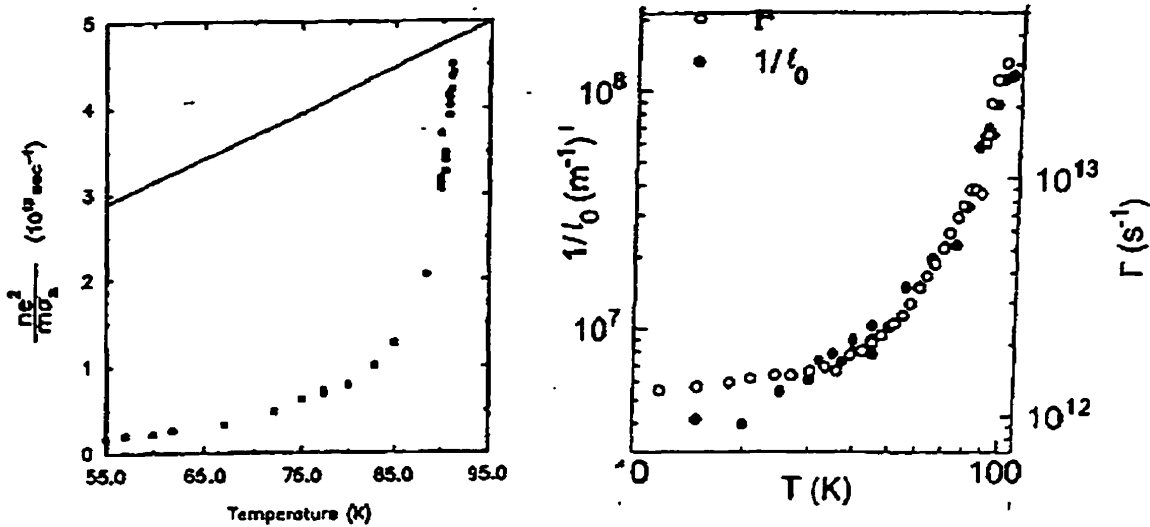


Figure 3.8: Quasiparticle scattering rate in $\text{YBa}_2\text{Cu}_3\text{O}_{7-\delta}$ as estimated from microwave measurement data (left) by $ne^2/m\sigma_n(T)$ and from thermal Hall conductivity (right) by $\sigma_{\text{th}}/\alpha$. The scattering rate falls off rapidly below T_c .

3. In order to account for the large enhancement, the phonon thermal conductivity in the absence of electron-phonon scattering has to be at least as large as the peak value. However, as we mentioned in the last section, the thermal conductivity of an oxygen-deficient, non-superconducting YBCO single crystal is *smaller* than 10 W/mK.
4. And finally, κ calculated under this assumption exhibits a very steep rise at T_c , which is in disagreement with the experimental data that suggest a more gradual upturn.

3.4.2 Electrons

Yu *et al.* [14] proposed an alternative way to explain the observed temperature dependence of the thermal conductivity. Their explanation is based on the observation, in microwave measurements [25], of a similar peak in the temperature dependence

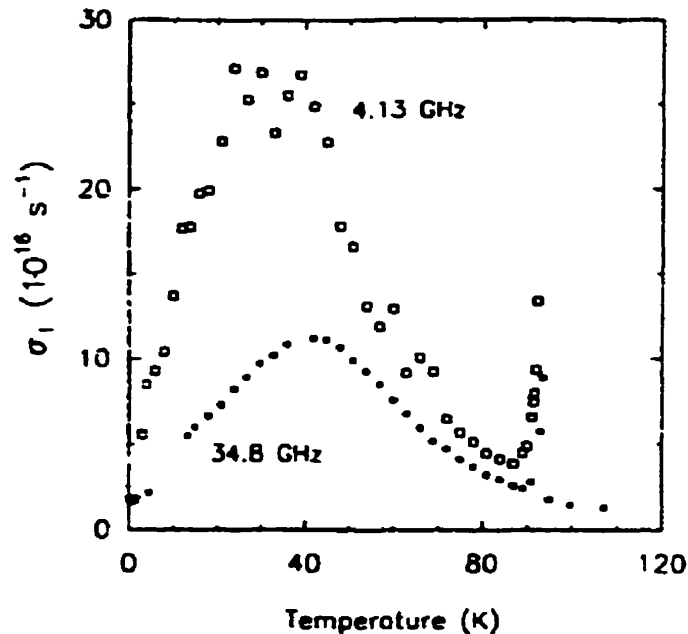


Figure 3.9: microwave conductivity of the detwinned crystal of $\text{YBa}_2\text{Cu}_3\text{O}_{7-\delta}$. The broad peaks below T_c are similar to that in thermal conductivity. This is attributed to the competition between the decrease in the normal-fluid density and a quasiparticle lifetime that increases rapidly below T_c .

of the charge conductivity σ_1 (see figure 3.9), attributing to a strongly suppressed quasiparticle scattering rate. Accordingly, Yu *et al.* associated the peak in κ with the electron contribution, and propose that the strong suppression of the quasiparticle scattering rate with decreasing temperature is responsible for the large enhancement of in $\kappa(T)$ below T_c .

They considered, in normal state, that the total thermal conductivity is expressed as the sum of phonon and electron contributions, assuming the electrical conductivity of YBCO follows $\sigma \propto 1/T$.¹ $\kappa_{e,n}$ should then be temperature independent according to the Wiedemann-Franz law: $\kappa_{e,n} = L_0\sigma T$ (taking the Lorenz number to be the Sommerfeld value) and the phonon thermal conductivity can be expressed by $\kappa_{ph} = \frac{1}{3}c_v v^2 \tau$, with c_v the specific heat of phonon, v the sound velocity, and τ^{-1} the total scattering rate for phonon, which can be expressed as in eqn. 2.5. They assumed the most prominent scattering mechanism for phonon thermal conductivity at high temperature is Umklapp scattering, for which $\tau_{phonon-phonon}^{-1} \propto T$. Other scattering contributions, such as phonon-electron, phonon-defect and phonon-

¹This is not true for the b-axis conductivity.

boundary scatterings, are weakly temperature dependent, which are approximated by a temperature-independent thermal resistivity W_0 . Thus, the total thermal conductivity is $\kappa_n = \kappa_{e,n}^n + 1/(W_0 + \alpha T)$, with W_0 and α constants.

As mentioned before, in the 2-fluid model, the superfluid (superconducting carriers) does not carry any heat. The temperature dependence of the electronic thermal conductivity is dictated by the number density and the relaxation time of the normal-fluid carriers. Since experiments on microwave conductivity of the high- T_c superconductor showed that the quasiparticle scattering rate is much suppressed below T_c , which indicates that the excitations that strongly damp the current-carrying quasiparticles freeze out rapidly below T_c , giving rise to a much enhanced electrical conductivity and hence electronic thermal conductivity. Therefore, the similarity between the microwave conductivity peak and that of the thermal conductivity $\kappa(T)$ in YBCO single crystals suggest that at least part of the peak in $\kappa(T)$ is due to κ_e . They derived the electronic thermal conductivity κ_e from the total thermal conductivity data using:

$$\kappa_{e,n} = \kappa_n - \frac{1}{W_0 + \alpha T}$$

the latter term is the phonon thermal conductivity κ_{ph} . Figure 3.10 shows their result compared with theoretical curves obtained using the formalism of Kadanoff and Martin [11], for different pair-states and gap ratios $g = \frac{\Delta(k, T=0)}{2k_B T_c}$.

In reality, the electron-phonon coupling is finite, and there will be a change in phonon thermal conductivity due to the decrease in electrons available to scatter phonons. However, they assumed that electron-phonon scattering may not be significant in comparison with phonon-phonon or phonon-defect scattering.

As can be seen from figure 3.10, this scenario also gives an good explanation for the appearance of the peak in κ . Some possible problems are:

- They estimate κ_e by simply subtracting κ measured in insulating YBCO from that of the superconductor, which is not justified given that the presence of electrons not only introduces additional scattering of phonons, but also alters the phonon spectrum.
- Their assumption that $\rho \propto T$ and therefore κ_e is constant in the normal state

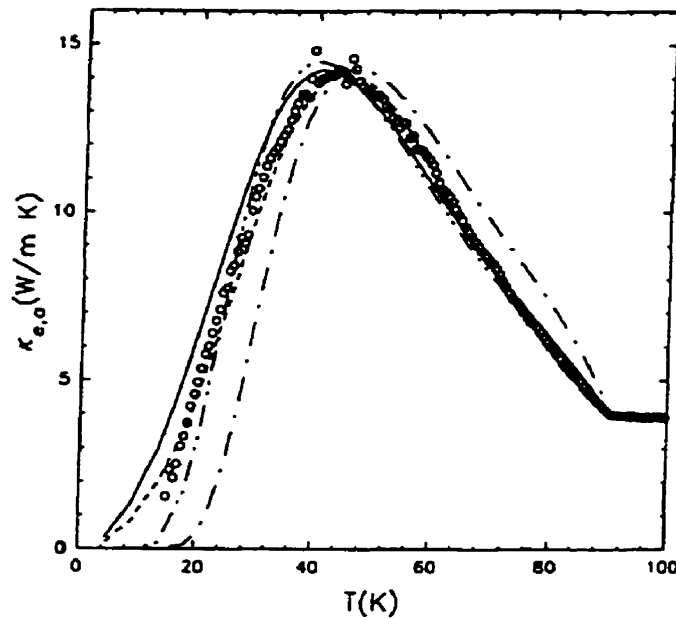


Figure 3.10: Temperature dependence of the κ_e derived from $\kappa - \kappa_{ph}$ (o) and calculated fits using different pair states and different gap-to T_c ratios.

seems inconsistent with our measurement of ρ , which shows, in the b-axis, that there exists a T^2 term due to the electrons in chains [13].

We can see that both explanations have strengths and weaknesses. And it should be stressed that in both cases the excellent fits are qualitative: no assessment of the actual values of the fitting parameters are given. These two scenarios will both be used to explain our measurement of κ in different Zn-doped samples in chapter 5, where some new information will be added to help us distinguish them.

EXPERIMENTAL ASPECTS

High-quality single crystals of $\text{YBa}_2\text{Cu}_3\text{O}_{7-\delta}$ have been grown by self-decanting flux method [27], then annealed in pure oxygen, and finally, detwinned in a pressure cell. After growth, they were characterized by means of a-b plane resistivity, AC magnetic susceptibility, polarized optical microscopy and scanning electron microscopy (SEM). The above procedures and techniques will be described in this chapter. Also included is a description of the apparatus and experimental procedure used for the measurement of the thermal conductivity.

4.1 *Sample preparation*

4.1.1 *Crystal growth*

The fact that YBCO melts incongruently (at $\sim 1020^\circ\text{C}$) limits the techniques for growing single crystals. Only the flux-growth technique, which uses a CuO rich melt has succeeded in producing bulk single crystals so far, and this is the method we adopted. To grow a crystal from the flux, we used the self-decantation technique [27] in which a temperature gradient is applied horizontally along the crucible during the whole process. Thermodynamically, it is favorable for the flux to move to the colder side of the crucible when solidifying, leaving the crystals behind. We applied a temperature gradient of about $4 - 5^\circ\text{C}/\text{cm}$.

We used a mixture of Y:Ba:Cu with molar ratios of 1:18:45, introduced by Wolf *et al.* [28], in yttria-stabilized zirconia (YSZ) crucible. We chose the YSZ crucible because the flux is corrosive and most other kinds of crucibles, like Al_2O_3 , MgO and Au, would introduce impurities in the crystals at the percent level, causing a broadened superconducting transition and a reduced T_c . YSZ is the one that contaminated

the least. (It is reported recently that the use of BaZrO₃ crucible has been shown to contaminate even less [29].)

To make the mixture, we used Y₂O₃ of 99.9999% (6N) purity; BaCO₃, 99.999% (5N); CuO, 99.9999% (6N). The purity of the material is a crucial aspect of the crystal growth: by using the same heating procedure and crucible material but with BaCO₃ and CuO of 99.9% purity, it is difficult to even melt the mixture properly [19].

After placing the powder in the YSZ crucible, the crucible itself was placed in an alumina crucible, which in turn was inserted into a programmable horizontally mounted furnace. The heating program is a combination of that used by Liang *et al.* [30] and that used by Vanderah *et al.* [31]:

1. Heat to 870°C in 4 hours. (we chose a slow heating to avoid a large temperature overshoot).
2. Remain at 870°C for 8 hours. In this stage, BaCO₃ decomposes into BaO for the next stage.
3. Over a period of 2 hours, heat to a temperature between 990 and 1020°C. This is the temperature where melting occurs. (The idea is to reach the lowest temperature for chemical reaction and melting of the starting materials, thereby reducing the amount of impurities from crucible corrosion.)
4. Stay for 4 to 8 hours at this temperature. This stage is to ensure homogeneity of the melt.
5. Cool to 990°C over one hour.
6. Stay at 990°C for 5 hours. The crystals start to grow.
7. Cool to 950 – 970°C over one hour. In this temperature range, crystals and flux coexist.
8. Cool to 930°C at a rate of 0.5 – 2°C/hour. This is the self-decantation stage in which the flux moves to the cold side and the crystals are left behind.

9. Cool to ambient temperature. The natural cooling rate of the furnace is low hence this stage takes about 12 hours. Such cooling results in surface annealing and twinning of the crystals.

4.1.2 Oxygenation

When the samples are taken out of the crucible, they usually have an inhomogeneous and deficient oxygen content. Therefore, at this stage we anneal the samples in a flow of pure oxygen to fill the CuO chains. We heat the sample up to 850°C for one day and then anneal for six days at 500°C. Both Lagraff [32] and Schleger [12] reported that at 500°C and a pressure of one atmosphere, the oxygen deficiency in $\text{YBa}_2\text{Cu}_3\text{O}_{7-\delta}$ is $\delta = 0.08 \sim 0.1$.

4.1.3 Detwinning

Usually, there exist lots of twins on these as-grown samples. The twins are domains with alternating \vec{a} and \vec{b} -direction which result from the structural transition from tetragonal to orthorhombic after growth, when the crystals are cooled and the surface is annealed. The domain structure is shown schematically in figure 4.1. In order to eliminate the twinning we used a stress cell with weight of about 0.5 kg applied along one of the edges of the sample, and kept it at a temperature of 550°C (a temperature found to be a compromise between increased oxygen mobility as the temperature rises, and a proper function of our stress cell), for about 15 minutes. This was done in air and then the crystal is re-annealed for one day at 500°C in flowing oxygen.

4.1.4 Zn-doped crystals

The same procedure is used for growing $\text{YBa}_2(\text{Cu}_{1-x}\text{Zn}_x)_3\text{O}_{7-\delta}$, except that a certain amount of ZnO is added into the initial mixture, depending on the desired level of doping. The Zn concentration of our crystals is determined from a measurement of T_c (via susceptibility or resistivity) using the known relationship between Zn concentration and T_c for polycrystalline samples [33]. The concentration is roughly 60% of that put into the melt, which is close to 2/3, a fraction one would expect for an ideal solution model where the Zn only occupies the Cu sites in the CuO_2 plane.

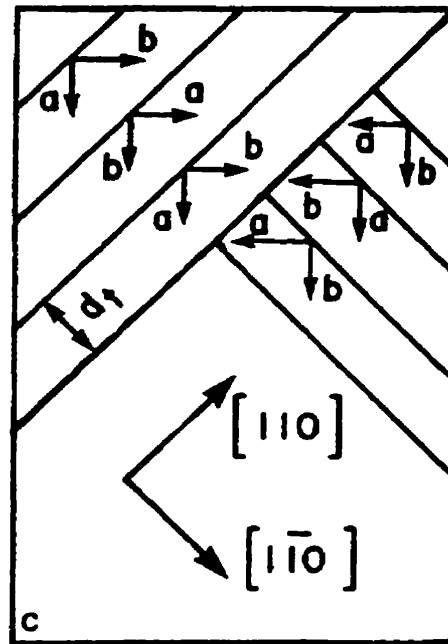


Figure 4.1: Schematic representation of a twinned crystal, showing the lamellar domains; the domain width d_t is of order one micron.

4.2 Sample characterization

4.2.1 Polarized optical microscopy

After annealing the sample, but before detwinning, we employed a polarizing microscope to observe twins in the a-b plane. Figure 4.2 shows optical effects on the a-b face of a YBCO crystal. The crystal is placed under an optical microscope, with its c axis vertical. White light from an external tungsten lamp is directed toward the sample at a large angle from the c axis, the reflected beam is not in the field of view and the crystal remains dark except if the incident beam is perpendicular to the $[110]$ or $[\bar{1}10]$ direction. Under these conditions, the white light dispersion reveals one family of domains.

This way, one can estimate roughly what fraction of the sample is twinned, how many twin domains exist and how large the twin domains are. Before detwinning, the number of twins in one orientation, in general, is about the same as in the other. As a result, transport properties on twinned crystal tend to be an average over both \vec{a} and \vec{b} . After detwinning, some samples can be fully detwinned while others be 10% or less.

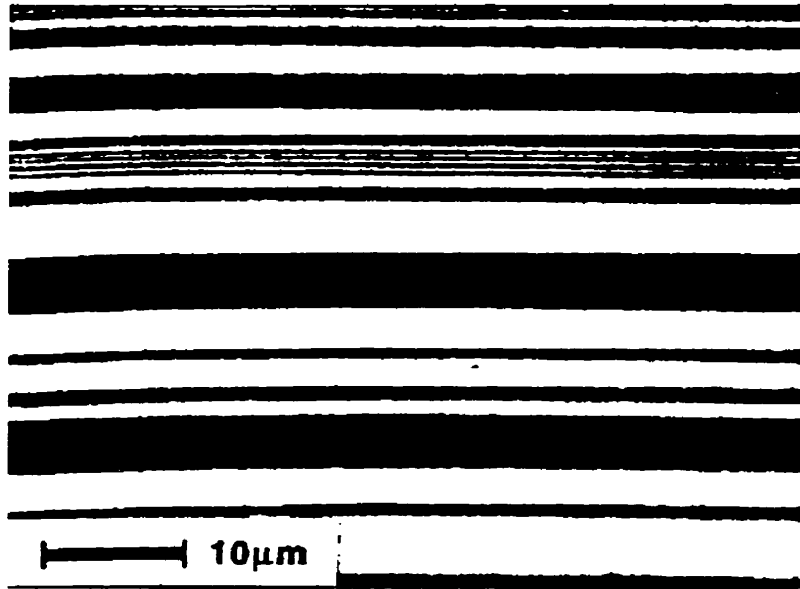


Figure 4.2: Picture of a small area of a twinned sample as seen in the polarized optical microscope when the polarizer and the analyzer are parallel to each other. The black and white areas are a-axis and b-axis domains, respectively.

Generally, the remaining twinned part is in one of the corners, due to unequal stress applied on the sample. As for the domain size, the spacing of twin boundaries in a typical twinned crystal is around 10000\AA for pure crystals and is observed to decrease with increasing Zn doping. Actually, the twin boundaries are so closely spaced in the $x=3\%$ sample that they are no longer visible under visible light, indicating a spacing less than 4000\AA .

4.2.2 *Electrical resistivity*

We measured the electrical resistivity of each crystal used in this work, to determine the transition temperature (T_c) and the transition width (ΔT), both are indications of the quality of a crystal. One of the advantages of our set-up is the ability to measure the electrical resistivity using the same contacts as employed for the thermal conductivity, as shown in figure 4.4. The motivation for such a design was to allow a measurement of the Lorenz number, free from geometric factor uncertainties. We use silver wires ($100\ \mu m$) to make the contact which is glued by silver epoxy on the sample. the electrical and thermal resistance of these contacts are smaller, because of the good conductance of silver, the electrical resistance was typically $\sim 100m\Omega(3.5m\Omega)$

at room temperature (helium temperature). We should note that in this set-up, one can measure either ρ_a or ρ_b , but not both. For a relation between the two quantities on the same sample, one employs the Montgomery method (see for example, R.Gagnon *et al.* [13]).

The temperature dependence of the resistivity is measured using a LR-700 resistance bridge (with a multiplexer) for both the thermometer and the sample. A typical result is shown in figure 4.3. The transition temperature is narrow (0.2 K) for pure crystals and broadens (1.5-2 K) when doped by Zn, as will be shown later. No obvious difference was observed between twinned and detwinned crystals.

4.2.3 Scanning electron microscopy

We employed SEM to examine the morphology of a sample and to measure its dimensions, which gives us a good estimate of the geometric factor used in the calculation of the absolute value of conductivity (thermal or electrical). A typical SEM photograph is shown in figure 4.4. This way, the uncertainty on the geometric factor can be restricted 10% or less, with the main source of the uncertainty being the width of the contacts and irregularities in the sample shape.

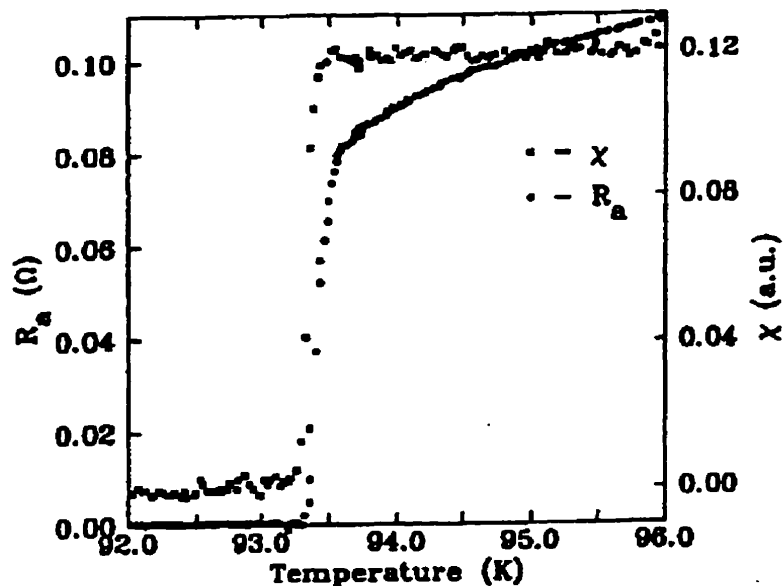


Figure 4.3: The transition temperature measured by resistivity (○) and susceptibility (□)

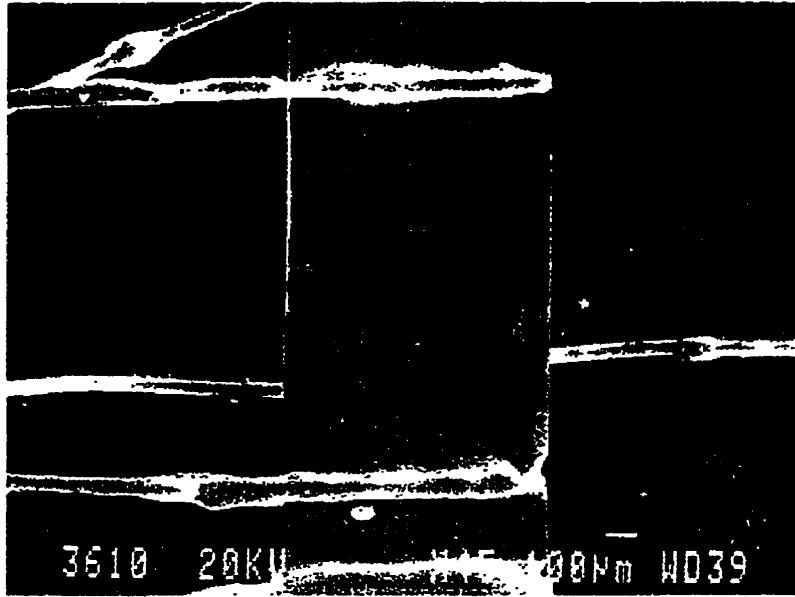


Figure 4.4: The SEM image of one of our crystals. The width of the contact is a main source of geometric factor uncertainty.

4.2.4 Magnetic susceptibility

We also employed AC magnetic susceptibility for the determination of T_c . This is the preferred method because it does not require any special preparation (*e.g.* contacts), and it is more sensitive than resistivity to possible inhomogeneities. The susceptibility apparatus is shown in figure 4.5.

While the sample is in the normal state, its susceptibility is negligible, and as the temperature drops below the transition point, magnetic flux is screened out of the sample and the effective volume of that secondary coil drops, which results in a change in the total e.m.f. picked up. Figure 4.3 shows a comparison of the magnetic susceptibility (χ) and electrical resistivity (ρ) of a pure YBCO crystal, in the vicinity of the superconducting transition. One can see the very narrow transition ($\Delta T \approx 0.1$ K in χ and 0.2 K in ρ), which is evidence for high quality and homogeneity of the sample.

4.3 ^4He cryostat

We used an insertable ^4He cryostat to achieve low temperatures, such as that described in detail by Swartz [34]. It has the advantages of low helium consumption,

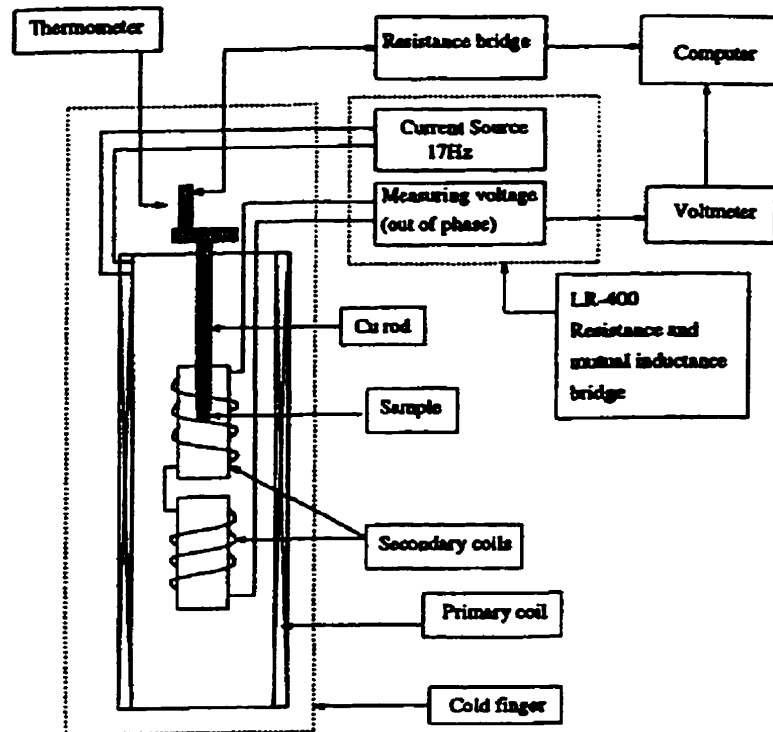


Figure 4.5: Susceptibility apparatus: one resistance bridge is used for reading the thermometer and another bridge to measure the susceptibility in mutual inductance mode.

fast cool-down and warm-up times and good temperature stability from 1.2 K to room temperature. This kind of cryostat is immersed into liquid ^4He in a storage Dewar. The liquid ^4He provides cooling down to 4.2 K, while cooling to 1.2 K is achieved by pumping on an internal "pot" of ^4He . The portion that is inserted into the Dewar is shown in figure 4.6, and described in the following.

1. Wiring: 38 wires are used in our set-up, connected to two 19-pin hermetically sealed electrical feedthroughs, on the upper portion of the cryostat. Half of the wires we used are copper, gauge 36 (for good electrical connection), half are manganin, gauge 36 (for limiting thermal conductance). The wires are contained in the tube used for evacuating the can. In order to restrict the heat flow down into the can, these wires are anchored at 2 stages: on top of the vacuum can (4.2 K) and on the sample stage. The sample stage is connected to the internal pot by a brass threaded rod, which provides an appropriate thermal link for the smooth control of the sample temperature.

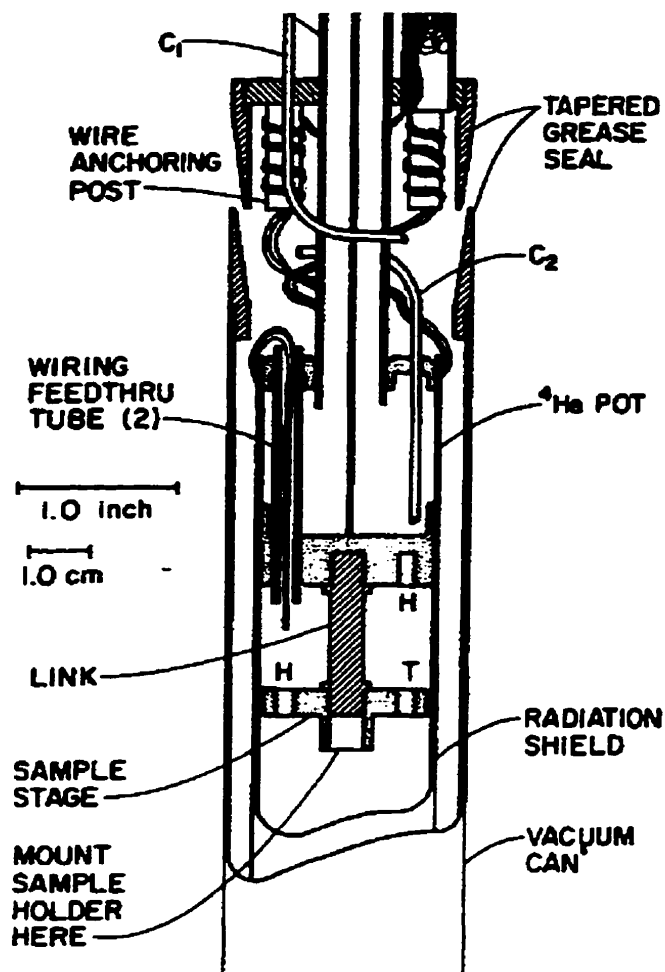


Figure 4.6: Low-temperature portion of the ^4He insertable cryostat, the tube marked C_1 and C_2 are capillary feed-through tubes for use with a continuous fill capillary. the 2 positions on sample stage marked T,H are to place thermometer and heater respectively.

2. Heater and thermometer: the temperature is controlled by using one of two calibrated thermometers: Pt (30-150 K) or Ge (1.0-75 K) (position T in figure 4.6). The heater is fixed on the upper surface of the sample stage (position H in figure 4.6). Although, there is a distance between the regulating thermometers and the sample, the sample holder has been designed for good thermal conduction, so no significant temperature gradient was found. We used an extra cernox thermometer on the sample mount to check this before starting measurements.
3. Vacuum can: as shown on top of figure 4.6, a tapered grease seal is used for the vacuum can. This makes it easy to attach and takes up only a small fraction of the available cross-sectional area. We employ a diffusion pump to achieve

the high vacuum, by which we can get vacuum as good as 10^{-7} torr. This is necessary for the accuracy of κ measurement, which will be discussed later.

4. Cooling procedure: First, the vacuum can is evacuated. In order to speed the cooldown, a few cubic centimeters of helium gas are added to the vacuum can, then the cryostat is inserted into a container of liquid nitrogen (LN_2) until the temperature of the pot is reduced to below 100 K. With helium gas in the vacuum can, this will take only about 15 minutes. (otherwise, it would take about 5 hours or more.) This gas will be evacuated after the low temperature has been achieved. Once the cryostat has cooled to LN_2 temperature, the second step is to insert it into a helium dewar to reach 4.2 K. After the thermometers are stable at 4.2 K, there should be some liquid helium inside the pot which is critical in the next step. We can obtain this by pressurizing the pot with a ^4He gas cylinder, and afterwards, by pumping on the pot one can then reach lower temperatures (down to 1.2 K). However, in practice, we didn't go to any temperatures lower than about 3.5 K. The temperature range used for most of our measurements was 4 to 150 K.

4.4 Thermal conductivity set-up

The technique we used to measure thermal conductivity is the so-called longitudinal steady-state method — analogous to a potentiometric measurement of the electrical resistivity. For every recorded point, the temperature of the sample is stabilized at some temperature T_0 , and then a constant heating power is applied to one end of the sample. At equilibrium, the temperature gradient across the sample is measured and thermal conductivity is then given by:

$$\kappa = \frac{\text{power}}{\text{temperature gradient}} \times \text{geometric factor} \quad (4.1)$$

The set-up is illustrated schematically in figure 4.7. We call this the 4-probe method (requiring a cold bath at one end, a heater at the other and two thermometers in between).

To the sample we attached with silver epoxy four $100 \mu\text{m}$ silver wires (now being replaced by $50 \mu\text{m}$ ones to reduce geometric uncertainty) which are connected to

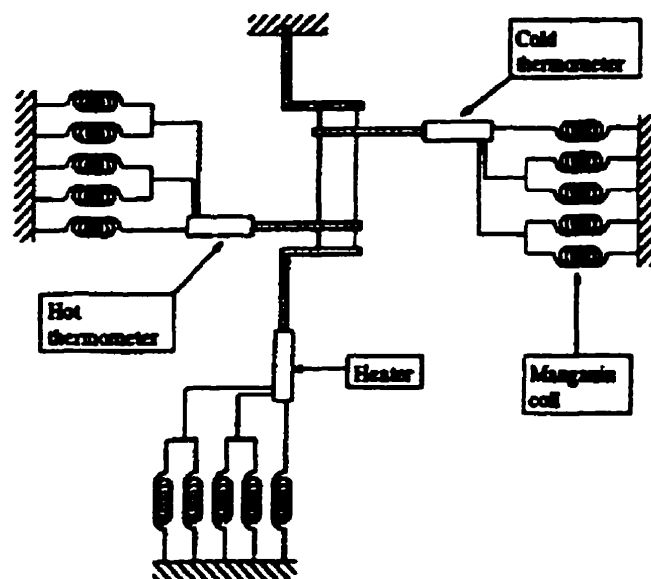


Figure 4.7: A detailed drawing of the thermal conductivity apparatus is shown on the left. Ag wires are epoxied along the sample, perpendicular to the direction of current, the manganin coils are connected to the electrical leads of the probe.

the heater, thermometers, and heat sink. We used manganin coils ($\sim 40\Omega$ of $25\ \mu\text{m}$ wire) for measuring the electrical resistance of heater and thermometers. These wires give negligible heat loss to the Cu base because of their high thermal resistance (see figure 4.7).

A constraint is the size of the thermometers and heater. The following points are considered: 1) the radiative heat loss from the heater is proportional to its surface area, as described later, so, the smaller the size, the smaller the loss, 2) the equilibration time of the thermometers can be reduced if we use smaller thermometers, 3) the longest dimension of the sample is approximately 2 mm, which serves as a reference size for the other parts. As a result, we chose to use $20\ \Omega$ cernox thermometers from Lakeshore, with a size of $1 \times 1.5\ \text{mm}^2$. The temperature dependence of these sensors is very good, as shown in figure 4.8. As for the heater, we bought some semiconductor-film resistors of $1.5\ \text{k}\Omega$, for their weak temperature dependence (except at temperatures below 10 K, when its resistance increases fast), and their small size ($1.5 \times 1.5\ \text{mm}^2$). The heater resistance is much higher than that of the manganin coils (i.e. $1.5\ \text{k}\Omega \gg 40\Omega$ in this case), so the power is dissipated almost

entirely in the heater, which is in good thermal contact with the sample.

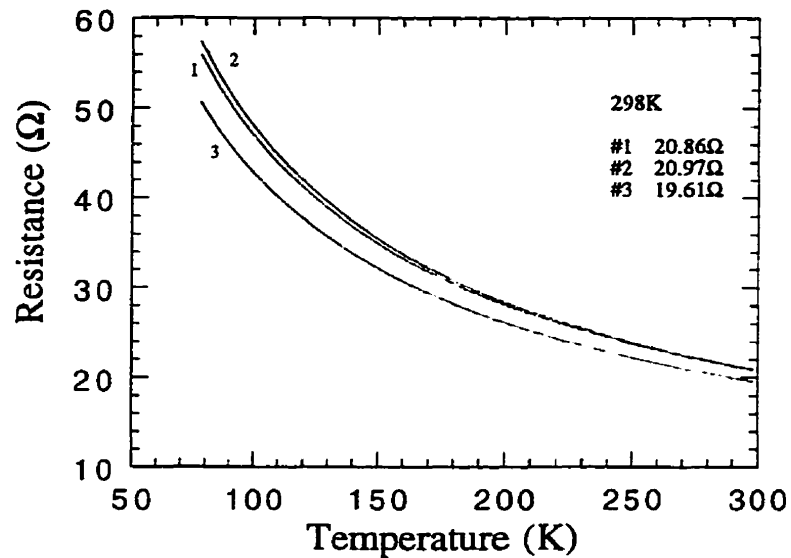


Figure 4.8: Resistivity vs temperature of three cernox thermometers. We used #1 and #2 to measure the sample temperature gradient.

As we said at the beginning, the electrical power \dot{Q} dissipated in the heater provides a heat flow, and the pair of thermometers (separated by a distance L through a cross section S) measure the temperature difference ΔT along the specimen. Provided ΔT is not too large, the value of the thermal conductivity obtained from eqn. 4.1 will be that corresponding to the mean temperature between the two thermometers, even if the thermal conductivity varies with temperature. Uher [35] showed that the difference between the true thermal conductivity and that derived from eqn. 4.1 is less than 0.25% (for $\Delta T/T = 0.1$ and $\kappa \propto T^3$). In our experiment we keep $\Delta T/T = 4\%$ in the whole temperature range.

To use the longitudinal steady-state method effectively, we must make sure that all the heat generated by the heater flows through the specimen to the cold side. As the thermal conductivity of the high- T_c materials is, in general, rather low, we should be very careful about the following factors: First, the choice and size of the wires connecting the heater and thermometers to the sample, so that heat loss is kept to a minimum. This is why we use manganin coils (40 gauge) to measure the thermometers and heater. Let us estimate the heat leak through these coils. The thermal conductivity of manganin at 150 K is $13 \text{ Wm}^{-1}\text{K}^{-1}$ [36], and we can

calculate its conductance to be $4.2 \times 10^{-8} WK^{-1}$. For our YBCO sample, a typical value of the thermal conductance is $2 \times 10^{-7} WK^{-1}$ at 150 K. With such a ratio, the heat loss through these coils is negligible compared with the heat flow through the sample. This is still true, if we also include the thermal resistance of the contacts between heater and sample, sample and heat sink, which are around $10^4 W^{-1}K$. In the latter case, we got a total conductance of $\frac{1}{2} \times 10^{-4} WK^{-1}$, still much higher than that of manganin coils. Secondly, good vacuum must be maintained in the can to eliminate heat exchange with the surrounding medium by conduction through residual gas. In our experiments the pressure in the sample chamber is around 10^{-7} mbar, so the mean free path of the gas molecules is larger than the distance between the thermal conductivity apparatus and the chamber cover, the convection could be safely neglected. According to ref [36]

$$\dot{Q}_{conduction} = 0.016a_0p_{mm}(T_2 - T_1) \quad (4.2)$$

where p_{mm} is the pressure in mm of Hg, and $\Delta T_{heater} = T_2 - T_1 = 5 K$, a_0 is related to the individual accommodation coefficients and the areas of surface (always smaller than 1), we get $\dot{Q}_{conduction} = 0.25 \mu W$. A typical \dot{Q} through the sample is $\kappa\Delta T$ around $3 mW$, so this is again a negligible effect. Thirdly, there are heat losses by radiation. This is more significant at high temperatures and effectively limits the temperature up to which this method is applicable. Experimentally, we found that by supplying the heater with a power of 0.25 mW, its temperature increases by $5 - 5.5^\circ C$ at $T=150$ K. Assuming an emissivity factor $\epsilon = 1$ for the heater surface (the worst case), the heat lost by the heater can then be estimated from:

$$\dot{Q}_{rad-loss} = \sigma A[(T + 5)^4 - T^4] \quad (4.3)$$

where $\sigma = 5.67 \times 10^{-12} W/cm^2K^4$ and A the surface of the heater. Using the heater surface area ($225 mm^2$), we got $\dot{Q}_{rad-loss} = 0.12mW$ at 150 K. This represents about 5% of the heat through a typical YBCO crystal at this temperature, therefore we kept our measurements below 150 K. This heat loss is down to $\sim 1\%$ at T_c .

The electrical circuit of the thermal conductivity apparatus is very simple, as shown in figure 4.9. The limiting resistors R_L are thin film resistors of $10 k\Omega$, and the resistance of the thermometers (R_1 and R_2) and the manganin coils (R_{M1} and

R_{M2}) are less than 1% of R_L throughout the temperature range of this experiment. This ensures that the current applied is always the same. Furthermore, because we calibrate the thermometers for every data point (at every temperature T_0), effects of hysteresis do not affect the results.

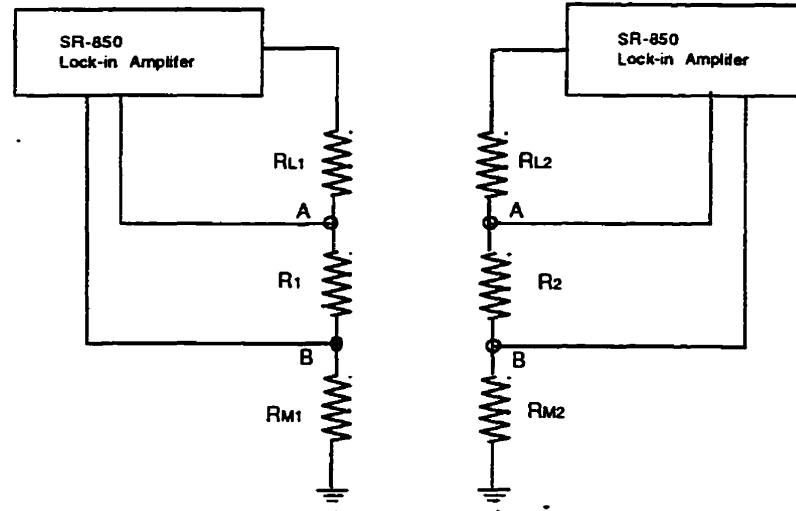


Figure 4.9: The electrical circuit of the experiment. $R_{L1,2}$ are limiting resistors of $10 \text{ k}\Omega \pm 1\%$, $R_{1,2}$ are the thermometers ($20 - 60 \Omega$) and $R_{M1,2}$ are the manganin coils (20Ω).

4.5 Experimental procedure

We systematically measured twinned Zn-doped crystals $\text{YBa}_2(\text{Cu}_{1-x}\text{Zn}_x)_3\text{O}_{7-\delta}$ (with $x = 0\%$, 0.15% , 0.6% , 1.0% and 3.0%) and detwinned samples with Zn(0% , 0.6% , 2% and 3%). In all cases, we started the measurements after cooling the cryostat down to liquid helium temperature, The temperatures T_{cold} and T_{hot} , are measured by using two SR 850 lock-in amplifiers from Stanford Research System. The two lock-in sends a low frequency ac voltage, which is converted into a current by means of the $10 \text{ k}\Omega$ limiting resistor, the voltage drop across each thermometer is detected and converted into resistance. because the limiting resistances (R_L) are very high, consequently, the current applied on the thermometer is almost always the same. This procedure is done both *before* and *after* applying the heat on for each set point. One therefore obtains an in-situ calibrations of the thermometers and use these calibration to obtain the two temperatures T_{cold} and T_{hot} . This method can be schematically demonstrated in figure 4.10. the gradient of temperature is simply $T_{hot} - T_{cold}$, and κ is finally

calculated using eqn. 4.1.

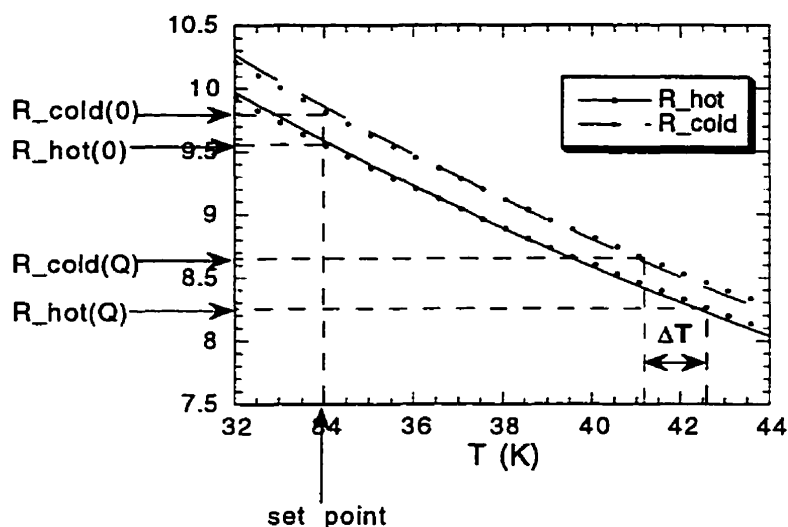


Figure 4.10: Demonstration of analysis performed in order to extract the thermal conductivity. The circles (open for T_{cold} and closed for T_{hot}) represent the data points used to obtain the calibration (solid and dashed lines). In this example, temperature is set by temperature controller to 34 K, and the temperature gradient (ΔT) is simply the difference between the two temperatures read from the in-site fit curve after the heat is applied. The sample temperature is the average of the two.

The following are several details on the measurement:

1) To measure thermal conductivity in the steady state, the temperature has to be extremely stable. We achieved this by continuously measuring the temperature with a temperature controlling program (say, at a rate of 6 times/min), and analyzing the data. We set two criteria: 1) the difference between the actual temperature and set point temperature should be smaller than a certain value (say, 0.01 K) and 2) the rate of change of T (obtained by calculating the slope of the a few past data) should be smaller than some set value. Both of these criteria have to be satisfied before the next step is taken.

2) Once the temperature of the probe is stable, we apply heat, and wait until the apparatus reaches equilibrium. The waiting time depends on temperature (via heat capacity and thermal conductivity), so we have to set a longer waiting time as the temperature increases. We achieve this by applying the same technique as in step (1), except that we read the data with two lock-in amplifiers, one for each thermometer. We analyze sequentially the readouts and impose criteria for temperature stability.

3) For each data point, the system records a) the potential across the two thermometers, before and after heat is applied: $V_{cold}(Q = 0)$, $V_{hot}(Q = 0)$, $V_{cold}(Q > 0)$ and $V_{hot}(Q > 0)$; b) the heater voltage while being heated with current (I); c) the sink temperature (T_0) as obtained from a calibrated Ge or Pt thermometer. By the way introduced in the beginning of the section, using the measured curve of $V_{cold}(T)$ and $V_{hot}(T)$ for the thermometers *without heat*, in isothermal conditions we obtain the temperature difference between the thermometers *with heat*, $\Delta T = T_{hot} - T_{cold}$. The thermal conductivity is then given by $\kappa = (I \times V_{heater})/\Delta T \times (\text{geometric factor}) \approx I^2 R/\Delta T \times (\text{geometric factor})$. In practice, we should keep $\Delta T/T$ constant. To achieve this, we take the data collected so far, use the formula above to obtain κ , and feed it back into the programme to determine the value of I to be used for the next point, where $I = \left(\frac{\kappa T \times (\Delta T/T)}{R \times \text{geometric factor}}\right)^{-\frac{1}{2}}$. In this way, we kept $\Delta T/T$ to roughly 4% for the whole temperature range.

Besides measuring κ of different Zn-doped twinned crystals, we also measured detwinned crystals to study the anisotropy of κ in \vec{a} and \vec{b} directions. To get a true comparison, we measured a-axis and b-axis crystals from the same batch. Again, we measured samples with different level of Zn-doping.

4.6 Test on a gold sample

In order to test the accuracy of our set-up, we measured a well-known material — gold. There are two purposes for this:

- check that our experimental set-up is suitable at low temperature by confirming Wiedemann-Franz law (below 20 K).
- estimate the extent of heat losses at high temperature (above 150 K)

As discussed earlier in section 2.1.5, the ratio of the electronic thermal conductivity over electrical conductivity is proportional to temperature, therefore, verification of the WFL on a metallic sample would certainly demonstrate the validity of our thermal conductivity set-up.

In order to achieve this, measurements of both the thermal and electrical conductivity were carried on gold wire. They are measured using the same contacts, as a

result, we can obtain the Lorenz number without geometric uncertainty, this is a main advantage of our set-up. The geometry of the sample was chosen such that its heat conductance would be comparable to the least conducting of the YBCO samples. We used an impure iron-doped gold wire (which is actually a Gold-Iron thermocouple wire with .07% Fe) with dimensions $50\mu\text{m}$ in diameter, 10 mm in length (7mm between the thermometers). This gives a thermal conductance of around $6.5 \times 10^{-5} \text{W/K}$, 4 times *smaller* than the lowest conductance of our YBCO crystals, which is around $3.0 \times 10^{-4} \text{W/K}$ at $T = 4 \text{K}$.

Figure 4.11 shows the thermal conductivity of the Au sample measured from 10 K to 60 K. The residual electrical resistance at low temperatures (4.2 K) is $0.042 \times 10^{-8} \Omega\text{m}$. Our main concern is to use the linear part of κ where the electrons are mainly being scattered by impurities at low temperatures to calculate the Lorenz number.

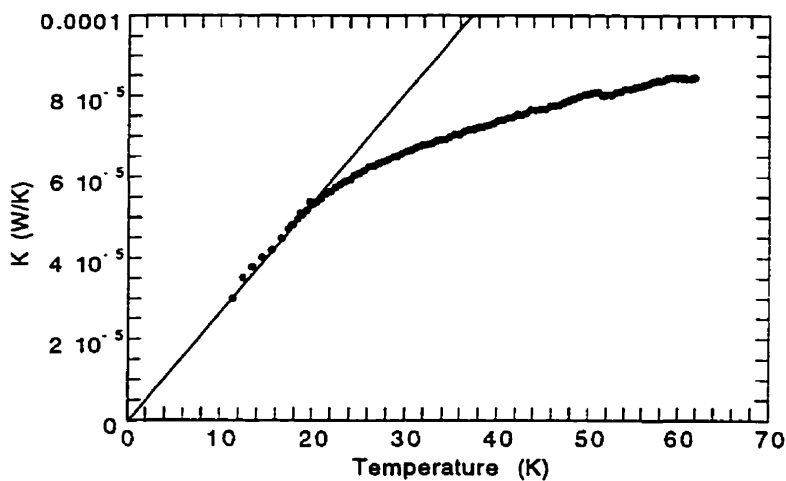


Figure 4.11: Thermal conductivity of Au sample (Gold-Iron with 0.7% Fe) at low temperature, one can observe a linear part below 20 K, with a slope of $2.7 \times 10^{-6} \text{W/K}^2$.

Below 20 K, we got a slope of $2.7 \times 10^{-6} \text{W/K}^2$ for κ_{gold} , from which we estimate the Lorenz number at this temperature to be $2.7 \times 10^{-8} \Omega\text{W/K}^2$, a value greater than L_0 . This is strange at first glance, however, the gold sample we used is pretty dirty, so the electronic contribution is suppressed largely by impurities; therefore, it appears that we should not neglect the phonon part completely. From the theory of phonons, we know in this temperature range, phonons are scattered by electrons mainly [37].

The thermal resistance of phonons scattered by electrons can be expressed as:

$$W_e^{-1} = 3.67 \left(\frac{T}{\Theta} \right)^2 \kappa_{el,\infty} \quad (4.4)$$

where Θ is the Debye temperature. This way, we estimated the phononic thermal conductivity to be 5 W/mK – about 7% of κ_{total} , at $T=20$ K. After subtraction of this contribution, we got the pure electronic part, and re-estimated the Lorenz number to be 2.5×10^{-8} W/Km. this is within 2% of the Sommerfeld value.

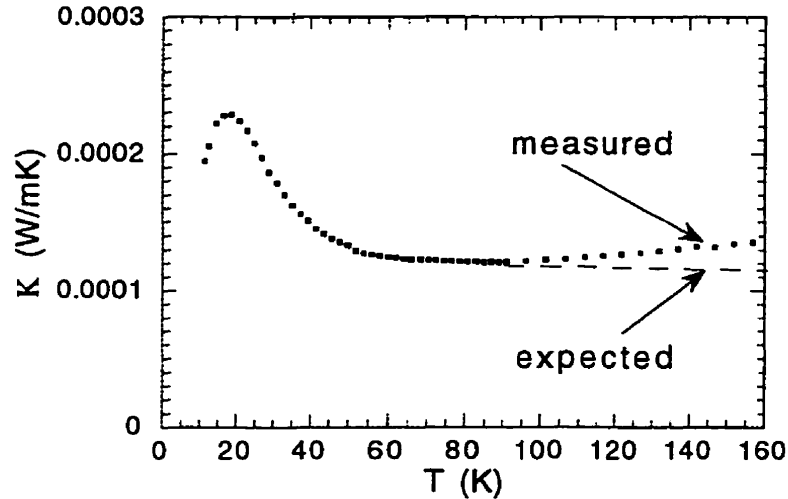


Figure 4.12: κ vs temperature of a pure Au sample, dash line is from the publish data of pure gold sample [36]. The heat loss is significant (15%) in the temperature above 160 K.

As to the second purpose, we measure another gold wire in higher temperature, in order to compare with the published data of pure gold. The sample is 99.99% in purity, 50 μm in diameter and 4 mm in length. The κ is measured up to 160 K in order to learn the importance of the heat loss in this temperature. The results are shown in figure 4.12. We found that the heat loss is significant near 150 K, mainly due to radiation. According to the published data, κ is nearly flat between 100 K to 200 K, so we found that $\kappa_{measured}$ is about 15% higher than expected at $T = 150$ K, corresponding to a heat loss of 0.8 mW, which is a little bit smaller than the estimation of radiation heat loss we made in section 4.4, 0.12mW (because there we took the emissivity factor $\epsilon = 1$). Considering the thermal conductance of this sample is $1.3 \times 10^{-4} W/K$ at 150 K, about 5 times smaller than the lowest conductance of our YBCO crystal, the results confirm that below 150 K, the heat loss is less than

5% for measurement of YBCO sample and thus, our experimental set-up is reliable during this temperature range.

RESULTS AND DISCUSSION

5.1 Introduction

As mentioned in chapter 1, the two aspects of our work are:

- The effect of Zn-doping on the κ of twinned and untwinned YBCO samples.
- The anisotropy of κ in the ab-plane of YBCO.

We present our results and offer a discussion in terms of related experimental studies and theoretical models in this chapter. But before that, let us summarize here what previous work has been done on these two issues.

On the anisotropy, only 2 previous measurements, as mentioned in chapter 3, but their results disagree with each other [14, 16]. On the Zn-doping studies, we want to mention the following:

- Ting *et al.* measured κ for Zn-doped YBCO sintered powder [38], they observed a small peak below T_c for the pure sample (figure 5.1), and also noticed that doping with Zn depresses the maximum in $\kappa(T)$. Particularly, only a smaller enhancement of $\kappa(T)$ below T_c for 1% Zn dopant, and no clear maximum can be observed for 2% (or higher) Zn content which is still superconducting with a T_c of 72 K.
- P.F. Henning *et al.* have recently reported measurements of $\kappa(T)$ for a Zn-doped YBCO single crystal [39], their results are reported in figure 5.2. They showed that impurities suppress the amplitude of the peak in $\kappa(T)$ and shift it to somewhat higher temperatures. Their measurement is done on twinned crystal, and a very puzzling feature is that, the ratio of $\kappa(\text{peak})/\kappa(100K) \approx 1.6$,

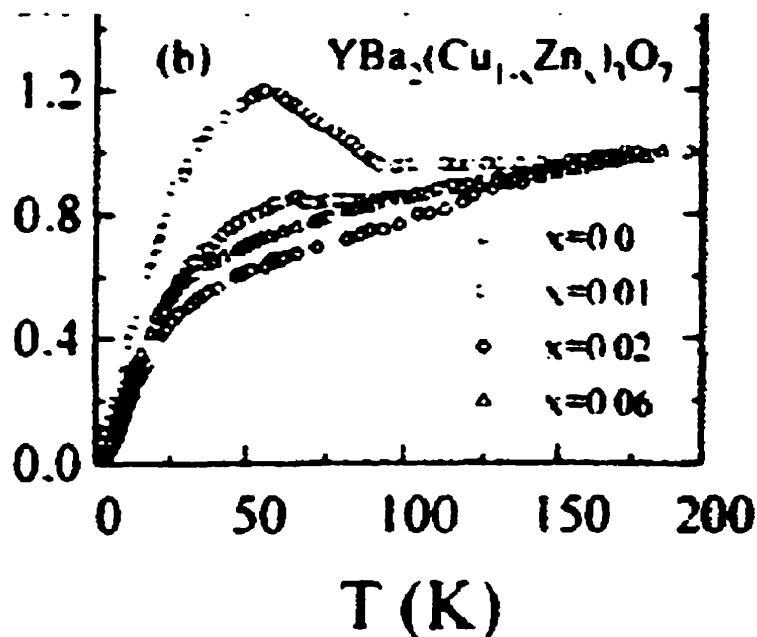


Figure 5.1: $\kappa(T)/\kappa(180)$ vs T for $\text{YBa}_2(\text{Cu}_{1-x}\text{Zn}_x)_3\text{O}_{7-\delta}$ with $x=0.0, 0.01, 0.02,$ and 0.06 . measured by Ting *et al.* on sintered powders [38].

for pure crystal, while the ratio for 3% Zn-doped is higher (≈ 2.2), although the absolute value of the peak is suppressed in the latter case.

5.2 Peak in $\kappa(T)$: effect of Zn impurities

5.2.1 Results

Charge conduction (normal state)

We begin by presenting our results for the normal state charge conduction. We have measured the resistivity of both twinned and detwinned crystals with different Zn concentrations from 0.0% to 3.0%. The results are shown in figures 5.3 and 5.4. The sample characteristics are listed in tables 5.2.1 and 5.2.1.

Here ρ_0 means the extrapolated value at $T=0$ from a linear fit in the range 130 - 250 K, while ρ_0^* is the extrapolated value after adjusting the slope ($d\rho/dT$) for each curve to be $1 \mu\Omega\text{cm}/\text{K}$ for the detwinned crystals and $0.611 \mu\Omega\text{cm}/\text{K}$ for the twinned crystals. Note that the linear fit is perfect for the detwinned (a-axis) samples but not so for the twinned. This adjustment of the slope is based on the assumption that Zn impurities only introduce a simple elastic scattering of electrons, as suggested by

Table 5.1: The geometric factor, T_c and resistivity of our twinned $\text{YBa}_2(\text{Cu}_{1-x}\text{Zn}_x)_3\text{O}_{7-\delta}$ crystals, with $x=0.0\%$, 0.15% , 0.6% , 1.0% and 3.0% . (The geometric factor of pure crystal is not available). ρ_0 is the residual resistivity ($T=0$ K) obtained by linear extrapolate on (130-250 K) and ρ_0^* is obtained in the same way after adjusting the curves to have the same slope.

Sample (Date of growth)	$X(\%)$	Geometric Factor (m^{-1})	$T_c(\text{K})$	ρ_0 ($\mu\Omega\text{cm}$)	$\frac{d\rho}{dT}$	ρ_0^* ($\mu\Omega\text{cm}$)	$\frac{d\rho^*}{dT}$
31-08-95A	0.0	-	93.7	-	-	-3.52	0.611
29-09-94A	0.15	15385(10%)	91.7	-4.2(4)	0.57(6)	-4.43	0.611
04-08-94A	0.6	15015(6%)	89.1	10.7(6)	0.61(3)	10.7	0.611
18-10-94A	1.0	11050(8%)	86.5	7.1(6)	0.67(5)	6.46	0.611
28-03-96A	3.0	46083(9%)	71.6	43(4)	0.88(8)	29.7	0.611

Table 5.2: The geometric factor, T_c and resistivity of our detwinned $\text{YBa}_2(\text{Cu}_{1-x}\text{Zn}_x)_3\text{O}_{7-\delta}$ crystals, with $x=0.0\%$, 0.6% , 1.0% , 2.0% and 3.0% . (The geometric factor of the 1.0% crystal is not available). ρ_0 is the residual resistivity ($T=0$ K) obtained by linear extrapolate on (130-250 K) and ρ_0^* is obtained in the same way after adjusting the curves to have the same slope.

Sample (Date of growth)	$X(\%)$	Geometric Factor (m^{-1})	$T_c(\text{K})$	ρ_0 ($\mu\Omega\text{cm}$)	$\frac{d\rho}{dT}$	ρ_0^* ($\mu\Omega\text{cm}$)	$\frac{d\rho^*}{dT}$
31-08-95A	0.0	20585(6%)	96.3	-14.5(9)	0.94(6)	-15.4	1.00
04-08-94A	0.6	20415(7%)	89.2	-7.5(5)	1.01(7)	-7.45	1.00
18-10-95A	1.0	-	86.2	-	-	0.636	1.00
11-05-95A	2.0	13575(13%)	79.0	35(5)	1.0(1)	33.8	1.00
28-03-96A	3.0	23096(3%)	74.6	19.2(6)	1.09(3)	17.5	1.00

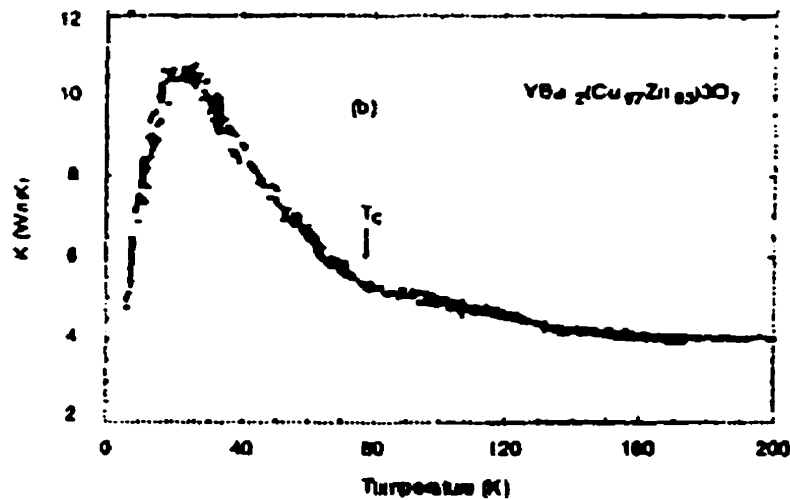


Figure 5.2: $\kappa(T)$ of $\text{YBa}_2(\text{Cu}_{1-x}\text{Zn}_x)_3\text{O}_{7-\delta}$ measured by Henning *et al.* [39] on twinned crystals.

Semba [40]. In this way, we can avoid the uncertainties that come from the geometric factor.

In this respect, note that in figure 5.3 (5.4), we did not have a geometric factor for the 0.0% twinned (1.0% detwinned) samples, so the data are normalized to have the average slope of the others.

In figure 5.5, the extrapolated residual resistivity is plotted as a function of Zn-doping. It obeys a linear relation, with $d\rho_0/dx = 1180 \mu\Omega\text{cm}/\%\text{Zn}$ for twinned crystals and $d\rho_0/dx = 1200 \mu\Omega\text{cm}/\%\text{Zn}$, for detwinned crystals. These are different from the values of $670 \mu\Omega\text{cm}/\%\text{Zn}$ in Ref [33] and $2100 \mu\Omega\text{cm}/\%\text{Zn}$ in Ref [41]. Also shown is the decrease of T_c with Zn-doping, where T_c is taken at the middle of the resistive transition. Again it is linear with x , with $dT_c/dx = 650 \text{ K}/\%\text{Zn}$ for both the twinned and the detwinned crystals. Again, this differs from the value of 1240 K derived from ref [33]. These discrepancies may well be due to the method of determining the concentration of Zn. One could therefore take care when comparing different data to use T_c as the measure of Zn content. For example, if we compare the ratio of residual resistivity to T_c , we get very close result to these two groups, $\frac{\partial\rho_0}{\partial T_c} = \frac{1200}{650} \approx 1.8$ for our detwinned crystals and around 1.7 for both [33] and [41].

Heat conduction

We show in figure 5.6 our results for the thermal conductivity of $\text{YBa}_2(\text{Cu}_{1-x}\text{Zn}_x)_3\text{O}_{7-\delta}$ of twinned crystals, with $x = 0.0\%$, 0.15% , 0.6% , 1.0% and 3.0% . Here, each curve is

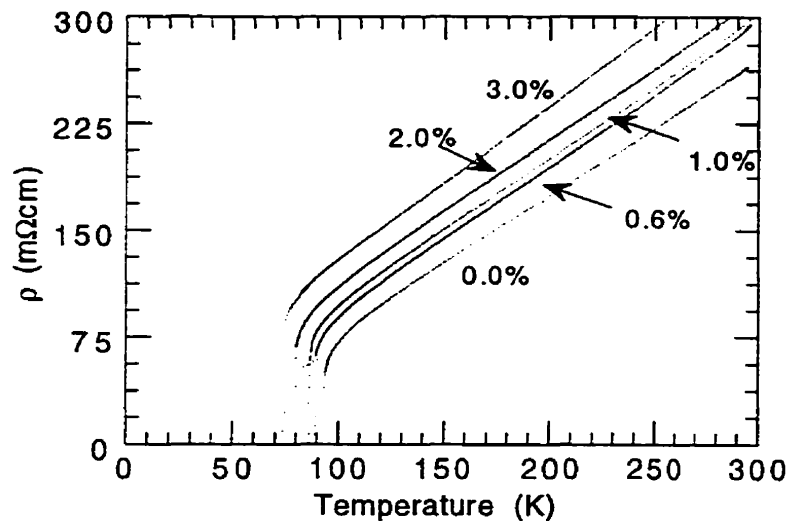


Figure 5.3: Electrical resistivity vs temperature for detwinned $\text{YBa}_2(\text{Cu}_{1-x}\text{Zn}_x)_3\text{O}_{7-\delta}$ crystals (a-axis), with $x=0.0\%$, 0.6% , 1.0% , 2.0% and 3.0% .

normalized to the same value at 100 K in the normal state, so as to show most clearly the relative drop in the peak. The results for detwinned Zn-doped crystals, with $x = 0.0\%$, 0.6% , 2.0% and 3.0% are shown in figure 5.7.

Below T_c , a peak is observed in $\kappa(T)$ for all of our Zn-doped samples. One central fact is evident, namely the peak height falls, and it does so quickly at the beginning (with small Zn-doping), followed by a slower decrease for larger doping.

At this stage, let us mention that application of the WFL in the normal state gives that the total κ includes at most a 30% electronic contribution using the resistivity data of the sample. While the electrons are strongly scattered by impurities, the phonons are not likely to be, because of their relatively long wavelengths. This is not quite supported by the detwinned crystal data, since the distinct decrease of κ in the normal state with Zn concentration (see figure 5.7) goes beyond that attributable to the resistivity. This is a somewhat puzzling result. However, it does not affect our discussion, since we are only concerned with the relative peak heights.

5.2.2 Discussion

Microwave conductivity vs Zn

Since microwave conductivity is a direct measurement on the quasiparticle behavior, some results of it are discussed in here for comparison. Zhang *et al.* [42] have

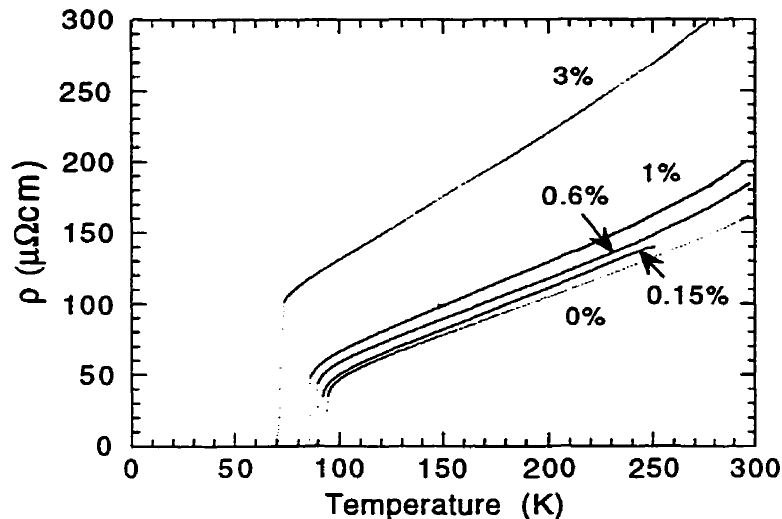


Figure 5.4: Electrical resistivity vs temperature, twinned $\text{YBa}_2(\text{Cu}_{1-x}\text{Zn}_x)_3\text{O}_{7-\delta}$ crystals with different Zn-content, where $x=0.15\%$, 0.6% , 1.0% and 3.0% .

measured the microwave conductivity σ_1 of YBCO on doped crystals for several zinc concentrations, where it is found that the peak of σ_1 below T_c is largely suppressed by as little as 0.15% Zn impurities (see figure 5.8). Their results confirmed that electron scattering rate does undergo a decrease below T_c , and addition of Zn impurities limits the drop in the scattering rate and reduces the conductivity. This is very similar to the thermal conductivity behavior observed in our data. Details about microwave conductivity measurement are given in Appendix A.

Thermal Hall effect

During the course of this work, Krishana *et al.* [26] from Princeton University measured the thermal Hall effect in YBCO, a method with the ability to observe the quasiparticle current without the phonon background. Also, κ_{xy} provides a measure of the thermal conductivity $\kappa_{e,pl}$, which only associated with the quasiparticles in CuO_2 planes, without the chain contribution. Details about the thermal Hall effect can be found in Appendix B. Their result for $\kappa_{e,pl}$ is shown in figure 5.9 along with our derived results of $\kappa_{e,pl}$. This is a direct evidence that the electronic thermal conductivity undergoes a peak below T_c .

Two scenarios

First, we tried to explain the data of figure 5.6, 5.7 in terms of the phonon scenario. As mentioned in section 3.4.1, if the total thermal conductivity in the normal state

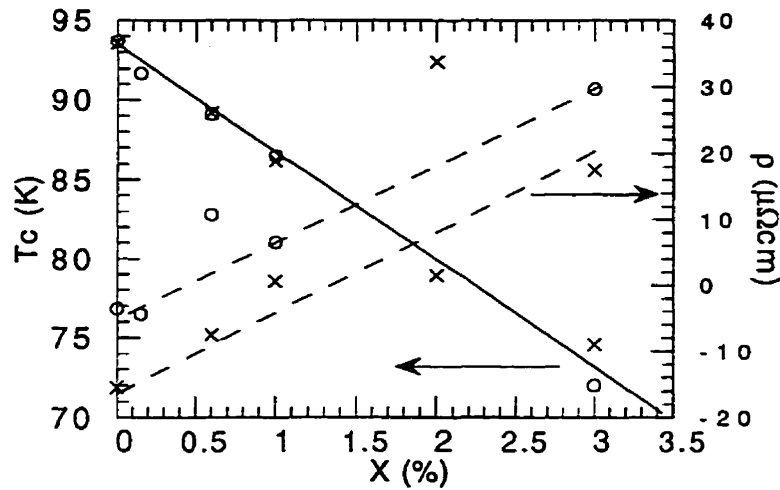


Figure 5.5: T_c and ρ_0 as a function of Zn content (see tables 5.2.1 and table 5.2.1), twinned (o) and detwinned (x), both of which show linear dependence on x .

is dominated by phonon conduction and the phonons are significantly limited by electron-phonon scattering, then, for $T < T_c$, Cooper pairs form and the number of electrons available to scatter phonons falls rapidly, resulting in an increase in the mean free path of the phonons and thus an enhancement in $\kappa(T)$ as seen in conventional superconductors. As the temperature is lowered, however, the population of phonons is further reduced, while the mean free path is limited by some other conditions (*e.g.* sample boundary). causing a decrease in $\kappa(T)$.

Assuming this is the case, we tried to fit our experimental $\kappa(T)$ data using TW theory as described in section 3.4.1. The last term in eqn. 5.1 is from Umklapp (phonon-phonon) scattering, included to give a good description of our data at high temperature (above T_c):

$$\kappa_{ph}(t) = At^3 \int_0^{\Theta_D} dx \frac{x^4 e^x}{(e^x - 1)^2} x [1 + \alpha t^4 x^4 + \beta t^2 x^2 + \delta t x + \gamma t x g(x, y) + Ut^4 x^2]^{-1} \quad (5.1)$$

Assuming that the electron conduction is a featureless, smooth function of T and only affects our analysis slightly, like Tewordt *et al.* we used the estimation from Geilikmann where a tabulated $\kappa_{e,s}/\kappa_{e,n}$ is given. We also employed a scaled energy gap: $\Delta(t) = \chi \Delta(t)_{BCS}$. For the pure case (0.0%Zn), a good fit was obtained (figure 5.10), with $A = 650, \alpha = 30, \beta = 20, \gamma = 100, \delta = 0, U = 50, \chi = 1.1$, and $\kappa_{e,n} = 1.0$. Notice that $\kappa_{e,n}$ is about 1/8 of the κ_{total} , in agreement with Krishana *et al.* estimate, 1/7. Using eqn. 3.2 and eqn. 3.6, we estimated the value of L_b (dimension

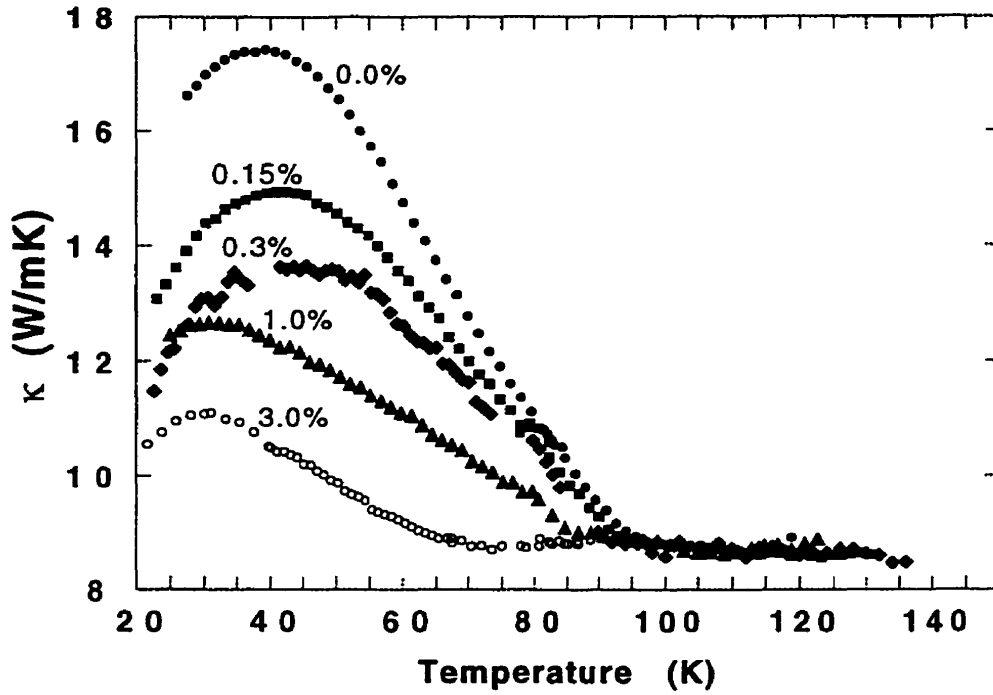


Figure 5.6: Thermal conductivity of twinned $\text{YBa}_2\text{Cu}_3\text{O}_{7-\delta}$ with the following Zn-impurity. 0% (solid circle), 0.15% (square), 0.3% (rhombus), 1.0% (triangle), 3.0% (circle). The curves are all normalized in normal state.

of our crystals) to be $20 \mu\text{m}$, and λ to be 0.25. The former represents the mean free path for boundary scattering of phonons and the latter the coupling strength between electrons and longitudinal acoustic phonons, respectively. $\Theta_D = 360\text{K}$, $a = 4\text{\AA}$, and $t = 5000 \text{ K}$ were used in this estimation [24, 38]. L_b is quite reasonable (from SEM we got $80\mu\text{m}$ for the thickness) and λ was found to fall into the weak coupling range.

The decrease in $\kappa_{ph}(T)$ with Zn doping could be associated with a change of the energy gap or the electron-phonon coupling strength instead of simply a change in the impurity scattering of phonons, because Zn has almost the same radius as Cu (0.75\AA and 0.73\AA , respectively) and the same ionic valence (+2). Following the standard work of Slack and Klemens, we may write the thermal resistivity due to point defects as

$$1/\kappa_{defect} \approx \frac{\pi T V_0 \Gamma}{2\hbar v_s^2}$$

where V_0 is the unit cell volume and Γ measures the mass defect due to the impurity, $\Gamma = x(1 - M_{doped}/M_{pure})^2$, For the $x=1.0\%$ sample, $\Gamma = 6 \times 10^{-8}$, giving $1/\kappa_{defect} = 10^{-6} \text{ m.K/W} \ll 1/\kappa = 10^{-1} \text{ m.K/W}$.

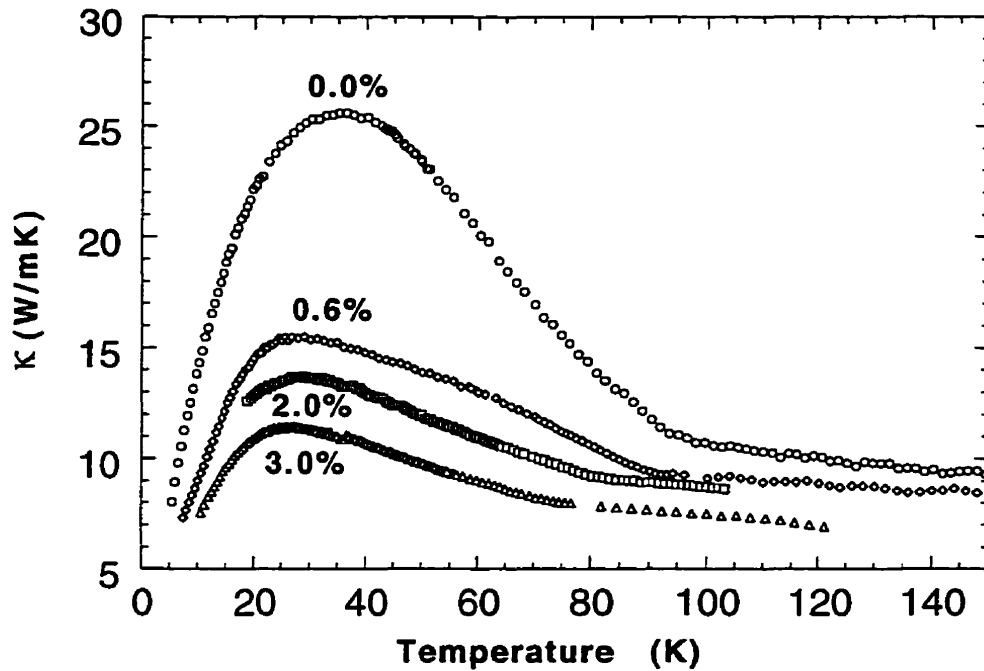


Figure 5.7: Thermal conductivity vs T for detwinned $\text{YBa}_2\text{Cu}_3\text{O}_{7-\delta}$ crystals (a-axis) with different Zn content ($x=0.0\%$, 0.6% , 2.0% and 3.0%).

Let us then consider the case if the electron-phonon interaction is significantly reduced (i.e. decreased γ) by a small addition of impurities. TW theory can still provide fits to the data, as shown in figure 5.11 (we reduce γ from 100 to 5). However, this appears to be an unsatisfactory explanation, because small levels of Zn would require substantial changes in the electron-phonon coupling, which is already small in the pure case (0.25 in our case).

An alternate explanation for the rapid suppression of the $\kappa_{ph}(T)$ peak could be a suppression of the quasiparticle gap commensurate with the reduction in T_c (Nagao [43]), i.e. a reduction in $\chi = \Delta(0)/\Delta(0)_{BCS}$, as shown in figure 5.12. The decrease of χ can indeed reduce the enhancement of $\kappa(T)$ below T_c , implying a more rapid depression of the energy gap than reflected by the reduced $T_c(x)$. Roth et al [44] found that the specific heat jump ΔC_v at T_c decreases very quickly with increasing Zn content (with 5% Zn substitution, ΔC_v was completely suppressed). This suggests that in Zn-doped samples, it is possible to exhibit a tendency to gapless superconductivity.

So from the phonon point of view, it would seem that the rapid decrease of $\kappa(T)$

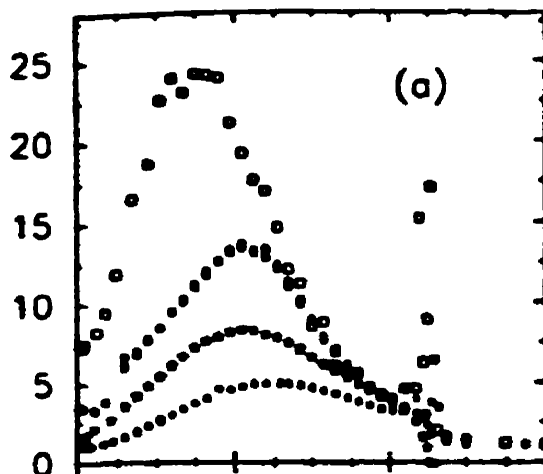


Figure 5.8: Microwave conductivity σ_1 at 3.88GHz (open squares) and 34.8 GHz (solid squares) for a pure, twinned crystal, and with 0.15% (star) and 0.31% (solid circle) Zn-impurity. The peak has almost disappeared in the 0.31% sample (after Zhang *et al.*).

below T_c for Zn-doped compounds originates from the suppression of the superconducting energy gap. However, there exist the following weak points for this as an explanation of our data:

- it cannot explain the change of the peak position in our case, specifically, at the beginning, the shift to higher temperature. For $x=0.0\%$, 0.3% , and 0.6% the ratio of peak position to T_c are 0.39, 0.46, and 0.44 respectively.
- the upturn at T_c is much sharper in the calculated curves than seen in the data. That is, it predicts a pronounced change in the slope of $\kappa(T)$ at T_c , while we observe a more gradual one, as shown in figure 5.10.

Consequently, we turn to the electronic scenario, that is, the collapse of the electronic scattering rate as a mechanism for the peak in $\kappa(T)$ of YBCO. From thermal Hall conductivity [26] and microwave measurements [25], we know that a collapse of the quasiparticle relaxation rate is observed below T_c (figure 3.8), and could be most naturally interpreted in terms of a gapping of the spectral density of electronic excitations responsible for inelastic scattering just above T_c .

Hirschfeld and Puttikka [45] adopt a theoretical model of electronic transport in a d-wave superconductor limited by impurity and spin fluctuation scattering and apply it to calculate the electronic thermal conductivity. Let us say a word about this

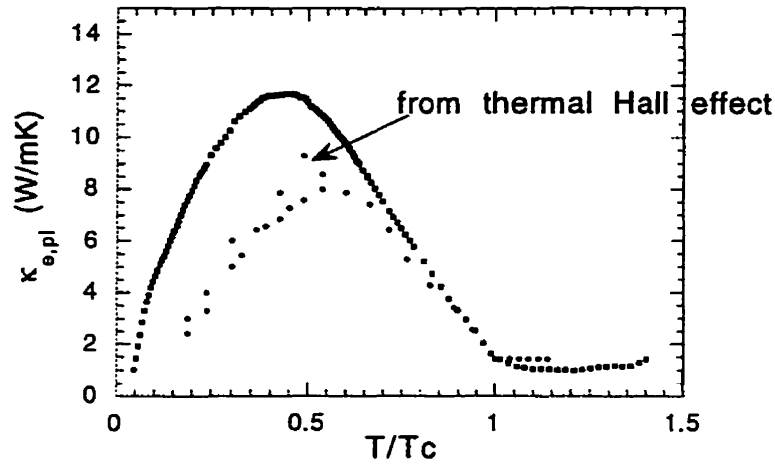


Figure 5.9: Comparison of $\kappa_{e,pl}$ measured by us with that from thermal Hall effect by Krishana [26]. $\kappa_{e,pl}$ of ours is obtained by subtracting the estimated κ_{ph} from κ_{total} .

theory before discuss our data.

The model is focused on a combination of phonon and electron conduction. They suggested that quasiparticles excited above the ground state are scattered with a total rate

$$1/\tau = 1/\tau_{imp} + 1/\tau_{\phi} \quad (5.2)$$

where $1/\tau_{imp}$ is the relaxation rate due to potential scatterers (*e.g.* impurities) and $1/\tau_{\phi}$ describes the rate of scattering by inelastic processes (*e.g.* spin fluctuations). The electronic thermal conductivity κ_e for an unconventional superconductor is then evaluated using a Kubo formula. They use a self-energy Σ_0 due to the elastic impurity scattering which is treated in a self-consistent t-matrix approximation and is given by $\Sigma_0 = \Gamma G_0 / (C^2 - G_0^2)$, where $\Gamma = n_i n / (\pi N_0)$ is the unitary limit scattering rate depending on the concentration of the defects n_i , the electron density n , and the density of state at the Fermi level N_0 . C is the scattering strength of an individual impurity and G_0 is the integrated propagator. Then they adopted a model of scattering by anti-ferromagnetic spin fluctuations based on an RPA treatment of the Hubbard model with parameters chosen to reproduce normal state NMR and resistivity data in YBCO [46], Thus make the replacement $\Sigma_0 \rightarrow \Sigma_0 - i/2\tau_{in}$.

The bare heat response is then given by a convolution of the Green's function G

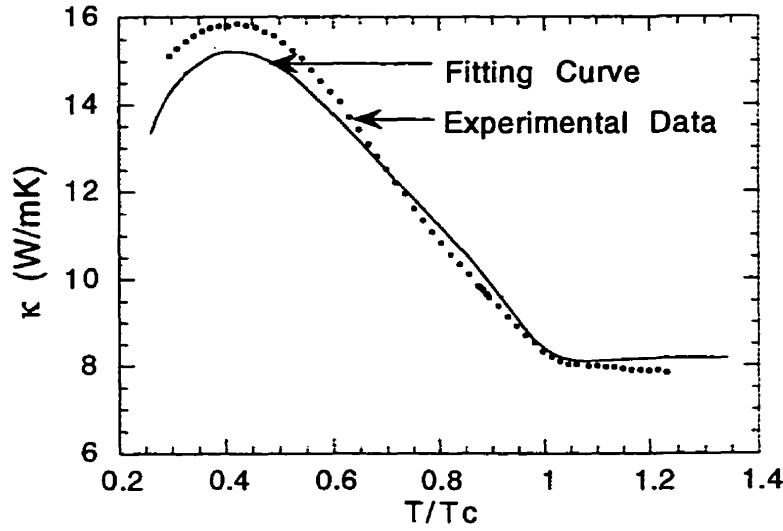


Figure 5.10: Total thermal conductivity κ vs temperature for the pure twinned crystal: experimental data (circles) and fitted curve (solid line) using TW theory for phonons and Geilikmann's estimation for electrons, with $A=650$, $\alpha = 30$, $\beta = 20$, $\delta = 0$, $\gamma = 100$, $U = 50$, $\chi = 1.1$ and $\kappa_{el} = 1$.

for the diagonal thermal conductivity tensor and one obtains

$$\frac{\kappa_{e,s}^i(T)/T}{\kappa_{e,n}^i(T_c)/T_c} = \frac{6}{\pi^2} \int_0^\infty dw \left(\frac{w}{T}\right)^2 \left(-\frac{\partial f}{\partial w}\right) K_i(w, T) \quad (5.3)$$

$$K_i(w, T) = \frac{\Gamma_{tot}(T_c)}{w'w''} \times Re \left\langle \kappa_i^2 \frac{w^2 + |w|^2 - 2|\Delta_k|^2}{\sqrt{w^2 - |\Delta_k|^2}} \right\rangle_k$$

where w' and w'' are the real and imaginary parts of frequency w , f is the Fermi function, and $\Gamma_{tot} \equiv \Gamma_0 + 1/2\tau_{in}$ is the total quasiparticle scattering rate. They have numerically evaluated eqn. 5.3, and their results are reproduced in figure 5.13, where different impurity scattering rates Γ/T_{c0} are calculated. In the clean limit, the combination of the collapsing relaxation rate with decreasing temperature due to gapping of the spin fluctuation spectral density and the rapidly decreasing number of quasiparticles at low T leads to a peak in the thermal conductivity. As impurities are added, the collapse of the inelastic scattering rate is cut off at progressively higher and higher energy scales, such that the peak moves to higher and higher temperatures and simultaneously weakens.

We can see that this model could give us a good description of our data if we consider the following:

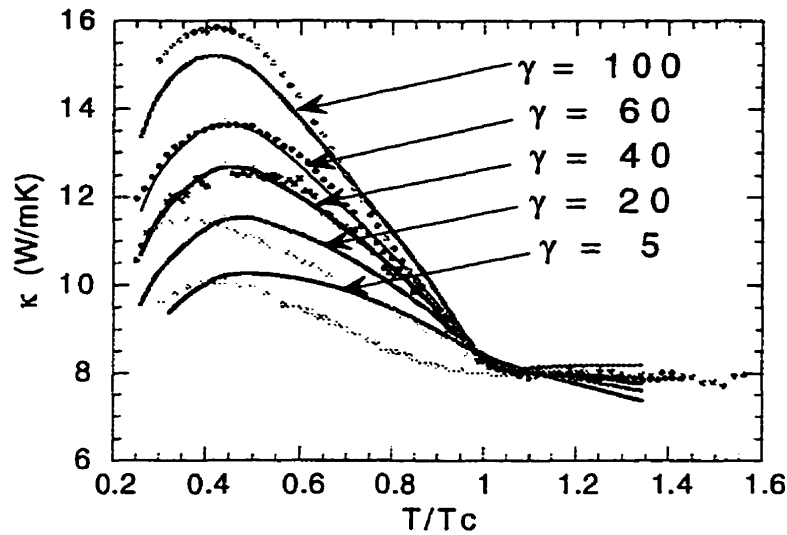


Figure 5.11: κ vs $T(K)$, with different Zn concentrations, Solid lines are fitted by TW theory with different γ which is related to the coupling constant between phonons and electrons.

1) For phonons, consider that as the temperature is decreased, two trends are expected, a) the phonons density decrease, which results an decreased phonon specific heat. b) Umklapp (phonon-phonon) scattering decrease, resulting an increasing mean free path l_{ph} . Because the former falls off faster than the latter, this would result in a rise in $\kappa(T)$. The increase in mean free path of phonon is then cut off when temperature further down, due to the decrease of phonon density along with the dominance of other scattering mechanisms, thus, result in a small peak at 25-30 K. This could be account for our 3% data. From thermal Hall conductivity [26], Krishana *et al.* estimated that about 6/7 of κ in the normal state is due to phonons. This is higher than our 3% data, which is only 70% of that of pure crystal. Considering that phonons actually would also be effected by impurities to some extent, it is possible that the data of 3% is too low to be taken as the phonon part of the pure crystal. As a result, we adjusted it to be 6/7 of κ for the pure sample at 100 K, and took this to be our κ_{ph} . This procedure is shown in figure 5.14.

2) For the electron part, we obtained it by subtracting κ_{ph} from κ_{tot} , as shown in figure 5.14, which yields a huge peak below T_c in κ . This is very similar to the results obtained by Hirschfeld and Putikka. We further adopted their calculations of the electronic thermal conductivity with the increasing impurity scattering (figure 5.13), and when combined with our own phonon estimation, which is also, very close to

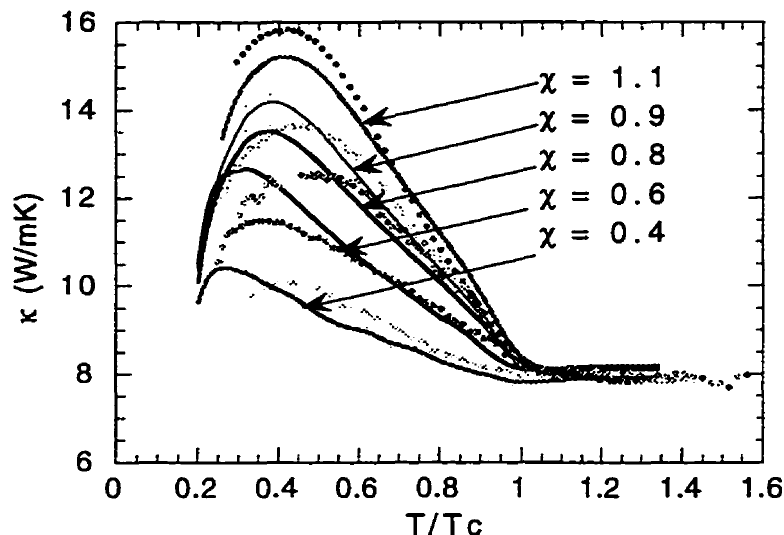


Figure 5.12: κ vs $T(K)$ with different Zn concentrations. Solid lines are fitted by TW theory with different gap scaling ratio χ .

theirs, gives a very good fit of our Zn-doping results (see figure 5.15).

It is clear that the effect of increasing the impurity concentration within this scenario is to cut off the collapse of the inelastic scattering rate, which leads to a shift in the peak to higher reduced temperatures T/T_c . However, $\kappa_{ph}(T)$, which dominates κ_e in the normal state for all the samples, will also show a peak at lower temperature. Therefore, the position of the peak in the total κ now may be explained as follows: while the electronic peak initially dominates and moves upward in T with disorder, the phonon peak at 25-30 K eventually becomes more important. This, indeed, provides a good account of our twinned data.

Our data on detwinned crystals (a-axis) also support the latter explanation (figure 5.7). To make things clear, we plot the ratio of peak height to the value at T_c of the conductivity in figure 5.16 and the ratio of peak temperature to transition temperature in figure 5.17. We can see that in both types of crystals, the relative peak height decreases very fast with small amount of Zn, because of the suppression of the electronic part due to impurities, as observed in the microwave conductivity (see figure 5.8).

As to the peak temperature, it shows that at low levels of Zn, the peak shifts higher and then shifts lower when the Zn content continues increasing. We attribute the latter trend to the appearance of the phonon peak. This conclusion is not quite

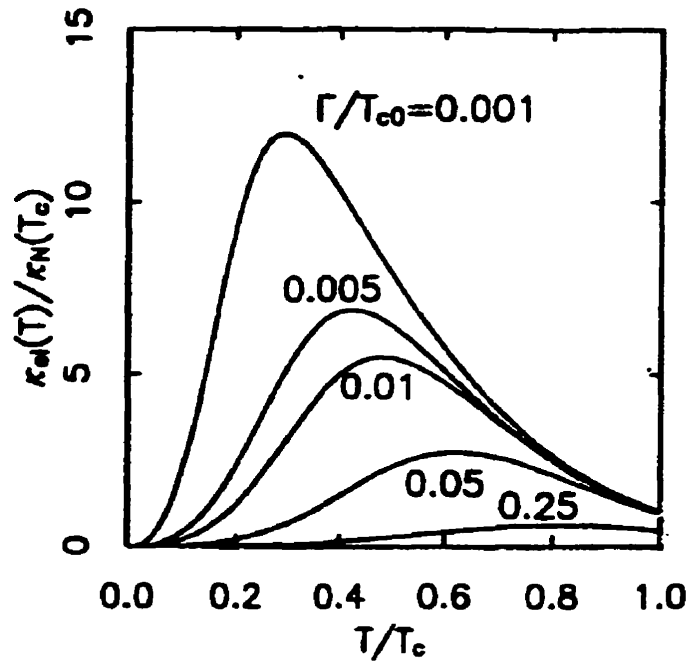


Figure 5.13: Normalized electronic thermal conductivity $\kappa_{e,s}/\kappa_{e,n}$ calculated by Hirschfeld *et al.*, using different impurity scattering rates Γ/T_{c0} .

true for the present detwinned crystal data (figure 5.17). Unfortunately, the low concentration Zn-doping of this case are not available at this time, to clarify, further measurements need to be done.

5.2.3 Summary

In light of the microwave data and thermal Hall data, We favor the electronic scenario as the most likely model to account for the peak in $\kappa(T)$, that is, electronic thermal conductivity is in large part responsible for the peak and is strongly suppressed by impurity scattering. The following conclusions about our Zn-doped YBCO data could then be drawn:

1. electronic conduction does account for most of the peak in clean crystals;
2. a small peak in κ_{ph} does occur at about 20-25 K;
3. phonons in fact dominate heat conduction in YBCO above T_c ;
4. the phonon contribution also decreases slightly with Zn doping;

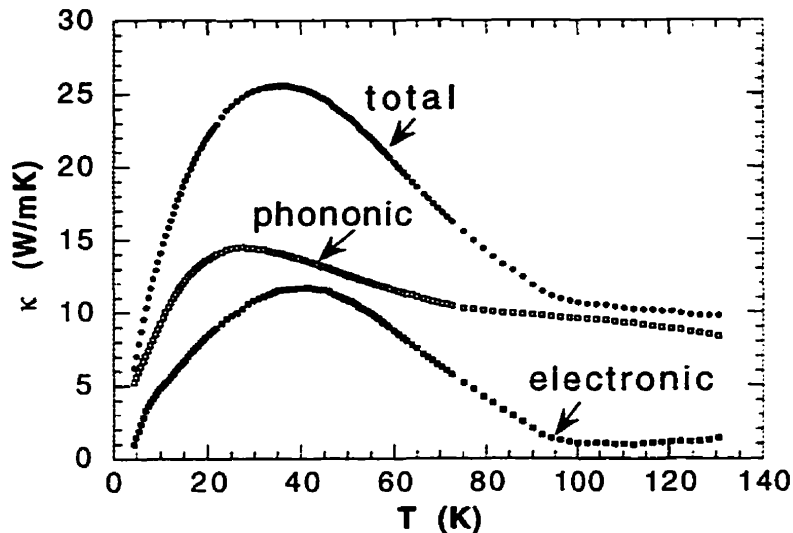


Figure 5.14: Demonstration of thermal conductivity consisting of phononic part and electronic part, where the phononic part is obtained from the high Zn-impurity concentration data ($x = 3\%$), after being adjusted to $6/7$ of the total value in the normal state. The electronic part is obtained by subtracting κ_{ph} from κ_{total} .

5. the temperature at which the peak in κ (T) occurs may vary non-monotonically with disorder.

The assumption, however, that the effect of impurities on the phonon κ_{ph} can be neglected is not really true. In our data for detwinned crystal (shown in figure 5.7), we observe an obvious decrease in κ in the normal state with Zn-doping, which is beyond the uncertainty in the geometric factor. Assuming the electronic part only contributes $1/7$ above T_c for pure crystals, we cannot associate this decrease with electrons only. This suggests that the decrease has its main origin in an increased scattering of phonons with Zn doping. To clarify this point, the following mechanisms could be studied further:

- the phonon conduction could be affected by impurities even though the impurities themselves may be ineffective scatterers. There might be an increasing number of dislocations with Zn-doping or a large strain field associated with the impurity Zn atom. This issue can be checked by measuring $\kappa(T)$ to lower temperature $T \ll T_{max}$, where $\kappa(T)$ is dominated by these scattering.
- another potential scattering mechanism can be twin boundaries (which could be viewed as sheet-like faults), the density of which is observed to increase with

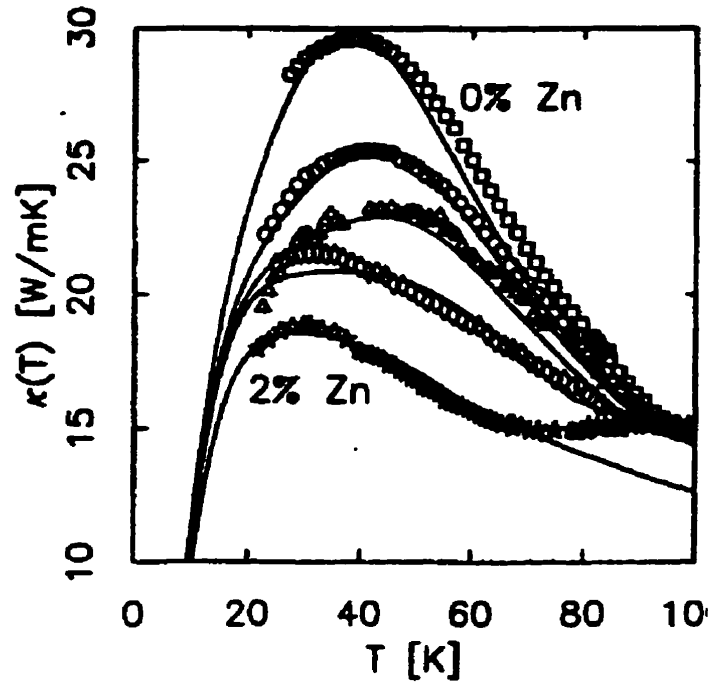


Figure 5.15: Total thermal conductivity κ vs T fitted by using $\kappa_{e,s}$ calculated by Hirschfeld, for Zn concentration 0.0%, 0.15%, 0.3%, 1.0% and 3.0%.

increasing Zn-doping. We have used the result for detwinned crystals (κ_a and κ_b) to calculate the average value for a pure sample: $\kappa_{ab} = \frac{1}{\frac{1}{2}(1/\kappa_a + 1/\kappa_b)}$, which turns out to be larger than the κ_{twinned} that we measured (see figure 5.18). This suggests that heat carriers are indeed scattered by twin boundaries, which is in contrast to electrical conductivity, we found that electrons are not scattered by twin boundaries, something which is discussed in the next section.

As a result, the mechanism behind the peak in κ changing at higher concentrations of Zn is still controversial. It could be explained by continuing electronic κ suppression as described by Hirshfeld and Putikka or by phonon κ changing with disorder (the electron part has been suppressed completely for as little as 0.6% in our case). Further study on this subject is needed.

The last point I want to mention on this issue is that we cannot, however, rule out the possibility that phononic thermal conductivity could be affected by Zn doping in a subtle way: via the modification of electronic degree of freedom, which, in turn, affects the phonon's lifetime. This is omitted in here because it is somewhat complicated and has been addressed by Ting *et al.* [38].

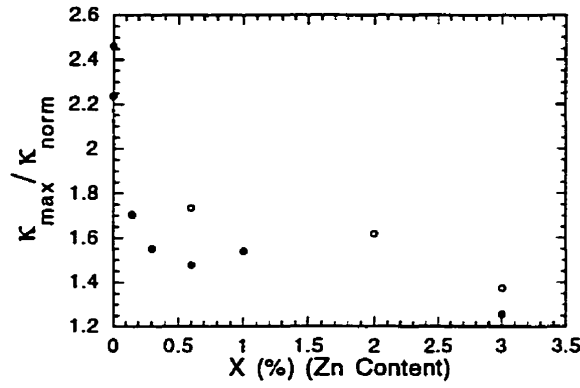


Figure 5.16: The ratio of κ_{max} (peak value) to κ_{norm} (normal state value, $T=100$ K) for twinned (solid) and detwinned (empty) $YBa_2(Cu_{1-x}Zn_x)_3O_{7-\delta}$ crystals, as a function of Zn content. The decreasing trend in both cases (twinned and detwinned) is obvious as Zn impurities increase.

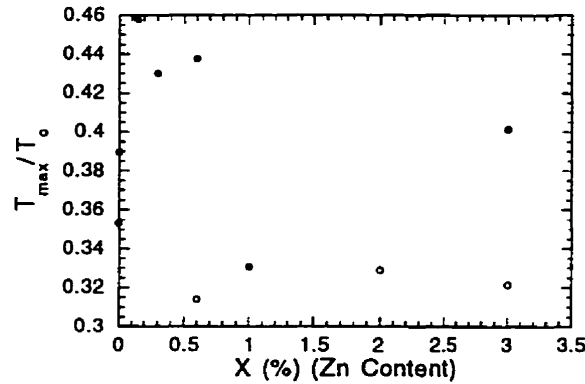


Figure 5.17: The ratio of T_{max} (the temperature at which the peak in $\kappa(T)$ occurs) to T_c as a function of Zn content, which shows non-monotonic change with increasing of Zn impurities. (solid for twinned and empty for detwinned crystal).

5.3 Anisotropy in $\kappa(T)$

5.3.1 Results

Charge conduction

The electrical resistivity of a detwinned YBCO crystal for a current along the b-axis is shown in figure 5.19. It is known that along the b-axis, the resistance consists of two parallel contributions: one from the CuO_2 planes, and one from the CuO chains, along the b-axis. From these one can obtain:

$$\rho_b = \rho_{plane} \times \rho_{chain} / (\rho_{plane} + \rho_{chain}) \quad (5.4)$$

or equivalently:

$$\rho_{chain} = \rho_b \times \rho_{plane} / (\rho_b - \rho_{plane}) \quad (5.5)$$

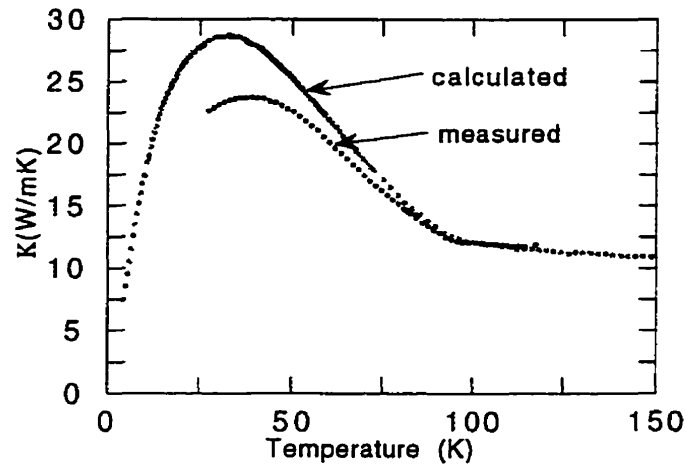


Figure 5.18: κ_{twin} (measured value) vs T, compared with κ_{ab} calculated using $\kappa_{ab} = \frac{1}{\frac{1}{2}(1/\kappa_a + 1/\kappa_b)}$. The difference between them should be due to the effect of twin boundaries.

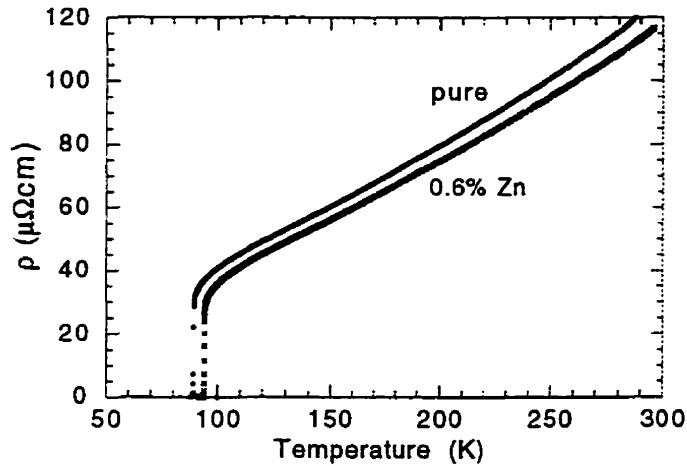


Figure 5.19: Electrical resistivity vs T of b-axis $\text{YBa}_2(\text{Cu}_{1-x}\text{Zn}_x)_3\text{O}_{7-\delta}$ crystals with $x=0.0\%$ and 0.6% . The curvatures are obvious in higher temperature for both.

where $\rho_a = \rho_{\text{plane}}$. We found ρ_{chain} can be expressed roughly as $\rho_{\text{chain}} = \rho_{\text{chain},0} + aT^2$, where $\rho_{\text{chain},0}$ is the residual resistivity in the chains. We fitted our data for the pure sample between 130 K and 270 K (to avoid the fluctuation regime), and found a and $\rho_{\text{chain},0}$ to be $0.0016 \mu\Omega\text{cmK}^{-2}$ and $66\mu\Omega$ respectively. The quadratic dependence on temperature of ρ_{chain} was explained by scattering of the 1-D electrons by phonons, as discussed in ref [13].

Next we turn to the resistivity of the twinned YBCO to study the effect of twin boundaries on charge conduction. In figure 5.20, the measured resistivity of a pure twinned sample is plotted. Assuming an equal number of a- and b- oriented domains

as we discussed in section 4.2.1, then, the expected value of a twinned crystal can be calculated from ρ_a and ρ_b by $\frac{\rho_a + \rho_b}{2}$, if the boundaries have little effect on charge transport. From figure 5.20, we see that the measured curve and calculated curve coincide very well, indicating that the effect of twin boundaries is negligible, that is, the twin boundaries are not a significant scattering mechanism for charge transport (at least above T_c).

Heat conduction

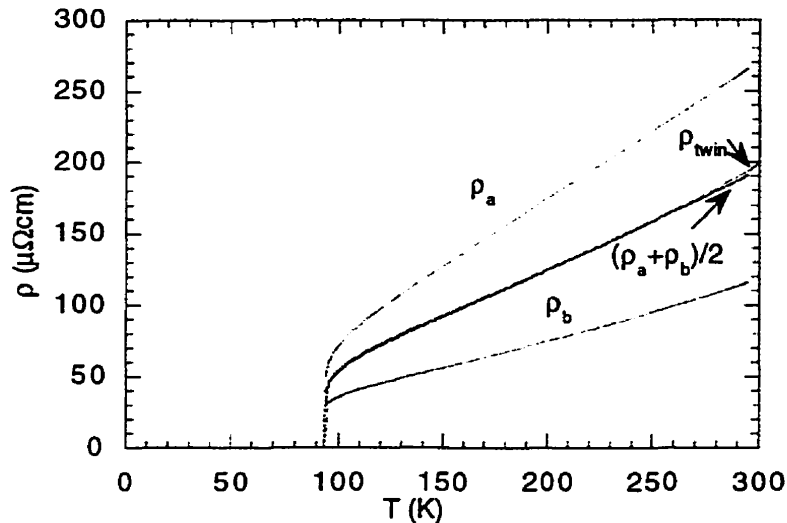


Figure 5.20: The resistivity of twinned crystals; comparison of measured and calculated using $\rho_{twin} = \frac{\rho_a + \rho_b}{2}$.

Let us now turn to the anisotropy of thermal conductivity in the ab -plane of YBCO. The temperature dependence of κ_a and κ_b from 150 K to 4.2 K is shown for the pure and 0.6% YBCO crystals in figure 5.21 and 5.22, respectively. One can see that, above T_c (≈ 93 K and 89 K respectively), the temperature dependences of κ_a and κ_b are nearly identical, except for a constant offset. Both increase monotonically with decreasing temperature. Below T_c , both of them increase rapidly, a familiar feature for κ of YBCO. However, an obvious feature is that the temperature dependence of κ_a and κ_b below T_c are not the same, with peaks at around 40 K and 25 K respectively. The difference between them (for pure crystals) is plotted in figure 5.23. Two aspects are striking: there is not a trace of an anomaly at $T_c = 93.8$ K, in contrast to the plane behavior (κ_a), and a sizeable increase sets in rather suddenly at a much lower temperature, about 55 K, giving rise to a peak centered around 15 K.

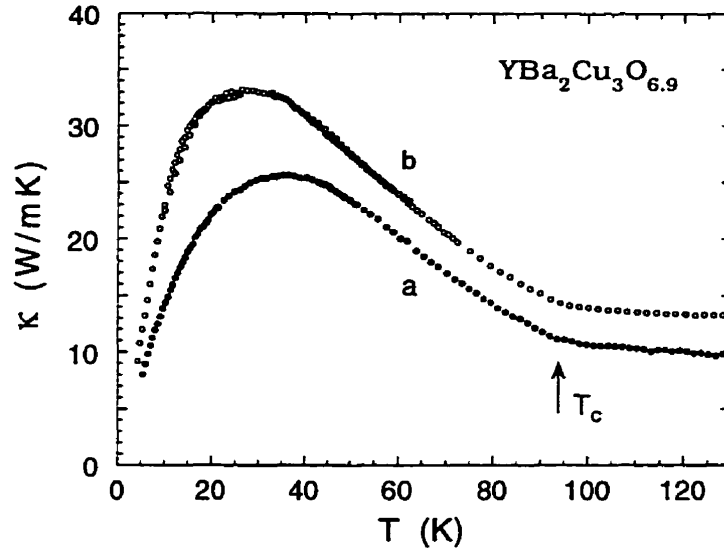


Figure 5.21: Thermal conductivity of pure $\text{YBa}_2\text{Cu}_3\text{O}_{7-\delta}$ along two directions (a-axis and b-axis). It is obvious that the maximum appear at different temperatures (40 K for a-axis and 25 K for b-axis).

5.3.2 Discussion

First, we hope to find if this anisotropy is due to phonons or not, which could arise either from an anisotropy in the electron-phonon interaction or in the phonon spectrum (*i.e.* sound velocity). From results of ultrasound measurements [47], however, we know the sound velocity along the a-axis and the b-axis are close to each other, because the $\text{YBa}_2\text{Cu}_3\text{O}_{7-\delta}$ structure is only slightly away from tetragonal symmetry, with the b-axis only 2% \sim 3% longer than the a-axis. Therefore, it is not likely to be the source of the anisotropy. As for a possible difference in the mean free path for phonons in the two directions, it is not inconceivable to assume that the scattering rate for phonons along the b-axis is less than that along the a-axis. However, it would be difficult to explain the appearance of an anomalous feature of κ_{ph} well below T_c (and not just at T_c). As a result, we anticipate that the difference in the temperature dependences of κ_a and κ_b may be associated, at least in large part, with the anisotropy of the electronic thermal conduction.

Considering the structure of YBCO, we applied a simple model of parallel conduc-

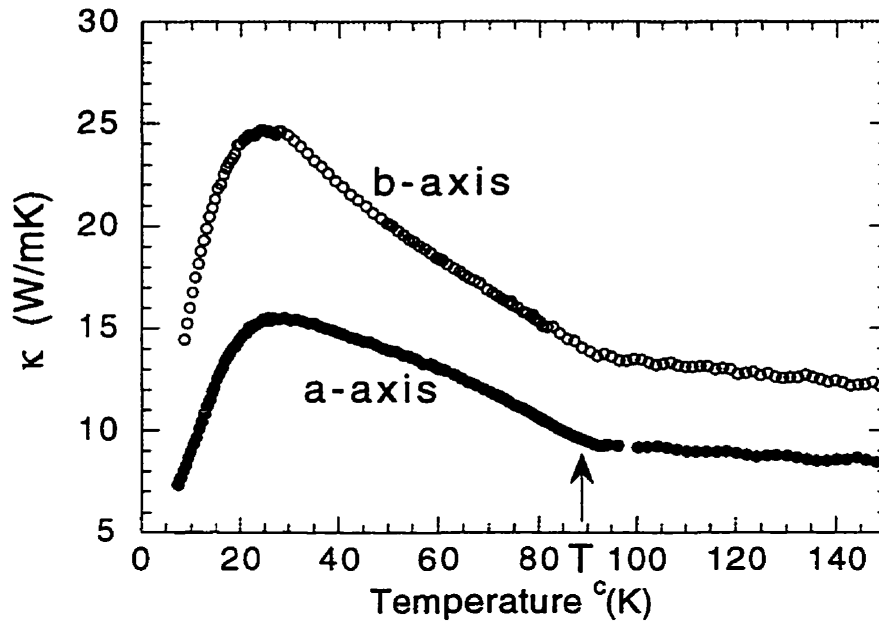


Figure 5.22: Thermal conductivity of detwinned (a-axis and b-axis) crystals for Zn-doped sample ($x=0.6\%$).

tion channels to the b-axis conductivity, viewing it as a sum of separate conductivities in the CuO_2 planes and along the CuO chain: $\kappa_b = \kappa_a + \kappa_{chain}$. Then κ_{chain} is the difference, $\kappa_b - \kappa_a$, shown in figure 5.23. The anisotropy in the normal state is roughly constant and the difference $\kappa_b - \kappa_a$ hovers between 3.0 and $3.5 \text{ Wm}^{-1}\text{K}^{-1}$, with an absolute uncertainty of $\pm 10\%$. If we apply WFL to the chain conductivity above T_c , we get $\frac{L_0 T}{\rho_{chain}} = 3.5 \text{ Wm}^{-1}\text{K}^{-1}$, where $L_0 = 2.44 \times 10^{-8} \text{ } \Omega\text{WK}^{-2}$ is the Sommerfeld value. Noting also that the anisotropy ratio κ_b/κ_a in the normal state is 1.2 to 1.4, assuming the electronic part is $1/7$ of κ , we find $\kappa_{b,e}/\kappa_{a,e} = 2.6 \sim 3.4$ in the normal state, very close to the measured electron resistivity ratio $\rho_a/\rho_b = 2.1$. All of these features indicate that electrons are responsible for κ_{chain} .

An interesting feature is that the peak in κ_{chain} is very similar to that in κ_{plane} . We can actually see the similarity more clearly if we scale the temperature by the onset point in both peaks (55 K and 93 K respectively), as in figure 5.24. (for ease of comparison, the data is normalized in such a way that the two peaks have roughly the same height once a constant background has been subtracted). This shows that heat conduction can be used as a measure of the onset of superconductivity, just as easily as the electrical resistivity or the magnetic susceptibility. For example,

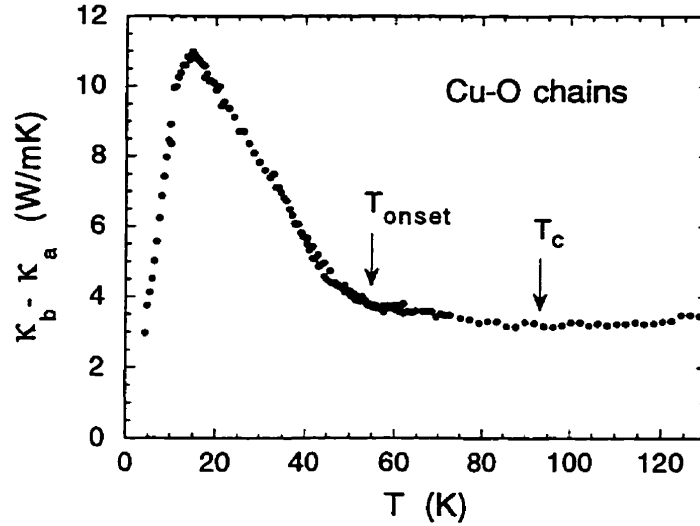


Figure 5.23: κ_{chain} for a pure $\text{YBa}_2\text{Cu}_3\text{O}_{7-d}$ crystal.

the arrow in figure 5.21 shows the resistivity determined transition temperature, in perfect coincidence with the change in κ . This will work as long as electrons are a major source of scattering for the carriers of heat. This is not only true at T_c , but also below T_c .

These features cannot be described by a single gap structure below T_c , because any model using a single gap or order parameter (s- or d-wave) will only lead to a single conductivity peak. Therefore, it is necessary to consider a 2-component system to understand the data. The essential features of the data can be well described by a model of two superconducting components, one associated to plane, with $T_c = 93$ K, the other to the chain, with $T_c = 55$ K. Here, let us introduce a theory of single-electrons tunneling, which gives a description of the 2-component model:

It is commonly believed that the pairing interactions in YBCO are localized to the CuO_2 planes. However, the CuO chains could become superconducting via a coupling with the planes, by single-electron tunneling, *i.e.* the proximity effect. And since the chains are intrinsically normal and their superconducting state is only induced, a smaller gap than that of the planes is expected [48]. In this model, the Hamiltonian is written as :

$$H = H_0 + H_1$$

$$H_0 = \sum_k \left[\sum_n \epsilon_{nk} c_{nk\sigma}^\dagger c_{nk\sigma} + \epsilon_{\perp k} (c_{1k\sigma}^\dagger c_{2k\sigma} + H.c.) \right]$$

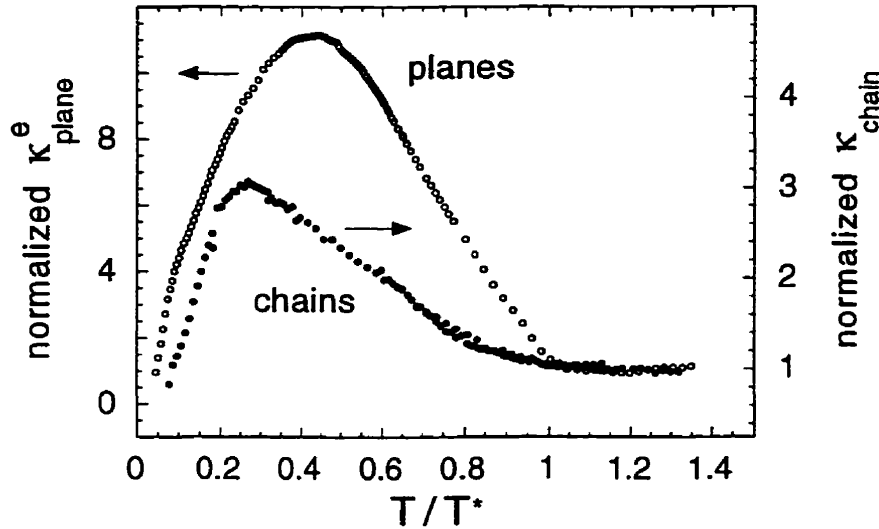


Figure 5.24: Comparison of κ_{chain} and κ_{plane} vs reduced temperature (T/T_c). The similarity between them suggests the 2-component gap structure in YBCO crystal. We normalized the two curves to the same normal state value and same peak height to emphasize the similarity between them.

$$H_1 = \sum_{nk} \Delta_n \gamma_{nk} (c_{nk\uparrow}^\dagger c_{n-k\downarrow}^\dagger + H.c.)$$

A general feature of the proximity effect models appears to be pronounced upward curvature in the superfluid density along \vec{b} at a temperature well below T_c , as an example, Xiang and Wheatley [49] has calculated the superfluid density and their result is shown in figure 5.25. As one can see, the temperature dependence of superfluid density ρ of the \vec{a} and \vec{b} directions are different. The linear dependence for the ρ_{plane} (a -axis) is expected because d -wave pairing is used, the presence of a positive curvature in $\rho_b(t)$ ($t = T/T_c$) is evident. This can be attributed to the chain electrons, which have their own T_c and energy gap at lower temperatures. To clarify, let's considered the case where the chain and plane bands are completely decoupled (with transition temperature $T_c^{(chain)} < T_c^{(plane)}$). The superfluid densities ρ_{chain} and ρ_{plane} are shown in figure 5.25. In this special case, $\rho_b = \rho_{plane} + \rho_{chain}$ would have a sudden change at $T_c^{(chain)}$. Switching on a weak coupling leads to a single transition temperature $\approx T_c^{(plane)}$ but leaves a smooth upturn in $\rho_b(t)$.

This can be used to give an explanation of our data qualitatively, that is, there exists a second superconducting gap for the electrons in the CuO chains, because of the coupling with the planes, therefore they have a smaller energy gap and lower T_c . When the temperature goes through $T_c^{(chain)}$, the electrons in the chains begin

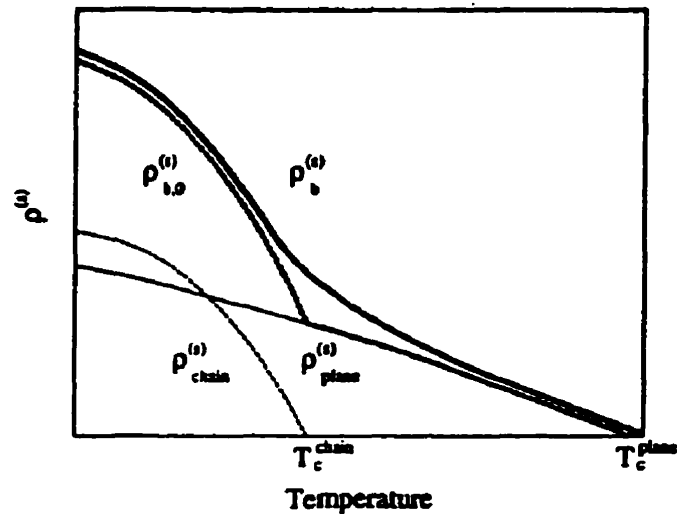


Figure 5.25: The superfluid density in the 2-gap model, $\rho_{chain}^{(s)}$ and $\rho_{plane}^{(s)}$ are the superfluid densities of the chain and planes when the interlayer coupling is zero. Then $\rho_{b,0}^{(s)} = \rho_{plane}^{(s)} + \rho_{chain}^{(s)}$. When chains and planes are weakly coupled by single electron tunneling, the chain-direction superfluid response develops a positive curvature near $T_c^{(chain)}$

to condense, resulting in an enhancement of κ_{chain} via the same mechanism as that in κ_{plane} . In κ_b , there are two peaks which overlap with each other in a certain temperature range. We point out that the existence of two gaps has been suggested by other experiments: the temperature dependence of the Knight shift [50] and the NMR relaxation time [51].

Our results on κ_{chain} may well explain the recently reported data by H. Srikanth *et al.* [29], who observed two peaks in $\sigma_1(T)$ below T_c , and a two-stage growth in the superfluid density (or λ), as shown in figure 5.26. They also described this in terms of two superconducting components, with $T_{cA} = 60 K$ and $T_{cB} = 93 K$. However, these authors used twinned crystals, so they were unable to say what role the chains play in this two-component superconductivity.

Interestingly, this two-stage behavior is not seen in the microwave results of Zhang *et al.* [42], (shown in figure 5.28). There, σ_b and σ_a shows similar temperature dependences, with only a factor of 2 difference between them in the whole temperature range. The penetration depth measured by the same group shows a similar featureless anisotropy (see figure 5.27), where λ_a and λ_b have a nearly identical temperature dependence, as does the superfluid fraction $n_s(T)/n_s(0) = \lambda^2(0)/\lambda^2(T)$, in contrast to the calculations by the 2-gap model.

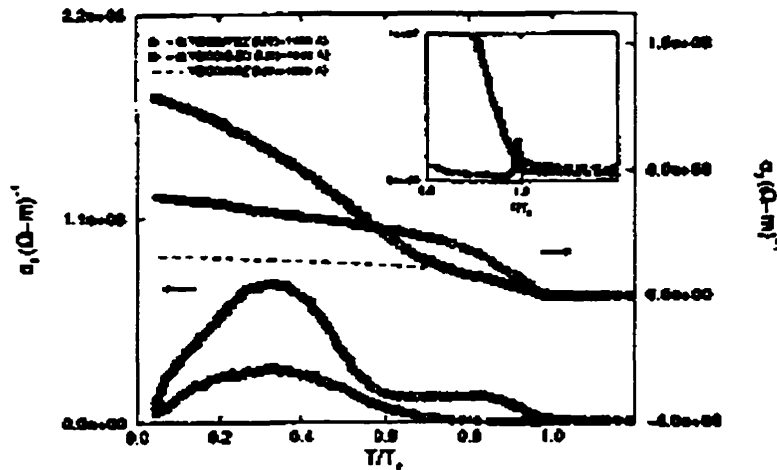


Figure 5.26: New microwave data measured by Srikanth *et al.*, which shows two peaks in σ_1 .

One should note that because electro-magnetic fields penetrate only a distance of the order of the London length into the superconductor, surface effects can complicate the determination of the bulk conductivity in the microwave technique. On the other hand, thermal conductivity is definitely a bulk probe not subject to extrinsic surface effects. As a result, the former is very sensitive to sample quality. In this respect, Srikanth *et al.* [29] showed that the microwave feature in the vicinity of 60 K is only present in samples grown in BaZrO_3 crucible and entirely absent in those prepared in ZrO_2 crucible. Therefore, it appears that our measurements are able to detect the chain anomaly in crystals where previous microwave data show no unusual behavior.

Before closing, we would like to come back to the issue we discussed at the beginning of this section, where we thought that phonons are not responsible for the anisotropy in the ab plane. What was really meant was that the anomalous feature (*i.e.* the peak of κ_{chain}) is not due to phonons, we could not rule out the possibility of an anisotropy due to phonons completely, as a matter of fact, phonon thermal conductivity may provide the constant background for the curve of κ_{chain} . Notice that for the data of our crystals, the anisotropy in the normal state is larger than expected if only electrons are taken into account. There exists a difference of 3.5 W/Km between the a -axis and the b -axis, while the electronic contribution to κ at T_c is estimated to be about only $1/7$ for a pure sample (1.2 W/mK), therefore, electrons cannot be responsible for the whole difference between κ_a and κ_b . The rest could be due to

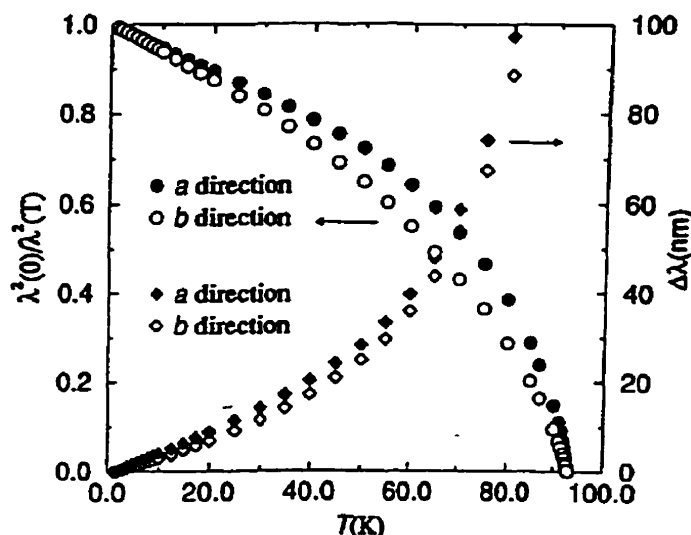


Figure 5.27: The change of penetration depth of YBCO, $\Delta\lambda(T)$ and $\lambda^2(T)$ measured by the microwave technique by Zhang *et al.* for a-axis (solid) and b-axis (empty). A similar temperature dependence is observed in these two directions.

phonons, and is featureless.

5.3.3 Summary

To conclude, we have observed a pronounced peak in the difference between the thermal conductivities of $\text{YBa}_2\text{Cu}_3\text{O}_{7-\delta}$ along \vec{b} (planes + chains) and \vec{a} (planes), which is qualitatively similar to the peak in κ_a . We interpret this feature as a sudden increase in superfluid density at about 55 K. Our result suggest that the additional superfluid growth observed below 55 K is associated with the CuO chains, which can be qualitatively explained by single-particle tunneling models. To clarify, further experiments on this issue need to be done. For example, 1) Using different oxygen content samples to observe the change of the peak due to the chain would be a very useful test of the 2-gap model. If this model were true, a decrease in the oxygen content would greatly affect the value of the smaller energy gap [52]. The reason is that the oxygen is removed preferentially from the chains, as a result, some of the chain Cu atoms develop magnetic moments which act as strong pair-breakers in the chain band, causing the gap Δ_{chain} to be suppressed very rapidly, thus, the chain develops a gapless state. 2) Tune the ratio of inelastic to elastic scattering in the chain just as was done for κ_{plane} by introducing controlled amounts of impurities that

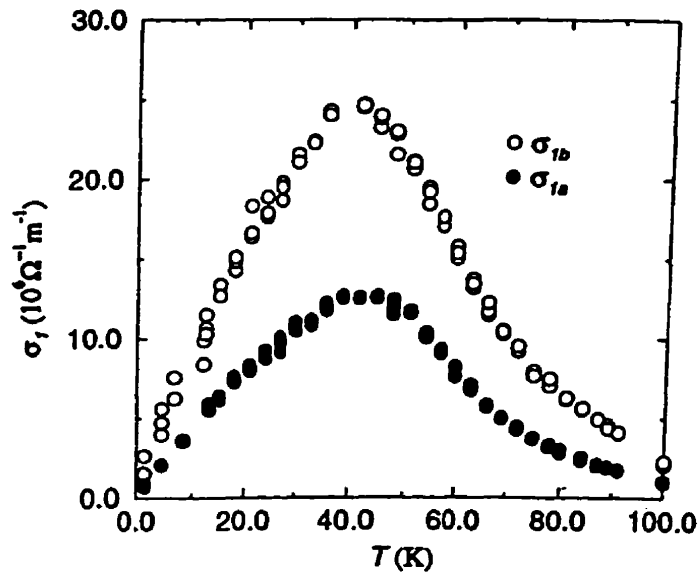


Figure 5.28: σ_1 vs temperature, along \vec{b} and \vec{a} axis, measured from the microwave resistant real part (after K. Zhang et al) A factor of 2 is observed between σ_{1b} and σ_{1a} for the whole temperature range.

go specifically in the chain, such as Au. This kind of investigation is currently under way. Just as it was for the planes, a high sensitivity to impurities would be evidence for an electronic origin to the peak in κ_{chain} . This would then directly imply that the peak in κ_{chain} is due to pair condensation of chain electrons, given that electrons in the chains are more likely to be scattered by other electrons in the chains than by electrons in the plane.

APPENDIX

A.1 Microwave conductivity

Microwave measurements can yield important information on high T_c superconductors. such as, the nature of the pairing, the quasiparticle density of states and the scattering mechanism. The principle for microwave conductivity measurements is as follows:

The surface impedance $Z_s = R_s + iX_s$, where R_s is the surface resistance and X_s is the surface reactance, is a measurable complex quantity that characterizes the electromagnetic properties of a superconductor. The surface reactance is a measure of the screening of the fields by the superconducting condensate and provides a direct probe of the London penetration depth $\lambda(T)$ via $X_s(T) = \mu_0\omega\lambda(T)$, which provides a measure of the superfluid density n_s , since $\lambda(T) = (\frac{\mu_0 n_s e^2}{m^*})^{-\frac{1}{2}}$. The real part of surface impedance, R_s , provides information about the real part of the conductivity σ_1 . In the clean, local limit ($\omega\tau \ll 2\Delta$), a 2-fluid model of the microwave surface resistance gives:

$$R_s(\omega, T) = \frac{8\pi^2}{C^4} \omega^2 \lambda^3(T) \sigma_1(\omega, T) \quad (\text{A.1})$$

where $\sigma_1(\omega, T)$ is the real part of the conductivity associated with the response of the normal fluid. At low frequencies ($\omega\tau \ll 1$) the temperature dependence of σ_1 is determined by the product of the normal fluid density, $n(T)$, and the electronic scattering time of the normal fluid, $\tau(T)$. Thus, it involves the density of states and the scattering rate of the quasiparticle.

A.2 Thermal Hall effect

Thermal Hall conductivity may provide information to help distinguish between various models of electron scattering. When a quasiparticle in a type-2 superconductor

is in a magnetic field incident on a pinned vortex line, the "handedness" of the superfluid velocity around the vortex core leads to asymmetric scattering, that is, the amplitude for scattering to the right is different from that to the left. This asymmetry produces a transverse quasiparticle current that changes sign with the field \vec{B} . The transverse current is equivalent to a thermal Hall conductivity κ_{xy} . Since phonons are scattered symmetrically by the vortices, this means the asymmetric scattering provides a selective "filter" that allows us to observe the quasiparticle current without the phonon background. Furthermore, κ_{xy} provides a measure of the mean free path of in-plane quasiparticles, and of the thermal conductivity $\kappa_{e,pl}$ associated with these excitations.

By noting that the fraction of the incident beam scattered into the transverse direction equals $\langle \Gamma_{v,a} \rangle / [\langle \Gamma_{in} + \Gamma_{v,tr} \rangle]$, where $\Gamma_{v,a}$, Γ_{in} and $\Gamma_{v,tr}$ are the asymmetric scattering rate, the inelastic scattering rate and the vortices scattering rate respectively. The Hall conductivity can then be expressed by

$$\kappa_{xy}(B) = N(T)l_0^2(\sigma'_\perp/v_F\phi_0)B/[1 + l_0\sigma'_{tr}|B|/\phi_0]^2 = pB/[1 + \alpha|B|/\phi_0]^2 \quad (\text{A.2})$$

with l_0 the mean free path, σ_{tr} the transport cross section, ϕ_0 the flux quantum, σ_\perp the transverse cross section and v_F the average Fermi velocity. p and α are two fitting parameters (p is related to the mean free path, and α measures the average quasiparticle lifetime ($\alpha = l_0\sigma'_{tr}$)), taking σ_{tr} to be T-independent, one could determine l_0 . using p and l_0 , one then could obtain $N(T)$ by $N(T)/v_F = \kappa_e(0)/l_0 = (\phi_0/\sigma'_\perp)p(T)l_0^{-2}$. Here $N(T)$ measures the entropy current, equivalent to ratio κ_s/κ_n discussed by Kadanoff [11]. Finally, this would give the profile of the κ associated with the in-plane quasiparticles, because chain electron will not contribute to $N(T)$ in here:

$$\kappa^{e,pl} = N(T)l_0/v_F \quad (\text{A.3})$$

BIBLIOGRAPHY

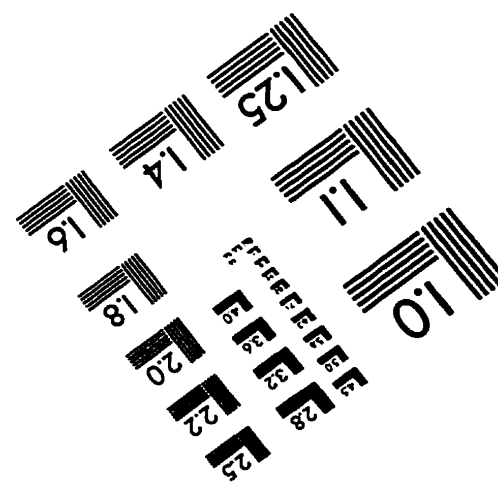
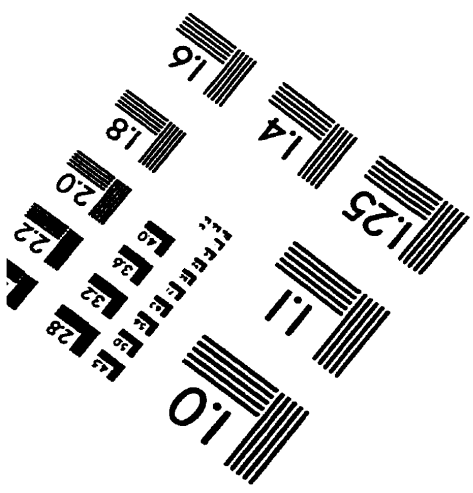
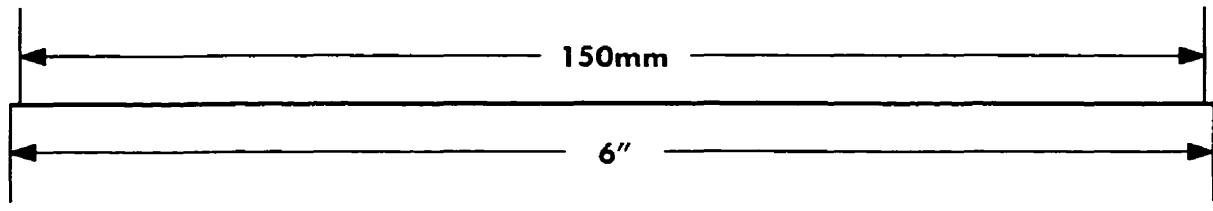
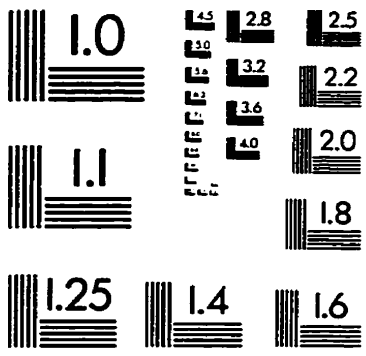
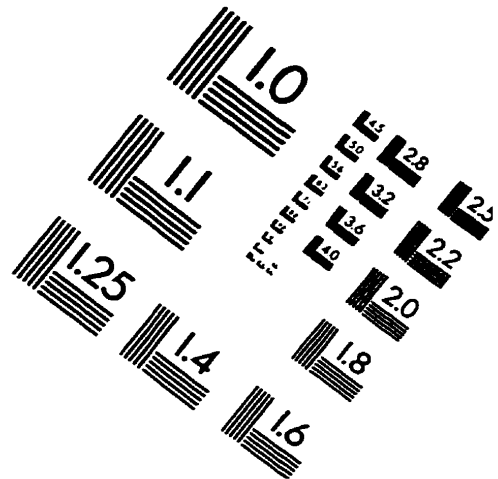
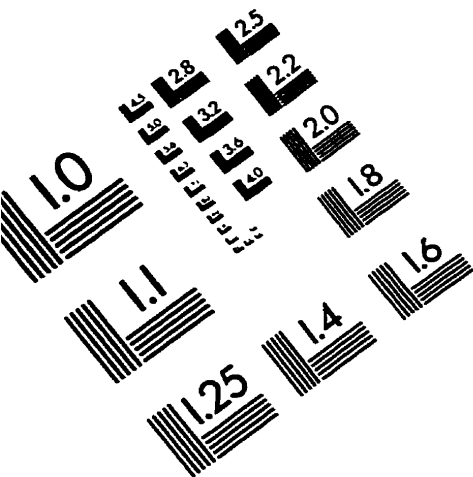
- [1] R. Berman. *Thermal conduction in solids*. Clarendon Press, Oxford, 1976.
- [2] Ashcroft and Mermin. *Solid State Physics*. Academic press, London, 1974.
- [3] J. G. Daunt and K. Mendelson. *Nature*, 141:116:118, 277, 1938.
- [4] K. Mendelssohn and J. Olsen. *Proc. Phys. Soc.*, A63:2, 1950.
- [5] J. Bardeen, G. Rickayzen, and L. Tewordt. *Phys. Rev.*, 142:146, 1966.
- [6] J. Bardeen, N. Cooper, and R. Schrieffer. *Phys. Rev.*, 108:1175, 1957.
- [7] C.B. Satterthwaite. *Phys. Rev.*, 125:873-876, 1962.
- [8] H. Frohlich. *Proc. Roy. Soc.*, A215:191, 1952.
- [9] J. Bardeen and D. Pines. *Phys. Rev.*, 99:1140, 1955.
- [10] J.M. Ziman. *Can. J. Phys.*, 34:1256, 1956.
- [11] L.P. Kadanoff and P.C. Martin. *Phys. Rev.*, 124:670, 1961.
- [12] P. Schleger, W.N. Hardy, and B.C. Yang. *Physica C*, 176:261, 1991.
- [13] R. Gagnon, C. Lupien, and L. Taillefer. *Phys. Rev. B*, 50(5):3458, 1994.
- [14] R.C. Yu, M.B. Salamon, Jian Pin Lu, and W. C Lee. *Phys. Rev. Lett.*, 69:1431, 1992.
- [15] S.J. Hagen, Z.Z. Wang, and N.P. Ong. *Phys. Rev. B*, 40:9389, 1989.
- [16] J.L. Cohn, E.F. Skelton, and S.A. Wolf. *Phys. Rev. B*, 45:1314, 1992.
- [17] L. Tewordt and Th. Wölkhausen. *Solid State Commun.*, 70:839, 1989.

- [18] N.V. Zavaritskii, A.V. Samoilov, and A. A. Yurgens. *Sov. Phys. JETP Lett*, 48:242, 1988.
- [19] Z. Gold. Thermal conductivity of the high temperature superconductor ybco. Master's thesis, McGill University, 1994.
- [20] P.G. Klemens. *Solid State Physics*. Academic Press, New York, 1958.
- [21] P.G. Klemens and L. Tewordt. *Rev. Mod. Phys.*, 36:118, 1964.
- [22] P. Carruthers. *Rev. Mod. Phys.*, 33:92, 1961.
- [23] B.T. Geilikman, M.I. Dushenat, and V.R. Chechetkin. *Sov. Phys. JETP*, 46(6):1213, 1977.
- [24] S.D. Peacor, R.A. Richardson, F. Nori, and C. Uher. *Phys. Rev. B*, 44:9508, 1991.
- [25] D.A. Bonn, P. Dosanjh, R. Liang, and W.N. Hardy. *Phys. Rev. Lett.*, 68:2390, 1992.
- [26] K. Krishana, J.M. Harris, and N.P Ong. *Phys. Rev. Lett.*, page 3529, 1995.
- [27] R. Gagnon, M.Oussena, and M. Aubin. *J. of Crystal Growth*, 121:559–565, 1992.
- [28] Th. Wolf, W. Goldacker, B. Obst, G. Roth, and R. Flukinger. *J. of Crystal Growth*, 96:1010, 1989.
- [29] H. Srikanth, B.A. Willemsen, T. Jacobs, S. Sridhar, A. Erb, E. Walker, and B. Flukiger. *cond-mat/9610032*, preprint, 1996.
- [30] R. Liang, P. Dosanjh, D.A. Bonn, D.J. Barr, J.F. Carolan, and W.N. Hardy. *Physica C*, 195:51, 1992.
- [31] T.A. Vanderah, C.K. Lowe-Ma, D.E. Bliss, M.W. Decker, M. S. Osofsky, E.F. Skelton, and M.M. Miller. *J. of Crystal Growth*, 118:385, 1992.
- [32] J.R. Lagraff and D.A. Payne. *Physica C*, 212:478, 1993.
- [33] T.R. Chien, Z.Z. Wang, and N.P. Ong. *Phys. Rev. Lett.*, 67:2088, 1991.

- [34] E.T. Swartz. *Rev. Sci. Instrum*, 57:2848, 1986.
- [35] C. Uher. *J. Superconduct.*, 3:337, 1990.
- [36] G.K.White. *Experimental Techniques in Low Temperature Physics*. Clarendon Press, Oxford, 1968.
- [37] J.M. Ziman. *Electrons and Phonons*. Clarendon, Oxford, 1963.
- [38] S.T. Ting, P. Pernambuco-Wise, and J.E. Crow. *Phys. Rev. B*, 50:6375, 1994.
- [39] P.F. Henning, G. Cao, J.E. Crow, W.O. Putikka, and P.J. Hirschfeld. *J. superconduct*, 8(1), 1995.
- [40] K. Semba, A. Matsuda, and T. Ishii. *Phys. Rev. B*, 49:10043, 1994.
- [41] Y. Fukuzumi, K. Mizuhashi, K. Takenaka, and S. Uchida. *Phys.Rev.lett.*, 76:684, 1996.
- [42] K.Zhang, A.D. Bonn, S.Kamal, R.Liang, D.J. Baar, W.N. Hardy, D. Basov, and T. Timusk. *Phys. Rev. Lett.*, 73:2484, 1994.
- [43] T. Nagao, H. Mori, F. Yonezawa, and K. Nishikawa. *Solid State Commun.*, 74:1309, 1990.
- [44] G. Roth, P. Adelman, R. Ahrens, B. Blank, H. Burkle, F. Gompf, G. Heger, M. Herrien, M. Nindel, J. Pannetier, B. Reaker, H. Rietschel, B. Rudolf, and H. Wuhl. *Physica C*, 162-164:518, 1989.
- [45] P.J. Hirschfeld and W.O. Putikka. *Phys. Rev. Lett.*, 77:3909, 1996.
- [46] S.M. Quinlan and D.J. Scalapino. *Phys. Rev. B*, 49:1470, 1994.
- [47] D.P. Almond, Q.X. Wang, J. Freestone, E.F. Lambson, B. Chapman, and G.A. Saunders. *J. Phys.: Condens. Matter*, 1:6853, 1989.
- [48] N. Klein, N. Tellmann, H. Schulz, K. Urban, S. A. Wolf, and V.Z. Kresin. *Phys. Rev. Lett.*, 71:3355, 1993.
- [49] T. Xiang and J.M. Wheatley. *Phys. Rev. Lett.*, 76:134, 1996.

- [50] S.Barrett, D.J. Durand, C.H. Pennington, C.P. Slichter, T.A. Friedmann, J.P. Rice, and D.M. Ginsberg. *Phys. Rev. B*, 41:6283, 1990.
- [51] M. Takigawa, P.C. Hammel, R.H. Heffer, and Z. Fisk. *Phys. Rev. B*, 39:7371, 1989.
- [52] V.Z. Kresin and S.A. Wolf. *Phys. Rev. B*, 46:6458, 1992.

IMAGE EVALUATION TEST TARGET (QA-3)



APPLIED IMAGE, Inc
 1653 East Main Street
 Rochester, NY 14609 USA
 Phone: 716/482-0300
 Fax: 716/288-5989

© 1993, Applied Image, Inc., All Rights Reserved